Simulation of Spark Assisted Compression Ignition Combustion Under EGR Dilute Engine Operating Conditions

by

Robert John Middleton

A dissertation submitted in partial fulfillment
of the requirements for the degree of
Doctor of Philosophy
(Mechanical Engineering)
in The University of Michigan
2014

Doctoral Committee:

Professor Dionissios N. Assanis, Co-Chair
Professor Margaret S. Wooldridge, Co-Chair
Professor Krzysztof J. Fidkowski
Professor Hong G. Im
Research Scientist George A. Lavoie
Research Scientist Jason B. Martz

When a distinguished but elderly scientist states that something is possible, he is almost certainly right. When he states that something is impossible, he is very probably wrong.

The only way of discovering the limits of the possible is to venture a little way past them into the impossible.

Any sufficiently advanced technology is indistinguishable from magic.

— Arthur C. Clarke

Learn all you can from the mistakes of others. You won't have time to make them all yourself.

— Alfred Sheinwold

To my family.

Acknowledgments

First and foremost, I would like to thank Provost Dennis Assanis for offering me the opportunity to conduct groundbreaking research in a challenging and supportive environment. His leadership has been invaluable during the course of my graduate career. I would also like to thank Professor Margaret Wooldridge for stepping in as my co-chair when Dennis moved on to Stonybrook University. I am also grateful for Professor Hong Im and Professor Kris Fidkowski for providing challenging outside perspectives.

I am extremely fortunate to have had the opportunity to collaborate very closely with Research Scientist Jason Martz on many projects. You have provided a tremendous source of scientific insight, guidance, support and friendship throughout my time here, and I could not have completed this degree without your assistance. I'd also like to thank Research Scientist George Lavoie for providing insightful scientific discussion and perspective on where my research fits into the larger engine community.

Many others have provided valuable assistance that has made this work possible. I'd like to thank Dr. Laura Olesky for providing the experimental data used throughout the validation work in this thesis, as well as providing the basis for many of the modeling studies conducted here. On the computational side, I'd like to thank Aris Babajimopoulos, SeungHwan Keum, and Janardhan Kodavasal for their technical help with KIVA. I'd also like to thank Dr. Randy Hessel for his assistance developing the computational mesh used in this work. I'd like to thank all of my friends from the Autolab, Josh Lacey, Mark Hoffman, Dan Murray, Ashwin Salvi, Luke Hagen, Elliot Ortiz-Soto, Ben Lawler, Ann Marie Lewis, Adam Vaughn, and Prasad Shingne, you've made my time here enjoyable and memorable. The autolab staff, Melissa McGeorge and Kathie Wolney have also provided significant

behind the scenes support, keep the lab running smoothly, and provide a great outlet to talk hockey and lighten the day.

I'd also like to thank all of the other people in and around Ann Arbor that have become my friends or have otherwise supported my time here. Particularly all of the players, staff, and hockey junkies at the Arctic Coliseum Adult Hockey Leagues in Chelsea, some of you have been teammates, others competitive rivals, all friends that have helped me maintain balance with the long hours of work and research that went into this thesis.

Finally, I would like to thank my parents, Robert C. and Mary P. Middleton, and my brothers Tim and Andrew, for their love and support during the course of my education. I am also thankful for my extended family here in Ann Arbor, especially Aunt Nola, Uncle Gary, and Aunt Gilda, you've made my time here feel more like home.

Preface

This work was supported by: A University Consortium on Efficient and Clean High Pressure Lean Burn (HPLB) Engines, Department of Energy Contract DE-EE0000203.

Table of Contents

List of Tables

Table

List of Figures

Figure

Abstract

Spark Assisted Compression Ignition (SACI) combustion has been shown to provide highly efficient, potentially low NO_X operation similar to that of Homogeneous Charge Compression Ignition (HCCI) combustion. Direct control over ignition timing and burn rate demonstrated through SACI operation has shown the ability to overcome several of the key shortcomings of HCCI operation while simultaneously allowing an increase in power density. However, detailed SACI models capable of capturing the charge preparation process and impact of dilution with exhaust gas recirculation (EGR) are currently limited. The current work addresses this need by developing and applying such a model to investigate SACI combustion behavior in an engine.

As part of the model development it is essential to have valid predictions of laminar flame speeds under SACI conditions. Until now this has not been readily available in the literature. To address the need for reaction front data under highly EGR dilute, high preheat temperature conditions in the SACI regime, laminar premixed reaction front simulations were conducted. Moderate burning velocities were observed for high EGR dilutions typical of mid and high load HCCI operation, provided that preheat temperatures were elevated and burned gas temperatures exceeded 1450 K. For a given preheat and burned gas temperature, moving from air dilution to EGR dilution suppressed burning velocities, a behavior attributed to a decrease in the mixture oxygen content with increasing EGR. Correlations of laminar burning velocity and front thickness were developed from these data.

As a main model platform an existing model capable of capturing premixed HCCI, SI, and SACI combustion in KIVA-3V was extended to account for engine breathing and charge preparation by direct injection under conditions utilizing high levels of internal and

external EGR dilution. Using the correlated laminar flame speed and thickness data, the model was capable of predicting trend-wise agreement with metal engine cylinder pressure measurements for HCCI, SI, and SACI combustion.

Based on a detailed analysis it was found that during SACI operation, charge compression heating from boundary work and reaction front heat release combined to increase the end-gas temperature and initiate end-gas auto-ignition, providing significant control over the combustion process. Manipulation of the flame front heat release by varying intake temperature, spark timing, and dilution composition was demonstrated to allow control over peak combustion heat release rates independent of combustion phasing, enabling reduced peak heat release rates with increased load and efficiency. The primary influences on end-gas heat release rate were the total end-gas mass and the temperature stratification in the end-gas prior to auto-ignition, which were seen to evolve significantly during the flame propagation phase prior to auo-ignition. Insights from this work can be used to guide SACI operating strategies to enable high efficiency engine operation at higher power density than with HCCI combustion.

Chapter 1
Introduction

A common motivator for automotive engine development is the pressure to continually increase engine operating efficiency. In recent years the combination of tightening legislative standards for vehicle fleet fuel economy as well as increasing consumer awareness of vehicle efficiency as fuel prices rise have driven engine manufacturers to consider a variety of advanced engine technologies and operating strategies. One such strategy that has received considerable attention is Homogeneous Charge Compression Ignition (HCCI), which offers the potential for high efficiency operation with low emissions. However, controllability issues have limited HCCI to low load operation and prevented it from being implemented in mass produced vehicles. These challenges have shifted industry attention to another combustion strategy, Spark Assisted Compression Ignition (SACI), in an attempt to realize the benefits of HCCI while overcoming its limitations.

1.1 HCCI Background and Challenges

Homogeneous Charge Compression Ignition (HCCI) is a combustion strategy that was developed to address the need for high efficiency engines with low pollutant emissions. An HCCI engine operates un-throttled with an ultra dilute premixed fuel-air charge in a relatively un-modified Spark Ignition (SI) engine typical of many current automotive applications. The fuel-air charge is compressed to the point of end-gas auto-ignition and combustion occurs without any external trigger, either from a spark plug as in an SI engine, or through the injection of additional fuel as in a Diesel engine [1–3]. Under ideal operation combustion

begins near Top Dead Center (TDC) and the auto-ignition event occurs rapidly, in a nearly constant volume manner. The tradeoffs between expansion work, compression work, and heat transfer losses dictates that peak thermal efficiency is achieved when combustion is phased slightly after TDC [4, 5]. However, the lack of a direct mechanism to control combustion phasing makes maintaining such combustion phasing problematic.

An HCCI engine offers several thermal efficiency benefits over a more traditional SI engine. To meet emissions requirements for NO_X, CO, and unburned hydrocarbons, SI engines operate at a constant equivalence ratio of 1.0, and utilize a three-way catalyst (TWC) to reduce engine out emissions to the extremely low levels required for tailpipe standards [6]. Load control in an SI engine is accomplished by throttling the intake air and reducing the fueling rate to maintain stoichiometric operation, leading to high pumping losses during low load operation. In contrast, an HCCI engine operates un-throttled and controls load by adjusting fueling rate, while equivalence ratio varies. The pumping losses associated with throttling are avoided, increasing work output and engine efficiency [7].

The high levels of charge dilution utilized in an HCCI engine limit peak cylinder temperatures enough that at low loads engine-out NO_X concentrations are low enough to meet emissions regulations without expensive and complicated dedicated NO_X after-treatment systems [3, 7]. As HCCI load increases and peak temperatures rise, the engine out NO_X emissions also rise past the levels mandated by the emissions standards. Under these conditions an HCCI engine can be operated stoichiometrically by utilizing exhaust gas recirculation (EGR) for dilution, thereby enabling a common inexpensive TWC to eliminate the engine out NO_X. The low burned gas temperatures in an HCCI engine increase the ratio of specific heats in the charge, leading to significant increases in indicated thermal efficiency [8, 9]. Another effect of reduced charge temperatures is a reduction in heat transfer losses to the cylinder walls, further increasing HCCI engine efficiency [10]. Finally, the higher compression ratios typically used in HCCI engines to promote auto-ignition, relative to SI engines, also increase thermal efficiency [9].

Early imaging experiments of HCCI combustion in the 1970's and 1980's established that HCCI combustion was primarily chemically controlled and lacked structured reaction fronts [1, 11, 12]. High speed chemiluminescence and Schlieren imaging studies [1, 11] showed nearly constant charge density in the combustion chamber, without the characteristic sharp density gradients and high radical species structures observed during SI combustion. A more recent Planar Laser Induced Fluorescence (PLIF) imaging study [13], as well as a chemiluminescence study [14], showed HCCI combustion occurring in a sequential auto-ignition process, beginning in hotter locations near the center of the combustion chamber and proceeding outward into colder less reactive regions while simultaneously increasing the temperature of the colder regions through compression heating. The resulting distribution of auto-ignition reactivity leads to the fast, but not instantaneous, combustion rates observed during HCCI operation, where burn durations are typically between 5-15 crank angle degrees ($^\circ$ CA) [15]. Experiments have shown that decreasing the wall temperature can increase the resulting HCCI burn duration [14], while computational studies have also shown longer burn durations and thermal stratification increases [16].

The chemically controlled nature of HCCI combustion presents a difficult control problem for stable engine operation. The ignition timing is determined by the local thermodynamic state and reactivity of the fuel-air mixture near TDC, which is in turn dependent on the mixture state at intake valve closing (IVC), as well as the charge temperature history during the compression process [17]. While variables such as the intake manifold temperature (T_{intake}), compression ratio, intake manifold pressure, fuel composition, equivalence ratio, EGR rate and engine speed all influence the mixture state at TDC, not all of these variables are practical to adjust in an automotive application [12, 18–21]. In practical engine applications where intake manifold heating is not possible and compression ratios are similar to those found in typical SI engines, advanced valve control strategies are often used to control charge temperature [21–25]. The most common operating strategy uses negative valve overlap (NVO), whereby the exhaust valves are closed early in the exhaust

stroke, trapping some volume of hot internal EGR (iEGR) in the combustion chamber for the subsequent engine cycle [23]. As the valve timing is adjusted this residual fraction can be controlled and used to manipulate the charge state at IVC, with larger residual fractions leading to increased temperatures and advances in combustion phasing.

Much of the behavior of HCCI is tied closely to the combustion phasing, including burn rate and duration [25]. As charge temperature increases and combustion phasing advances, peak cylinder temperatures and pressures increase, burn duration decreases, and pressure rise rates correspondingly increase [26, 27]. Two combustion phasing limits exist for HCCI operation at a given load, an advanced phasing limit where pressure rise rates increase and excessive ringing can damage engine components [27–29], and a late phasing limit where combustion becomes unstable [23, 30, 31]. At both limits, the use of NVO and large internal residuals increases cycle to cycle variability and can cause undesirable behavior [32]. On the advanced side, in addition to the previously mentioned ringing limits, cycles with excessively advanced combustion phasing also have higher peak temperatures and can generate sufficient NO_X to exceed the tailpipe standards [27]. On the late side, misfiring cycles with low combustion efficiencies can leave excess fuel in the residual and significantly advance the phasing of the subsequent cycle and lead to heavy ringing [32].

As HCCI load is increased these two phasing limits converge, such that at the high load operating limit small variations in the in-cylinder state can lead to either excessive ringing or misfire [29, 30, 33]. Many experimental studies have shown the high load limit of HCCI operation to be approximately 4-5 bar $IMEP_g$ under naturally aspirated conditions with equivalence ratios of $\Phi \approx 0.5$ [22, 29, 34, 35]. This limits HCCI operation to low load operation relative to the required full range of an engine in an automotive application [7, 34, 36, 37]. Under these conditions peak combustion temperatures can be high enough to require NO_X aftertreatment, and are typically operated stoichiometrically with up to 60% EGR dilution [38]. At the low load limit of HCCI operation, the start of end-gas auto-igntion has been shown to be governed primarily by thermal decomposition of H_2O_2

into OH [39], requiring that the end gas reach temperatures in the 850 k to 1200 K range to initiate thermal runaway. This reaction is also a key pathway for diesel combustion, end gas knock, and laminar flame chemistry [39–43]. Additional work has shown that peak burned gas temperatures must reach 1500 K for the HCCI combustion process to complete [44].

A variety of strategies have been investigated to expand the high load operating range of HCCI combustion. Most strategies involve delaying phasing and reducing burn duration to avoid the ringing intensity limits and NO_X issues at advanced combustion phasing [45]. However the methods used to manipulate burn durations vary.

Cooled external EGR has shown mixed results for increasing load. Simple computational studies have shown that the addition of EGR has a primarily thermal effect, decreasing TDC temperatures and delaying phasing relative to air dilution [46]. Increasing intake temperature to match phasing resulted in a slight decrease in the burn duration [47], behavior which was attributed to a reduction in the mixture oxygen. More detailed CFD studies of HCCI combustion [16] and experimental investigations [5,20,48] have also replicated this behavior. However, other experimental studies showed a 20% increase in load and a doubling of burn duration as EGR dilution was increased from 0% to 55% [49].

Optical engine investigation by Rothamer on the impact of internal residual from NVO operation on HCCI compositional stratification have shown that internal residual introduces significant thermal and compositional stratification relative to PVO operation [50]. A simulation study by Kodavasal [16] investigated the impact of NVO operation and charge preparation strategy on HCCI combustion. Charge stratification from NVO operation was observed to increase HCCI burn duration by 30% relative to PVO operation, with the impact of thermal stratification greatly outweighing the impact of compositional stratification. Experimental work with fixed valve timing has shown similar sensitivity to changes in thermal stratification [14, 15], while increasing thermal gradients by using coolant temperature showed that a 50 K drop in wall temperature had a 1° lengthening of burn duration and a 15% drop in ringing intensity [45]. However, increased heat losses

reduced combustion efficiency significantly more and this hurt efficiency more than simply reducing intake temperature to retard phasing by 1°. Additional experimental studies of compositional stratification under PVO operation showed marginal improvement in load (10%) in one case [51], and significant improvement enabling loads up to 16 bar BMEP in another case [52].

Another possible load extension strategy is intake boosting, increased charge densities can help overcome high dilution levels required for HCCI operation. Dec et al. have demonstrated the ability to increase the HCCI high load limit from 5 bar IMEP to 16.3 bar IMEP using EGR dilution and 325 kPa intake pressure [34]. Dilution with EGR was required to manage ringing intensity and maintain optimal combustion phasing, demonstrating a higher operating limit than boosting with air dilution alone, where boost pressures were limited to 180 kPa. Another study by Olsson et al. achieved 16 bar BMEP in a multi-cylinder HCCI engine running 300 kPa intake pressure [53]. Christensen and Johansson have also demonstrated a 16 bar limit for boosted HCCI with 250 kPa intake and 48% EGR [19].

While boosting shows potential for increasing the HCCI load limit, it exhibits the controllability and stability problems noted for naturally aspirated HCCI. A simpler and more flexible strategy is desired instead.

1.2 SACI Background

Spark Assisted Compression Ignition (SACI) is a method of triggering HCCI combustion using an external ignition source [54]. Adding a spark event provides direct control over the combustion process and has been used to improve stability at low loads [55, 56], as well as to enable higher load operation than is available through HCCI [29, 57–60]. Load extension was accomplished through the combined use of NVO, direct fuel injection, and stoichiometric operation with both internal and external EGR.

During SACI combustion, a spark event is used to initiate flame propagation similar

to that found in an SI engine, in an ultra dilute mixture with elevated temperatures similar to that of an HCCI engine [54]. As the flame front propagates and releases fuel energy, it introduces additional compression heating and drives the end-gas to the point of auto-ignition earlier than it would have without the contribution of spark assist [54]. Optical engine studies have supported this description of SACI combustion, where structures that appear to be flames are seen originating at the spark plug gap and propagating outward throughout the combustion chamber [61–64]. The flame propagation phase is then followed by volumetric ignition in front of the flame, resembling images of HCCI combustion [65]. Global heat release analysis of metal engine SACI experiments also supports the same conceptual picture of SACI operations, where initial heat release rates are low, characteristic of turbulent flame propagation in an SI engine, before transitioning sharply to short rapid heat release rates characteristic of end-gas auto-ignition [29, 48, 62, 63, 66, 67].

Simulation studies of Martz et al. have shown that the reaction fronts with moderate burning velocities can exist across much of the SACI operating regime [68], and that the transition from flame propagation to auto-ignition is abrupt [69, 70], with the flame providing negligible heat release after the end-gas has reached 1200 K. Additional simulations using the PREMIX code [71] by other researchers have also predicted the presence of laminar flames under SACI combustion conditions [66]. The simulations agree well with reaction front expansion speeds observed in optical engines during SACI combustion 2-5 m/s [61], 1.9-4.3 m/s [64], and 0.5-10 m/s [62].

1.3 Understanding SACI Combustion

The HCCI, SACI, and SI combustion regimes utilized by modern internal combustion engines can be classified using a conceptual diagram which delineates the regimes in terms of T_u, the unburned gas temperature near TDC, and T_b, the corresponding constant pressure adiabatic temperature. Figure 1.1 shows the Multi-Mode Combustion Diagram (MMCD)

of Lavoie et al. [54], presented here at 40 bar, where the boundaries for each combustion regime are based on the limits for ignition, flame propagation [72, 73], knock [74, 75], and bulk quenching [44]. The dashed line at 2200 K (residual gas fraction) and the solid line at 2000 K (air) represent the approximate T_b's corresponding to NO_X emissions of 1 g/kg fuel; beyond which NO_X aftertreatment is typically required. The oblique lines represent burned gas temperatures for different values of Φ', the fuel-to-charge equivalence ratio. The circles shown on the diagram are SI combustion experiments [73], the triangles are HCCI combustion experiments [44, 76] and the dashed ovals are SACI experiments [22, 23, 65, 66, 77, 78]. The area most relevant for this work is near the autoignition boundary, which defines the lowest unburned temperature at which autoignition will occur in the absence of any significant energy release by other parts of the charge. This line slopes toward lower unburned temperatures at high Φ' as ignition delay times are reduced with increasing fuel concentration. To the right of this line is the HCCI autoignition regime, while to the left are the SI and SACI regions. Laminar flame behavior near this line is of particular interest for SACI operation.

Experiments moving across the SACI regime from low load to high load exhibit a transition from behavior that appears dominated by end gas auto-ignition at low loads, to behavior dominated by flame propagation at high loads, indicating that there is an orderly transition across the SACI regime [23, 29, 60]. Such transition behavior offers the potential for high efficiency operation across the entire engine load range encountered during a vehicle drive cycle, from low load idle to full load acceleration [37, 79]. Many of the factors previously discussed influencing HCCI combustion, including valve strategy choices and mixture thermal and compositional stratification, will also be present during SACI operation. Any detailed investigation of SACI combustion will need to properly account for the impact of these factors on the behavior of both modes of combustion. For example, an optical engine study showed that as negative valve overlap was increased, auto-ignition phasing advanced due to higher temperatures while the flame front expansion speeds decreased as

the dilution method changed [62]. Other optical studies observed increases in the flame front speeds as intake heating increased [64], consistent with laminar flame studies under similar conditions [68].

Many practical experimental investigations of SACI in metal engines have utilized significant internal and external EGR dilution to provide the charge preheating required for successful operation, as well as to avoid problems with NO_X emissions [57–60, 67]. Unfortunately there is a lack of fundamental knowledge of laminar burning velocity under high temperature highly EGR dilute conditions. Engine studies can provide some insight but the effects of EGR are difficult to de-couple from the thermal and compositional changes associated with such operation. While simulation studies have investigated the behavior of air dilute reaction fronts in the SACI regime [68], additional fundamental insight is needed under practical operating conditions.

Recent SACI simulation studies have investigated the impact of wall temperature and intake temperature effects on SACI combustion behavior [80]. Increasing wall temperature was shown to increase peak heat release rate, while increasing intake temperature exhibited a much stronger effect on phasing for a similar change in boundary condition temperature. A simplified stratification analysis showed that increasing the wall temperature decreased the thermal stratification in the charge and lead to higher rates of heat release. On the other hand increasing the intake temperature was predicted to increase thermal stratification while advancing phasing. An experimental study of the impact of compositional stratification on SACI combustion showed that adding additional fuel in the vicinity of the spark plug increased the flame propagation rate and allowed operation at higher loads than with a more homogeneous charge [58].

Experimental studies have shown increasing early rates of heat release with increasing spark advance, while simultaneously decreasing peak heat release rates at constant phasing [57, 67]. In both studies SACI was used to reduce ringing, and spark advance exhibit a measure of control over the auto-ignition burn duration. A similar investigation

adjusting the mixture dilution composition showed that decreasing EGR increased the auto-ignition burn duration, a trend opposite of that observed for pure HCCI operation [48].

The inclusion of spark assist allows for robust and direct control over dilute high efficiency combustion, without significant hardware changes from an HCCI or SI engine. While this presents the possibility of improving engine efficiency through unthrottled operation across a wide load range in a multi-mode engine with transient mode switching, additional fundamental understanding is required to implement such systems.

1.4 Modeling SACI Combustion

There are an assortment of models in the literature that are applicable to modeling and understanding SACI combustion processes. Simple zero and one dimensional models of knocking SI combustion use empirical expressions for the burning velocity and knock integrals to estimate the onset of end-gas auto-ignition [81]. More recent work by Ortiz-Soto has developed a quasi-dimensional SACI combustion model which uses single zone chemical kinetics to predict auto-ignition timing, while using an empirical model for auto-ignition burn rate [37]. Such simple models were developed for 1-D cycle simulations and lack the fidelity required to capture the effects of direct injection and charge thermal and compositional stratification. As a result they are not appropriate for detailed investigations of SACI combustion behavior.

More complex multi-dimensional CFD models are available that can provide the required spatial resolution for detailed SACI studies. One popular model framework is the G-Equation interface tracking method, which has been used to model knocking SI combustion with detailed chemical kinetics in the end-gas [82, 83]. More recently the same approach has been used by Dahms et al. to study spark ignition in the SACI combustion regime under stratified charge conditions [84–86]. Some major drawbacks to the G-Equation approach are the reliance on empirical expressions for the turbulent flame speed [87], and the high

computational cost of detailed chemical kinetics calculations in every cell.

Another multi-dimensional CFD approach is the Coherent Flamelet model [88] for SI combustion with end-gas knock [89, 90]. Some of these approaches have used tabulated lookup tables from homogeneous ignition simulations with detailed kinetics to predict end-gas knock [89, 91, 92], while others have used knock integrals to determine the auto-ignition timing [93]. A similar Coherent Flamelet approach has recently been used by Wang et al. to model SACI combustion [80], however their formulation lacked a chemical source term for reaction progress in the end-gas, which can affect the transition from flame propagation to auto-ignition within each computational cell.

Many previous studies, with both the G-Equation and the CFM model, have used isooctane air laminar burning velocity data from Metghalchi and Keck [94] to estimate flame speeds under SACI conditions. The authors of those studies did not have access to laminar flame speed data under highly dilute mixtures typical of SACI operation, and were forced to extrapolate the Metghalchi and Keck data from its original equivalence ratio range of 0.8 to 1.5 to a wider range of 0 to 3, either linearly or by refitting with another functional form [89, 91, 92, 95, 96].

Another shortcoming of previous studies is the choice of combustion mode for each cell. Some assume that combustion in a cell is governed entirely by either reaction front propagation or by homogeneous ignition, switching combustion models based on a Dahmköhler number or other criteria [80, 82, 97]. Simultaneous contributions of both modes in a single cell are then often neglected.

Recent modeling efforts at the University of Michigan have developed a KIVA based SACI combustion model (KIVA-CFMZ) combining the Coherent Flamelet model with a Multi-Zone model for detailed end-gas chemistry [70, 98, 99]. Detailed simulations of laminar flame propagation under highly dilute mixtures were used to develop correlations for laminar burning velocity and flame thickness under the highly dilute, high preheat temperature conditions in the SACI regime for use in KIVA-CFMZ [68]. The KIVA-CFMZ

model was used to study air dilute SACI combustion and produced excellent agreement with air dilute optical engine experiments [61, 70].

1.5 Objective and Document Organization

The primary objective of the current work is to improve fundamental understanding of the physical processes governing SACI combustion behavior. While existing experimental studies of SACI combustion have demonstrated the ability to address the ignition timing and peak combustion rate control issues associated with HCCI, as well as simultaneously increasing load and power density, there is a lack of fundamental SACI simulation studies in the literature. A goal of the current work is to develop and validate a detailed model capable of capturing SACI combustion behavior under operating conditions similar to those seen in SACI experiments, including dilution with high levels of internal EGR through NVO operation. The model will serve as a predictive tool for investigating potential applications of SACI combustion as well as a diagnostic tool to assist in interpreting the results of SACI combustion experiments.

This document is organized as follows:

- Chapter 2 addresses the lack of laminar burning velocity and front thickness data in the highly dilute, high preheat temperature SACI combustion regime for conditions diluted with EGR. Laminar reaction front simulations are performed for highly EGR dilute conditions to obtain laminar burning velocity and flame thickness data as well as to investigate the behavior of reaction fronts at high EGR levels. Correlations of burning velocity and front thickness are developed from these data.

- Chapter 3 describes the implementation of a detailed CFD model for SACI combustion in KIVA-3v. A previously developed SACI model (KIVA-CFMZ) is extended to account for charge preparation effects during open cycle breathing. The model includes previously developed physically based sub-models for reaction front propagation and end-gas auto-ignition, as well as newly included models for direct fuel injection and vaporization and a method of tracking EGR dilution throughout the combustion process.

- Chapter 4 presents the results of validation studies of the SACI combustion model against metal engine experimental HCCI, SI, and SACI combustion data. The model configuration and tuning procedure is discussed and the metrics used to compare model predictions to experimental SACI combustion data are presented.

- In Chapter 5 the KIVA-CFMZ model is used to study the behavior of SACI combustion at constant composition as the fractions of heat release due to flame propagation and auto-ignition are varied to control peak combustion rate.

- In Chapter 6 the KIVA-CFMZ model is used to study the impact of dilution composition on the balance between flame propagation and auto-ignition and the resulting heat release rate.

- Finally, Chapter 7 summarizes the conclusions of this work and provides suggestions for future studies.

Publications

The topics discussed in this dissertation have also been reported in the following publications [68, 69, 100–102]:

J. B. Martz, **R. J. Middleton**, G. A. Lavoie, A. Babajimopoulos, and D. N. Assanis. *A computational study and correlation of premixed isooctane air laminar reaction front properties under spark ignited and spark assisted compression ignition engine conditions.* Combustion and Flame, 158(6):1089–1096, 2011.

J. B. Martz, G. A. Lavoie, H. G. Im, **R. J. Middleton**, A. Babajimopoulos, and D. N. Assanis. *The propagation of a laminar reaction front during end-gas auto-ignition.* Combustion and Flame, 159(6):2077–2086, 2012

R. J. Middleton, J. B. Martz, G. A. Lavoie, A. Babajimopoulos, and D. N. Assanis. *A computational study and correlation of premixed isooctane air laminar reaction fronts diluted with EGR.* Combustion and Flame, 159(10):3146–3157, 2012.

J. B. Martz, **R. J. Middleton**, G. A. Lavoie, M. Fatouraie, B. Zigler, M. S. Wooldridge, A. Babajimopoulous, and D. N. Assanis. *Modeling spark-assisted compression ignition combustion in an optical engine.* Submitted for Review: 35th Symposium (International) on Combustion, 2014.

R. J. Middleton, J. B. Martz, L. K. M. Olesky, G. A. Lavoie, M. S. Wooldridge, and D. N. Assanis. *The effect of spark timing and negative valve overlap on spark assisted compression ignition combustion heat release rate.* 35th Combustion Symposium, Submitted for Publication, 2014

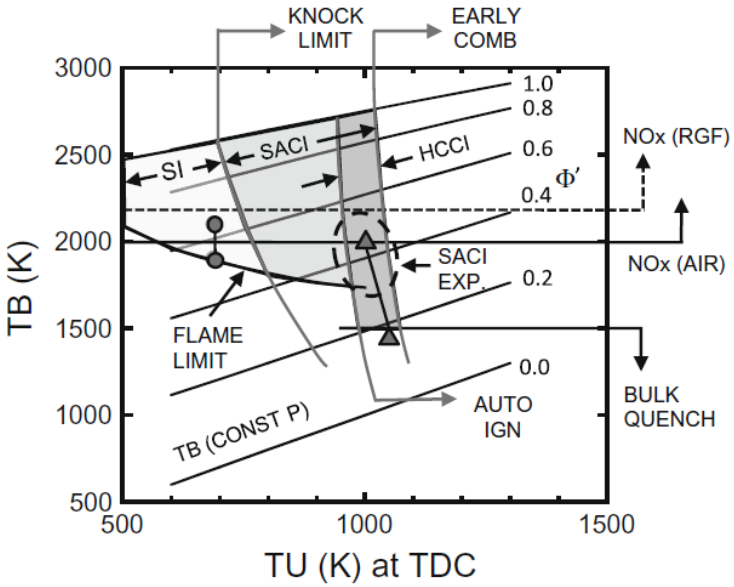

Figure 1.1 Multi-mode combustion diagram showing SI, SACI and HCCI combustion regimes in terms of TDC unburned temperature T_u, and burned gas temperature T_b for isooctane in air. Oblique lines are at constant fuel to charge equivalence ratio Φ'. The NO_X limit of 1 g/kg fuel is shown for air dilution as a solid line, for stoichiometric EGR dilution as a dashed line. Combustion regimes are separated based on limits for ignition, flame propagation, knock, bulk quenching and NO_X limit. Figure reproduced from Lavoie et al. [54].

Chapter 2

Laminar Flame Behavior under EGR Dilute Conditions

This Chapter investigates the propagation of premixed laminar reaction fronts for mixtures of isooctane-air and recirculated combustion products (or EGR) under high pressure and temperature conditions relevant for SACI combustion. The investigation uses a transient one-dimensional flame simulation with a skeletal 215 species chemical kinetic mechanism to generate laminar burning velocity and front thickness predictions. The simulation was exercised over fuel-air equivalence ratios, unburned gas temperatures, pressures and EGR levels ranging from 0.1 to 1.0, 400 to 1000 K, 1 to 250 bar, and 0 to 60% (by mass) respectively, a range extending beyond that of previous researchers. Steady reaction fronts with burning velocities in excess of 5 cm/s could not be established under all of these conditions, especially when burned gas temperatures were below 1450 K and/or when characteristic reaction front propagation times were on the order of the unburned gas ignition delay. For a given pressure, T_u and T_b, the burning velocity of an EGR dilute mixture was found to be lower than that of an air dilute mixture, with the decrease in burning velocity attributed primarily to the reduced oxygen concentration's effect on chemistry. Steady premixed laminar burning velocities were correlated using a modified two-equation form based on the asymptotic structure of a laminar flame, which produced an average error of 3.4% between the simulated and correlated laminar burning velocities, with a standard deviation of 4.3%, while additional correlations were constructed for reaction front thickness and adiabatic flame temperature. These correlations provide key inputs for modeling turbulent flame propagation during SACI combustion. The work presented in this

chapter has been published in Combustion and Flame [100] and is an extension of the a similar study focused on air dilute conditions [68].

2.1 Background

Modeling the deflagration portion of SACI combustion requires accurate expressions for laminar burning velocity (S_L) [70, 103–105]. While the primary fuel for automotive HCCI and SACI applications is gasoline, its kinetic, thermophysical and transport properties are variable and ill-defined [106]. As a result, isooctane is frequently used as a gasoline surrogate given the comparable laminar burning velocities [107] and ignition delays [75] of the two fuels.

Previous experimental studies conducted by Metghalchi and Keck [94], Ryan and Lestz [108], Bradley et al. [109] and Jerzembeck et al. [107], have investigated the behavior of isooctane laminar burning velocity over a range of conditions relevant for traditional spark ignited engine operation. Computational studies by Göttgens et al. [110] and Müller et al. [111] have examined laminar flames over a wider range of SI engine conditions. Recent previous work conducted at the University of Michigan studying air dilute flames has significantly extended the range of simulation conditions to include the very dilute high temperature mixtures typical of HCCI and SACI engines [68]. The ranges of the above studies are shown in Table 2.1. These studies have focused primarily on conditions diluted with excess air, whereas the investigation of conditions diluted with EGR has been rather limited. Metghalchi and Keck diluted stoichiometric mixtures with a 15/85% blend of CO_2/N_2 at diluent mass fractions of 0.1 and 0.2 [94], whereas Ryan and Lestz conducted stoichiometric experiments with the same dilution blend up to diluent mass fractions of 0.3 [108]. Rhodes and Keck [112] studied indolene-air flames diluted with a 20/80% blend of CO_2/N_2 for equivalence ratios from 0.7 to 1.2 and diluent volume fractions up to 30%. More recently Jerzembeck et al. [107] approximated EGR dilution by reducing the concentration

of O_2 in synthetic air, while Zhao et al. [113] and Tang et al. [114] have investigated the behavior of propane-air flames at atmospheric pressure over a range of equivalence ratios diluted with N_2. Concurrent with the preparation of the current work, Marshall et al. [115] used a combustion bomb to investigate isooctane flames diluted with up to 30% trapped residuals. In the absence of correlations for flame speed and thickness for conditions diluted with EGR, Dahms et al. [116] used a laminar flame simulation to generate these values for a range of engine relevant conditions with EGR; the simulation results were used directly in an engine modeling study and were not explicitly reported.

The primary objective of the current chapter is to extend the premixed reaction front simulation database and correlations of premixed laminar burning velocity and front thickness from previous work to include SI and SACI mixtures diluted with EGR. The results will allow for better understanding of the behavior of reaction fronts under low temperature combustion conditions diluted with air and/or EGR. A one dimensional laminar flame simulation was used to produce laminar isooctane-air reaction fronts in mixtures diluted with combustion products representative of EGR, over a range of conditions relevant to both SACI and SI combustion. Steady laminar burning velocity data were correlated using a two equation asymptotic fit. Correlations were also developed for steady laminar reaction front thickness and adiabatic flame temperature.

2.2 Simulation Details

Planar laminar isooctane-air-EGR reaction front simulations were performed at constant pressure with HCT [117], which solves the one dimensional momentum, species and energy transport equations. HCT has been used for the development and validation of kinetic mechanisms [42, 118–121] and for the simulation of both transient and steady state laminar flames [40, 41, 122, 123]. All simulations discussed in this work were configured to be consistent with a previous study [68], visualized as a reaction front propagating through a one

dimensional tube with a closed adiabatic boundary on the unburned side of the reaction front and an open constant pressure boundary on the burned side. The chemical mechanism used in the simulations was the skeletal 215 species isooctane mechanism of Tham et al. [124], which was derived from the detailed mechanism of Curran et al. [42]. Mixture average mass and thermal transport properties were calculated with the Sandia TRANSPORT [125] routine, while conductive and radiative heat losses to the ambient were neglected. A 75 cell grid was used for all reaction front calculations; a fine mesh was produced in the vicinity of the reaction front with 30 adaptive grid cells. Mixture thermal conductivity was scaled by a factor of 0.8, reducing atmospheric burning velocities by approximately 10% to match experimental results, consistent with previous simulation validation [68]. Unless otherwise noted, fresh air composition for all simulations was one mole of molecular oxygen per 3.76 moles molecular nitrogen, while recirculated exhaust gas (EGR) concentration was defined on a mass basis and composed of complete combustion products (CO_2, H_2O, O_2, and N_2) at the same equivalence ratio as the fuel-fresh air mixture. All simulations were conducted at constant pressure to eliminate the effects of engine timing and overall energy release on the unburned conditions. Initial reaction front profiles were obtained from estimates of the temperature and species jump across the reaction front; the initial burned gas species and temperatures were determined from constant pressure equilibrium calculations. The reaction front was then allowed to develop in time, resulting in one of three outcomes: steady flame propagation, auto-ignition of the end-gas accompanied by a reaction front acceleration, or bulk quenching.

Consistent with previous work, the laminar burning velocity, S_L, was found using the reaction front velocity in the laboratory frame, S_b, which was defined as the time rate of change of the reaction front position at the location of the average temperature between the maximum temperature within the HCT domain ($T_{\max}$) and the temperature of the unburned gas (T_u). The burning velocity at the reaction front position, S_f, was obtained from the gas velocity, u_f, at the reaction front position and S_b, where $S_f = S_b - u_f$. The premixed

laminar burning velocity, S_L, was obtained via the application of the continuity equation through the use of the density at the reaction front position and of the unburned gas, ρ_f and ρ_u, where $S_L = \rho_f S_f / \rho_u$ for quasi-steady front propagation. When steady, the burning velocities predicted by this approach are essentially identical to those calculated with the expression $S_L = S_b$ [40].

The results and correlations presented in the current work are for steady reaction fronts only, which typically required between 8-10 front thicknesses of travel to achieve steady propagation. Steady data were obtained by allowing the transient HCT solution to evolve in time until the laminar burning velocity was within the larger of either 0.01 cm/sec or 0.1% of the moving average of the previous 10 calculated values. The simulations were allowed to continue beyond the steadiness criteria as a safeguard against false convergence, typically for an additional 50 to 150 steady points. If the unburned gas temperature rose in excess of 0.5% of its initial value, the transient simulation was then considered unsteady and auto-igniting; conditions where converged steady propagation was not observed prior to auto-ignition are not included in the following results and correlations.

2.3 Simulation Validation

The HCT simulation configuration and chemical mechanism were previously validated for air dilute conditions against the high pressure ignition delay data of Davidson et al. [126] and Shen et al. [127], as well as against the elevated pressure laminar burning velocity data of Bradley et al. [109] and Jerzembeck et al. [107], data which were stretch corrected and determined prior to the onset of hydrodynamic instabilities. Further validation was conducted against the stretch corrected atmospheric pressure burning velocity data of Kumar et al. [128] and Davis and Law [129]. Good agreement was observed between the HCT simulation predictions and the experimental data, with detailed discussion provided in a previous publication [68].

Prior to conducting the current investigation, the applicability of the HCT simulation configuration to EGR mixtures was determined through comparisons against the indolene-air laminar burning velocity data from the combustion bomb experiments of Rhodes and Keck [112]. The diluent in the experiments and simulations was composed of a 20/80% mixture of CO_2/N_2 (on a volume basis), chosen to match the heat capacity of stoichiometric indolene combustion products. The experimental data cover equivalence ratios Φ from 0.7 to 1.2 and dilution fractions X_d from 0 to 30% (by volume). Experimental initial conditions were T_u = 350K, and p_i = 1 or 2 atm, with transient increases in T_u and p due to compression heating of the end gas until conditions of T_u = 500K and $p = 4p_i$ were reached. HCT simulations were conducted at conditions corresponding to both the initial state and final state of the experiments, with both sets producing similar reductions in burning velocity with dilution. Figure 2.1 shows good agreement between the indolene experimental data and isooctane HCT simulation results, with normalized burning velocity ($S_{L,\text{Diluted}}/S_{L,\text{Undiluted}}$) decreasing nearly linearly with increasing dilution X_d. Rhodes and Keck reported that the fractional decrease in S_L with dilution was independent of Φ, T_u and p, behavior which is confirmed by the HCT simulations, as a result these variables are omitted from the Figure for clarity.

A lack of experimental flame data at the highest pressures in the current study complicates the process of validating the simulation configuration and chemical mechanism, particularly at pressures above 100 bar where non-ideal gas behavior becomes possible. However, simulations of laminar premixed methane flames using the Redlich-Kwong equation of state for real gases with high pressure kinetics modifications have shown only slight decreases in burning velocity compared to an ideal gas formulation for pressures up to 150 atm under low temperature conditions [130]. Laminar diffusion flame simulations have shown very similar peak flame temperatures between real gas and ideal gas formulations up to pressures of 300 bar [131], with the ratio of real to ideal gas properties approaching 1 in the high temperature region of the flame. These results imply that under the high temperature and high pressure

conditions expected in boosted SACI engine applications the ideal gas approximation is appropriate.

2.4 Simulation Dataset Range

A total of 2750 constant pressure laminar burning velocity simulations were performed with Φ, T_u, pressure and EGR ranging from 0.1 to 1.0, 298 to 1000 K, 1 to 250 bar, and 0 to 60% by mass, respectively, as shown in Table 2.2, (298K simulations conducted only at 0% EGR). The current simulations extend those discussed in our previous study [68], investigating the influence of EGR dilution on flame properties over a wide operating range. Of the simulated conditions, 1095 produced steady laminar reaction fronts that were used for the correlation of laminar burning velocity and thickness. Consistent with Göttgens et al. [110], Müller et al. [111], and our previous work [68], laminar burning velocities under 5 cm/s were not included in the correlation. This metric was previously developed to compensate for the lack of external heat losses and other effects not captured by the ideal nature of the computations, in particular, for those simulations performed near the flammability limit [41]. Of the 1655 conditions not included in the correlation, 129 had converged steady laminar burning velocities of less than 5 cm/sec, while steady reaction fronts could not be produced for 458 conditions that auto-ignited, as discussed below, or for 1068 simulations performed under conditions where burned gas temperatures were less than 1450K. For these low flame temperature cases, reaction rates were too low to maintain a steady reactive-diffusive front structure and the front ultimately succumbed to bulk quenching.

Although transient reaction fronts with finite laminar burning velocities could be established under many conditions with burned gas temperatures above 1450K, the process of obtaining steady reaction fronts was complicated for conditions in which the ignition delay time of the unburned gas was short relative to the time required for the reaction front to become steady. These conditions corresponded primarily to high T_u, high pressure and

low fuel mass fraction (low Φ and/or high EGR), and resulted in significant burning velocity increases with reaction progress upstream of the front. These resulting transient data are not included in the steady burning velocity correlations of the current work, but were the subject of a separate study [69].

The range of conditions that produced steady reaction fronts with burning velocities in excess of 5 cm/s was found to depend on the EGR level in addition to the dependencies on pressure, T_u and Φ noted in previous work. Increasing the level of EGR dilution decreased the range where steady fronts could be obtained, until at 60% EGR no conditions with pressure above 15 bar produced steady flames with speeds above 5 cm/s. Steady flames were observed for conditions where T_b exceeded 1450K, the predicted S_L exceeded 5 cm/s, and ratio of ignition delay time to flame time was greater than 10.

2.5 Effect of Dilution Method on Reaction Front Behavior

It is widely accepted that the S_L of a hydrocarbon fuel is a strong function of T_b, which depends on the quantity of air and/or EGR dilution in the mixture [43]. While multiple studies have documented the influence of EGR dilution on S_L [94, 107, 108, 112–114], the potential thermal, transport, and chemical differences associated with the dilution method, all of which may affect S_L, were not decoupled. In an attempt to better understand these effects, lean mixtures diluted with air are compared to stoichiometric mixtures diluted with EGR at the same initial p and T_u. The T_b of the mixture is adjusted through the charge energy content, defined for both air and EGR dilute mixtures with Φ', the fuel-to-charge equivalence ratio given by Equation 2.1 [54]:

$$\begin{aligned}\Phi' &= \frac{(F/(A+R))}{(F/A)_{st}} = \frac{\Phi(1-Y_{\mathrm{EGR}})}{1+Y_{\mathrm{EGR}}\Phi(F/A)_{st}} \\ &\approx \Phi\,(1-Y_{\mathrm{EGR}})\end{aligned} \tag{2.1}$$

where F, A, and R, are the masses of fuel, air, and residual gas, the subscript st indicates stoichiometric conditions, and Y_{EGR} is the mass fraction of EGR.

Figure 2.2(a) compares the burning velocities of lean air dilute mixtures with those of stoichiometric, EGR dilute mixtures as a function of Φ', with T_u = 900K and p = 15 bar. At a given Φ', the S_L of the air dilute mixture exceeds that of the EGR dilute mixture. Also at a given Φ', the difference in T_b between the two mixtures shown in Figure 2.2(b) is caused by variations in the mixture heat capacity [46]. While a ≈ 0.05 shift in Φ' brings T_b in line for the two dilution methods, a larger shift in Φ' is required to produce overlapping S_L's in Figure 2.2(a), without resolving the difference in slope between the S_L curves. Figure 2.3 re-plots select data from Figure 2.2 on a relative basis, showing the ratios of $T_{b,\mathrm{EGR}}/T_{b,\mathrm{Air}}$, $S_{L,\mathrm{EGR}}/S_{L,\mathrm{Air}}$, and the reactant mole fraction $X_{\mathrm{O_2,EGR}}/X_{\mathrm{O_2,Air}}$ plotted vs Φ'. The similarity between S_L and the reactant O_2 concentration ratios suggests that S_L is related to the mixture O_2 concentration as well as T_b.

To further understand the above variations in S_L with dilution method, an air dilute reaction front with Φ = 0.4 is compared to an EGR dilute front with Φ = 0.7 and 40% EGR. Both simulations are at T_u = 900K, p = 40 bar; other key parameters are given in Table 2.3. Slightly higher fuel mass fraction (3%) and Φ' (5%) are required to match the T_b of the EGR dilute front to the T_b of the air dilute case, due to a slightly higher mixture heat capacity (3%) with EGR dilution. Significant spatially dependent differences in the $X_{\mathrm{O_2}}$ exist between the air and EGR dilute reaction fronts, as shown in Figure 2.4(a). The respective decreases in $X_{\mathrm{O_2}}$ for the EGR dilute front at a given location (in parenthesis) were 29% (unburned gas), 33% (start of reaction zone), 47% (location of peak heat release), and 51% (burned gas). Here the start of the reaction zone is defined as the location where the heat release rate is 2% of the peak heat release rate, with the X location and temperature of these two locations varying slightly between the fronts. Although both reaction fronts have very similar temperature profiles as shown in Figure 2.4(b), there is a 17% decrease in the S_L of the EGR dilute case (23.2 cm/s) relative to the air dilute case (28.9 cm/s).

To assess the chemical kinetic influence of O_2 concentration on S_L, scaled HCT simulations were conducted with the initial conditions of the air dilute reaction front listed in Table 2.3. To isolate the kinetic impact of the O_2 differences between the air and EGR dilute flames in the scaled simulations, the X_{O_2} within HCT's kinetics subroutine was modified throughout the domain by multiplication with a fixed scaling factor; X_{O_2} was not modified in the conservation equations or within the transport subroutines. For these simulations, a scaling factor of 0.5 was selected in an attempt to approximate the ratio of $X_{O_2,EGR}/X_{O_2,Air}$ within the reaction zones of the flames, near the location of peak heat release. This scaling approach is similar to previous sensitivity analyses, where both the forward and reverse kinetic rate coefficients were scaled to determine the most important reactions for a given thermochemical process [42, 119–121]. All 164 reactions involving O_2 were investigated with individual simulations, with the X_{O_2} scaling applied to the single reaction consuming O_2. In addition, a combined scaling of all reactions consuming O_2 was performed.

Figure 2.5(a) shows the normalized burning velocities relative to the unscaled air dilute base case for the 5 reactions exhibiting the greatest influence on S_L, as well as the combined O_2 scaling study. The variations in S_L associated with the O_2 concentration change were strongest for the high temperature chain branching reaction ($O_2 + H \rightleftharpoons OH + O$) and the competing chain terminating reaction ($O_2 + H\,(+m) \rightleftharpoons HO_2\,(+m)$). Both of these reactions are most active in the high temperature region of the reaction front, close to the burned gas temperature, as shown in Figure 2.5(b). These results are consistent with previous studies identifying the importance of these reactions to flame speed and ignition delay [40–43]. The burning velocity of the combined scaling simulation decreased by 14% relative to the base case, similar to the 17% decrease in S_L observed for the EGR case relative to the air dilute case noted above. Repeating the combined scaling simulation with a multiplier 0.7, to approximate the X_{O_2} ratio near the start of the reaction zone, produced a 6% reduction in S_L. These results suggest that the sensitivity of S_L to dilution method noted above is in part a kinetic effect related to the mixture O_2 concentration.

2.6 Exhaust Gas Recirculation (EGR) Mixture Definition that Includes O_2

Traditional SI engines with port fuel injection operate with near stoichiometric conditions and relatively low EGR rates, resulting in very well mixed fuel-air-EGR charges. In these applications the EGR rate is typically defined as the mass of exhaust gas over the total mass in the cylinder, and is reported along with a global equivalence ratio. In contrast, many modern engines utilizing advanced combustion strategies such as HCCI, SACI, and DI-SI use direct in-cylinder injection and large residual fractions, posing a more complex problem. Here the local gas composition can potentially vary from point to point within the cylinder, partly due to non-uniform fuel distribution from the injector, and partly due to incomplete mixing of the residual with the fresh charge. In order to apply the findings of the previous sections to such engines, any correlations for flame properties must clearly account for the local fuel-air-EGR mixture composition; in particular, for the local fuel and O_2 concentrations.

Before proceeding, it is useful to introduce two definitions for the equivalence ratio of any gas mixture, which were first presented by Babajimopoulos et al. [132] and will be used in this analysis. The first is the global equivalence ratio Φ, given as:

$$\Phi = \frac{2C^{\#} + \frac{1}{2}H^{\#}}{O^{\#}} \tag{2.2}$$

where $C^{\#}$, $H^{\#}$, and $O^{\#}$ are the total number of carbon, hydrogen, and oxygen atoms in the mixture. The second is a non-product equivalence ratio φ, given as:

$$\varphi = \frac{2C^{\#}_{-CO_2} + \frac{1}{2}H^{\#}_{-H_2O}}{O^{\#}_{-CO_2-H_2O}} \tag{2.3}$$

where $C^{\#}_{-CO_2}$, $H^{\#}_{-H_2O}$, and $O^{\#}_{-CO_2-H_2O}$ are the number of C, H, and O atoms not including those in the complete combustion products CO_2 and H_2O. For a lean, fully unreacted

fuel-air mixture the two definitions are equivalent. However, if recycled exhaust gases are introduced or as reactions progress, the two equivalence ratios have different values.

Considering the gas at one point in an engine as a small homogeneously mixed control volume, such as a CFD cell, the gas mixture is composed of three sources: atmospheric Air, unburned Fuel, and Recycled Exhaust Gases (EGR) from the previous engine cycle. To simplify the analysis, it is assumed that the EGR consists of complete combustion products (containing only H_2O, CO_2, O_2 and N_2). Within a stratified engine, the equivalence ratio and composition of fresh reactants in a single cell may differ significantly from the equivalence ratio and composition of the recycled products in that cell, as well as from the mean conditions in the cylinder. Grouping the atmospheric air and fuel together results in two gas sources. Each source has a composition given by the stoichiometry for the complete combustion of a hydrocarbon fuel at a given global equivalence ratio (Φ):

$$\text{Fresh} := \Phi_{\text{Fr}} \text{C}_x\text{H}_y + \left(x + \frac{y}{4}\right)(\text{O}_2 + 3.76\text{N}_2) \tag{2.4}$$

$$\begin{aligned}\text{Exhaust} := {} & \Phi_{\text{Ex}} \left(x\text{CO}_2 + \frac{y}{2}\text{H}_2\text{O} + \left(x + \frac{y}{4}\right) 3.76\text{N}_2\right) \\ & + (1 - \Phi_{\text{Ex}}) \left(x + \frac{y}{4}\right)(\text{O}_2 + 3.76\text{N}_2)\end{aligned} \tag{2.5}$$

where Φ_{Fr} and Φ_{Ex} are the global equivalence ratios of the Fresh and Exhaust sources, while x and y are the number of carbon and hydrogen atoms in the fuel.

When the two gas sources, Fresh and Exhaust, are mixed with molar ratio $X_{\text{Fr}}/X_{\text{Ex}}$ such that $X_{\text{Fr}} + X_{\text{Ex}} = 1$, the resulting number of moles for each species may be easily calculated from a linear combination of Equations 2.4 and 2.5. However, given an already mixed gas sample with known species concentrations, it is not possible to 'unmix' the gases and determine the two source equivalence ratios (Φ_{Fr}, Φ_{Ex}) and mixing fraction (X_{Ex}). Fortunately, the exact knowledge of Φ_{Fr}, Φ_{Ex}, and X_{Ex} is not necessary. As seen in Equation 2.5, the Exhaust source may be viewed as the combination of two gas mixtures,

blended with a molar ratio Φ_{Ex}/(1 - Φ_{Ex}). The first mixture consists of stoichiometric combustion products (SCP), while the second mixture is just air. If the excess air from the Exhaust source is lumped with the Fresh gas mixture, then the original gas sample may be viewed as consisting of two different sources: a 'fresh' source with global equivalence ratio Φ equal to the non-product equivalence ratio φ of the entire gas sample; and an 'exhaust' source with global equivalence ratio $\Phi = 1$.

To illustrate this, consider a general fuel-air-EGR mixture consisting of fuel, O_2, N_2, CO_2, and H_2O. Based on the previous discussion, the fuel and O_2 are present only in the 'fresh' source, CO_2 and H_2O are present only in the stoichiometric 'exhaust' source, and N_2 is present in both sources. The mole fraction of N_2 may then be divided into two parts, $X_{N_2,Reac}$ and $X_{N_2,st}$, where the subscript *Reac* refers to the N_2 associated with the molecular O_2, and the subscript *st* refers to the N_2 associated with the O_2 required to produce the CO_2 and H_2O present. From Equations 2.4 and 2.5, the following relations can be derived:

$$1 = X_{C_xH_y} + X_{O_2} + X_{N_2,Reac} + X_{CO_2} + X_{H_2O} + X_{N_2,st} \tag{2.6}$$

$$\frac{X_{H_2O}}{X_{CO_2}} = \frac{y/2}{x} \qquad \frac{X_{N_2,st}}{X_{CO_2}} = \frac{\left(x+\frac{y}{4}\right)3.76}{x} \qquad \frac{X_{N_2,Reac}}{X_{O_2}} = 3.76 \tag{2.7}$$

Using those relations, the mole fraction of stoichiometric combustion products (SCP) present as a diluent is then:

$$\begin{aligned} X_{SCP} &= X_{CO_2} + X_{H_2O} + X_{N_2,st} \\ &= \left[1 + \frac{y}{2x} + \left(x+\frac{y}{4}\right)\frac{3.76}{x}\right] X_{CO_2} \end{aligned} \tag{2.8}$$

For the isooctane fuel used in this study, Equation 2.8 yields $X_{SCP} = 8X_{CO_2}$.

The variables φ and X_{SCP} then completely define a gas mixture. Both variables can be calculated using only knowledge of the local gas composition and fuel stoichiometry. The

mole fractions of fuel and oxygen can be calculated from φ and X_{SCP} by:

$$X_{\mathrm{C}_x\mathrm{H}_y} = \frac{\varphi\,(1 - X_{\mathrm{SCP}})}{\left[\varphi + 4.76\left(x + \frac{y}{4}\right)\right]} \tag{2.9}$$

$$X_{\mathrm{O}_2} = \frac{1 - X_{\mathrm{SCP}}}{\left[\frac{\varphi}{\left(x + \frac{y}{4}\right)} + 4.76\right]} \tag{2.10}$$

In traditional engine applications where the charge is well mixed, it is usually assumed that the equivalence ratios of the Fresh and Exhaust sources are the same. Conditions are then typically reported with a global Φ and an EGR mole fraction (X_{EGR}) or mass fraction, as was used for the simulation initial conditions in Section 2.2. The variables Φ and X_{EGR} can be related to φ and X_{SCP} (via X_{CO_2} and Equation 2.8) using:

$$\varphi = \frac{(1 - X_{\mathrm{EGR}})\Phi}{1 - X_{\mathrm{EGR}}\Phi} \tag{2.11}$$

$$X_{\mathrm{CO}_2} = \frac{X_{\mathrm{EGR}}\Phi x}{X_{\mathrm{EGR}}\Phi\left(\frac{y}{4} - 1\right) + \Phi + 4.76\left(x + \frac{y}{4}\right)} \tag{2.12}$$

2.7 Correlation of Laminar Burning Velocity, Thickness and Burned Gas Temperature

The correlation expressions for laminar burning velocity presented in this work, Equations 2.15-2.17, are based on the correlations of laminar burning velocity for isooctane-air mixtures developed in our previous publication [68]. They follow the general form presented by Göttgens and Müller [110, 111], which is based on an asymptotic analysis of stoichiometric methane flames and has been used to predict burning velocities for multiple fuels over a range of equivalence ratios. The resulting expression includes terms corresponding to the fuel concentration, a characteristic activation temperature for the flame

chemistry (indicated as the inner layer temperature, T^0), and the temperature differences between T_u, T^0 and T_b. The dependence of burning velocity on pressure is accounted for by the inner layer temperature.

The analysis presented in the Section 2.5 highlights the importance of the kinetic influence of O_2 on the burning velocity of EGR dilute flames. As a result, the expression for laminar burning velocity, Equation 2.15, is modified from its previous form to include dependences on both the fuel and O_2 concentrations. Using Equations 2.9 and 2.10 from the previous section, the product of the fuel and O_2 concentrations for arbitrary reaction orders (m and r) is given in terms of φ and $(1-X_{\mathrm{SCP}})$ by:

$$X^m_{\mathrm{C}_x\mathrm{H}_y} X^r_{\mathrm{O}_2} = A\varphi^m \left(1-X_{\mathrm{SCP}}\right)^{(m+r)} \tag{2.13}$$

$$A = \frac{1}{\left[\varphi + 4.76\left(x+\frac{y}{4}\right)\right]^m} \frac{1}{\left[\frac{\varphi}{\left(x+\frac{y}{4}\right)} + 4.76\right]^r} \tag{2.14}$$

where the proportionality term A is approximately constant, varying by less than 5% for φ between 0.0 and 1.0 with the exponents used in the current correlation. We found that the φ and $(1-X_{\mathrm{SCP}})$ terms were the most appropriate for implementation in CFD codes, and were therefore chosen for the correlation expressions. The explicit use of terms for both the fuel and oxygen concentrations is consistent with the findings in Section 2.5, and with existing ignition delay correlations such as He et al. [74]. It is also consistent with the early steps in the derivation of the asymptotic solution for a laminar flame, where the fuel and oxygen concentrations appear in global reaction rate equations [133]. The resulting correlations, with modifications from previous work as indicated, are then given as:

$$S_L = F \underbrace{\varphi^m}_{\text{Modified}} \exp(-G/T^0) \left(\frac{T_u}{T^0}\right) \left(\frac{T_b - T^0}{T_b - T_u}\right)^n \underbrace{(1 - X_{\text{SCP}})^{D_1}}_{\text{New}} \tag{2.15}$$

$$T^0 = \left(\frac{-E}{\ln(p/B)}\right) \left(\underbrace{\varphi(1 - X_{\text{SCP}})}_{\text{Modified}} + C_7\right)^{C_8} + C_9 T_u + \underbrace{a_1 p^{a_2} \left((\varphi(1 - X_{\text{SCP}}))^{a_3} - 1\right)}_{\text{Modified}} \tag{2.16}$$

$$T_b = T_u + \varphi \left(c + d\varphi + e\varphi^2 + f T_u + gp\right) \underbrace{(1 - X_{\text{SCP}})^h}_{\text{New}} \tag{2.17}$$

The expression for the inner layer temperature T^0, Equation 2.16, is slightly modified from the expression given in previous work to be consistent with the new variables in Equation 2.15. Here the previously used fuel mass fraction Y_f is replaced with $\varphi(1 - X_{\text{SCP}})$, which is approximately proportional to the fuel mole fraction $X_{\text{C}_x\text{H}_y}$. We did not observe a T^0 dependence on oxygen concentration or EGR rate, as shown in Figure 2.6, with T^0 evaluated from the HCT simulations as the temperature at the maximum temperature gradient. HCT data are shown as symbols, predictions from Equation 2.16 as lines. The slight under-prediction of T^0 is consistent with prior observations by Göttgens and Müller [110, 111].

After fitting the correlation constants in Equations 2.15-2.17, the simulated burning velocities from HCT can be reproduced with an average error of 3.4% and a standard deviation of 4.3%. The error statistics for these correlation predictions compare favorably to the predictions for purely air diluted cases presented in our previous publication [68]. Best fit parameters for Equations 2.15 and 2.16 are provided in Table 2.4. Considering only conditions expected to be relevant for engine simulations, specifically those with S_L between 20 and 200 cm/sec, the correlation average accuracy improves to 2.4% with a 2.3% standard deviation.

Burned gas temperature (T_b) was fit with Equation 2.17 using T_u, T_b, p, φ and X_{SCP} from the simulation initial conditions. The best fit parameters for Equation 2.17 are included

in Table 2.5; only h was fit to the new data for EGR dilute conditions, other terms were held constant at their values from our previous work. Comparison of the constant pressure adiabatic flame temperatures to the predicted values from Equation 2.17 produced an average error and error standard deviation of 1.5% and 1.1%, respectively.

Reaction front thickness (δ) was determined from the HCT simulations by dividing the difference between $T_{\max}$ and T_u by the maximum temperature gradient within the reaction front, where $\delta = (T_{\max} - T_u) / (dT/dx_{\max})$. Following the approach used in our previous study, originally of Göttgens et al., the reaction front thickness was fit with Equation 2.18, using the preheat zone thickness (l_F) obtained from Equation 2.19 and the ratio of the mixture thermal conductivity to heat capacity (λ/C_p) calculated from Equation 2.20 at T^0 [110]. The fit of the reaction front thickness with Equation 2.18 using predicted T^0, S_L and T_b values taken from Equations 2.15-2.17 resulted in an average error and error standard deviation of 16.9% and 19.3% respectively. For engine relevant conditions with S_L between 20 and 200 cm/sec and pressure between 15 and 60 bar, the accuracy improves to 10.5% and 8.1%, respectively.

$$\delta = c_f \left(\frac{T_b - T_u}{T^0 - T_u} \right) l_F \underbrace{(1 - X_{\mathrm{SCP}})^{c_e}}_{\text{New}} \quad \underbrace{c_f = 0.723}_{Modified} \quad \underbrace{c_e = 0.485}_{New} \tag{2.18}$$

$$l_F = \frac{\left({}^{\lambda}/_{C_p} \right)\big|_{T^0}}{\rho_u S_L} \tag{2.19}$$

$${}^{\lambda}/_{C_p} = 2.58 \times 10^{-5} \left(T/298K \right)^{0.7} \mathrm{kg/m\ s} \tag{2.20}$$

The fitting of laminar burning velocity, reaction front thickness and burned gas temperature was performed using a simplex method, where the objective function was defined as the sum of the magnitude of the percent errors between the steady simulation

results and the correlation predictions. The objective function definition was selected to prevent high speed reaction fronts from dominating the fitness evaluation as well as preventing over and under-predictions from offsetting each other.

2.8 Reaction Front Characteristics with EGR Dilution

Figure 2.7 compares the correlation predictions from Equations 2.15-2.17 to the HCT simulation results at 15 bar pressure and T_u = 900K, where simulations are indicated as points, correlation predictions as lines. There is excellent agreement between the HCT simulation results and the correlation predictions, with qualitatively similar figures obtained at other T_u-p combinations. The results show dilution with EGR suppressing burning velocities across a range of equivalence ratios and EGR rates, consistent with the generally accepted influence of EGR dilution.

Figure 2.8 compares the S_L predictions from Equations 2.15-2.17 to the experimentally developed correlation from Marshall et al. [115], with T_u = 500K, p = 5 bar, and EGR mole fractions x_r = 0.0 - 0.3. Good agreement between the correlations is observed at these conditions, with S_L differing by less than 10% over most of the range presented. The stated limits of the Marshall correlation are $p < 6$ bar, $T_u < 640$K, $\Phi > 0.7$ and $x_r < 0.3$, requiring significant extrapolation to address experimentally observed SACI conditions.

The burning velocity data presented in Figures 2.7(a) and 2.8 display notable shifts in the equivalence ratio of the peak burning velocity as EGR dilution is increased. In Figure 2.7(a), at EGR rates above 40% the peak S_L occurs near Φ = 0.9, not at Φ = 1.1 as is observed for air dilute flames. This result is counterintuitive because it appears that at high EGR rates increasing dilution (via decreasing Φ and Φ') causes a seemingly non-physical increase in the burning velocity. This behavior can be understood by considering the burning velocity in terms of the dilution composition. Figure 2.9 shows contours of constant flame speed from Equations 2.15-2.17 as solid lines, with HCT simulation conditions from Figure 2.7(a) as

symbols, at T_u = 900K and p = 15 bar. Using the traditional Φ-EGR variables, Figure 2.9(a) displays the same counterintuitive behavior as Figure 2.7(a). Here the composition of the EGR is a function of the global Φ, such that decreasing Φ simultaneously decreases the fraction of combustion products (CO_2 and H_2O) while increasing the X_{O_2} present in the EGR. Re-plotting the same conditions using the φ-SCP variables developed in Section 2.6 allows us to separate these effects. In Figure 2.9(b), the φ axis corresponds to dilution with excess O_2, whereas the X_{SCP} axis corresponds to dilution with combustion products; increasing dilution by moving up or to the left always produces a monotonic decrease in S_L, as is intuitively expected. Changes in the EGR composition are evident by the slope of the lines of constant EGR, where at high EGR rates small decreases in Φ produces significant reductions in φ as well as reductions in X_{SCP}. Analyzing the net response of S_L to changes in Φ at high EGR rates is complicated by the competing influences of replacing the non-reacting X_{SCP} diluent with a reactive O_2 diluent, the reduction in diluent heat capacity due to the composition change, and the decrease in charge energy input Φ'. Figure 2.10 re-plots the conditions from Figures 2.7(a) and 2.9 in terms of T_b and X_{O_2}. Considering the 60% EGR cases, shifting from Φ = 1.0 to 0.9 results in a net increase in T_b and an increase in X_{O_2}, both of which contribute to an increase in S_L. When Φ is further reduced to 0.8, the decrease in heat capacity is not sufficient to overcome the reduction in energy input (Φ'), reducing T_b. The accompanying increase in X_{O_2} does not compensate for the decrease in T_b, resulting in the observed decrease in S_L.

2.9 Observations of Reaction Front Characteristics in Multiple Combustion Regimes

Considering the HCCI, SACI, and SI combustion regimes presented in Chapter 1 in Figure 1.1, the area most relevant for this work is near the autoignition boundary, which defines the lowest unburned temperature at which autoignition will occur in the absence of

any significant energy release by other parts of the charge. This line slopes toward lower unburned temperatures at high Φ' as ignition delay times are reduced with increasing fuel concentration. To the right of this line is the HCCI autoignition regime, while to the left are the SI and SACI regions. Laminar flame behavior near this line is of particular interest for SACI operation.

Contours from the laminar burning velocity correlation of the current work are shown on the T_u-T_b diagram at 40 bar in Figure 2.11(a), with the autoignition boundary and Φ' lines for air dilution included from Figure 1.1. Shown are S_L iso-lines of 10, 30, 60, and 100 cm/s and EGR levels of 0, 20, 40 and 60%. At this pressure, the correlation is extrapolated for the 60% EGR level, and for conditions in the lower right portion of the diagram extending past the $\tau_{ID}/\tau_F = 10$ iso-line indicated in Figure 2.12, as steady reaction fronts were not obtained under these conditions. The resulting S_L iso-lines show qualitatively similar behavior with varying EGR level, where iso-lines slope down and to the right. This indicates that for low Φ'-T_b conditions S_L can be maintained through the use of elevated T_u's for all EGR levels. HCT data show consistent behavior but are omitted from the Figure for clarity.

Figure 2.11(b) shows laminar burning velocity contours on the T_u-T_b diagram at 40 bar comparing dilution methods. One set of iso-lines corresponds to isooctane-air mixtures diluted with excess air, while the second set of iso-lines corresponds to stoichiometric isooctane-air mixtures diluted with EGR. The iso-lines for EGR dilution fall to the upper left of the corresponding air dilution iso-lines. This indicates that for a given T_u, EGR dilute mixtures require a higher T_b than air dilute mixtures to achieve a given S_L. Similarly, to maintain a target T_b and S_L, EGR diluted mixtures require higher T_u's than air diluted mixtures. This behavior is consistent with the results discussed in Section 2.5, where EGR dilute mixtures have lower X_{O_2} available for chemical kinetics, corresponding in part to a reduction in S_L compared to air dilute mixtures.

Figure 2.12 shows the ratio of ignition delay, τ_{ID}, to the correlated reaction front time, τ_F, on the T_u-T_b diagram at 40 bar. Here τ_{ID} is calculated from the isooctane ignition

delay correlation of He et al. [74], and the reaction front time $\tau_F = \delta/S_L$ is calculated from Equations 2.15-2.20. The shift in τ_{ID}/τ_F isolines with dilution method indicates that at a given T_u and T_b, an EGR dilute reaction front will travel fewer flame thicknesses than an air dilute front before autoignition occurs in the end-gas, as a result contributing a slightly smaller percentage of the overall heat release in a SACI engine. The difference in these curves is greatest in the lower right portion of the diagram, near the low load autoignition region where steady flames were not observed prior to autoignition. This behavior is consistent with observations that spark assist is less effective under low load conditions, i.e. stability can be improved but phasing is unaffected [54]. Our results suggest that EGR dilution is likely to be less amenable to spark assist at low engine loads than equivalent amounts of air dilution.

2.10 Conclusions

This chapter addresses the need for correlations of pre-mixed isooctane-air-EGR laminar reaction front data under the highly dilute, high preheat temperatures relevant for SACI combustion. HCT was used to produce simulated reaction fronts under conditions relevant for SI, SACI, and HCCI combustion, extending a previous study to include dilution with recirculated exhaust gases (EGR) as used in practical engine applications.

The simulation was exercised over fuel-air equivalence ratios, unburned gas temperatures, pressures and EGR levels ranging from 0.1 to 1.0, 298 to 1000 K, 1 to 250 bar, and 0 to 60% (by mass) respectively. Steady reaction fronts with burning velocities in excess of 5 cm/s could not be established under all of these conditions, especially when burned gas temperatures were below 1450 K or when characteristic reaction front propagation times were on the order of the unburned gas ignition delay. The use of EGR dilution slightly reduced the range of T_u-T_b conditions where steady flames could be produced.

Reaction fronts diluted with EGR were noted to produce lower laminar burning velocities

than air diluted reaction fronts with the same unburned and burned gas temperatures. This behavior was investigated with a scaling study of O_2 concentration on chemical kinetics. The reactions exhibiting the greatest influence on S_L with changing O_2 concentrations were identified as the high temperature chain branching reaction between molecular oxygen and atomic hydrogen and the competing chain terminating reaction between the same species. Decreases in burning velocity between EGR dilute and air dilute cases were attributed mostly to decreases in the O_2 kinetics between the cases.

A method of uniquely identifying an arbitrary fuel-air-EGR mixture was developed to account for charge stratification in advanced combustion engines. Use of a non-product equivalence ratio (φ) and a mole fraction of stoichiometric combustion products (X_{SCP}) replaces the traditionally used global equivalence ratio (Φ) and EGR fraction. The new formulation given here is particularly applicable to CFD modeling.

Correlations for laminar burning velocity, burned gas temperature, and flame thickness were developed based on the simulation data. They extend the authors' previous correlations for the same properties, and provide excellent agreement with the HCT simulation results; reproducing the burning velocity, thickness, and flame temperature to an average error of 3.4%, 17%, and 1.5%, respectively.

Table 2.1 Range of conditions for existing high pressure laminar burning velocity studies.

Authors	Φ	Pressure	T_u [K]	EGR Surrogate
Ryan and Lestz [108]	0.7 - 1.3	4 - 18 [atm]	470 - 600	15/85% CO_2/N_2
Metghalchi and Keck [94]	0.8 - 1.5	0.4 - 50 [atm]	298 - 700	15/85% CO_2/N_2
Rhodes and Keck [112]	0.7 - 1.2	1 - 8 [bar]	350 - 500	20/80% CO_2/N_2
Bradley et al. [109]	0.7 - 1.0	1 - 10 [atm]	358 - 450	N/A
Jerzembeck et al. [107]	0.7 - 1.2	10 - 25 [bar]	373	Reduced O_2
Göttgens et al. [110]	0.3 - 1.0	1 - 40 [bar]	298 - 800	N/A
Müller et al. [111]	0.6 - 1.0	1 - 40 [bar]	298 - 800	N/A
Martz et al. [68]	0.1 - 1.0	1 - 250 [bar]	298 - 1000	N/A
Marshall et al. [115]	0.7 - 1.3	0.6 - 6 [bar]	340 - 640	Residual Gas

Table 2.2 Range of conditions for laminar reaction fronts simulated in the current work.

Φ	0.1	0.2	0.3	0.4	0.5	0.6	0.7	0.8	0.9	1.0	
T_u [K]	298*	400	600	800	900	950	1000				
Pressure [bar]	1	2.5	5	10	15	25	40	60	100	160	250
EGR [Mass %]	0	20	40	60							

*0% EGR Only

Table 2.3 Reaction front conditions studied for oxygen sensitivity.

	Φ	EGR	Φ'	T_b	S_L	δ	X_{Fuel}	X_{O_2}	X_{O_2}	$C_{p,u}$
	-	Mass %	-	K	cm/s	cm	-	Unburned	Burned	ergs/g-K
Air Dilute	0.4	0	0.40	1864	27.86	3.47E-3	6.68E-3	0.209	0.122	1.21E+7
EGR Dilute	0.7	40	0.42	1858	23.19	4.13E-3	6.86E-3	0.147	0.060	1.25E+7
EGR/Air	-	-	1.05	0.997	0.83	1.19	1.03	0.71	0.49	1.03

Table 2.4 Best Fit Parameters for the laminar burning velocity, Equations 2.15-2.16.

F [cm/s]	m	G [K]	n	D_1	E [K]	B [bar]
232.0763	2.1786	-2585.6	5.1749	3.019	23,127	1.12E+11
C_7	C_8	C_9	a_1	a_2	a_3	
0.3256	0.4231	0.2784	15.2358	0.1	-1.1	

Table 2.5 Best Fit Parameters for the adiabatic flame temperature, Equation 2.17.

c	d	e	f	g	h
2638.1	194.6	-773.045	-0.34968	0.3432	0.857

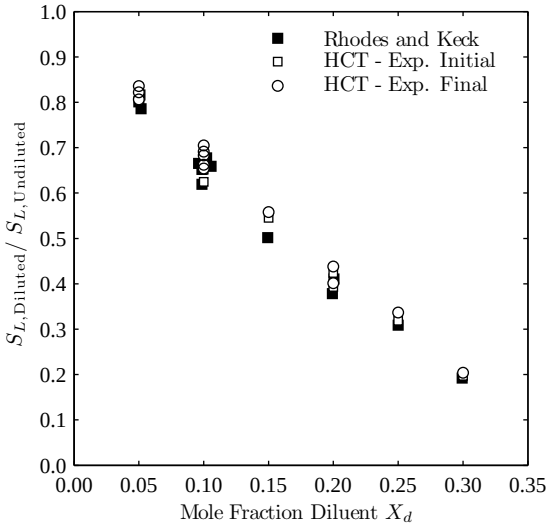

Figure 2.1 Fuel-air-diluent laminar burning velocity ratio, $S_{L,\mathrm{Diluted}}/S_{L,\mathrm{Undiluted}}$, as a function of the molar dilution level X_d. Dilution consists of simulated EGR with 20/80% CO_2/N_2 by volume. Experimental data from the indolene studies of Rhodes and Keck [112] shown as closed symbols, HCT isooctane simulation results shown as open symbols. Transient experimental data cover equivalence ratios between 0.7 and 1.2, T_u from 350K to 500K, and p from 1 to 8 atm. HCT simulations conducted at the experimental initial and final conditions.

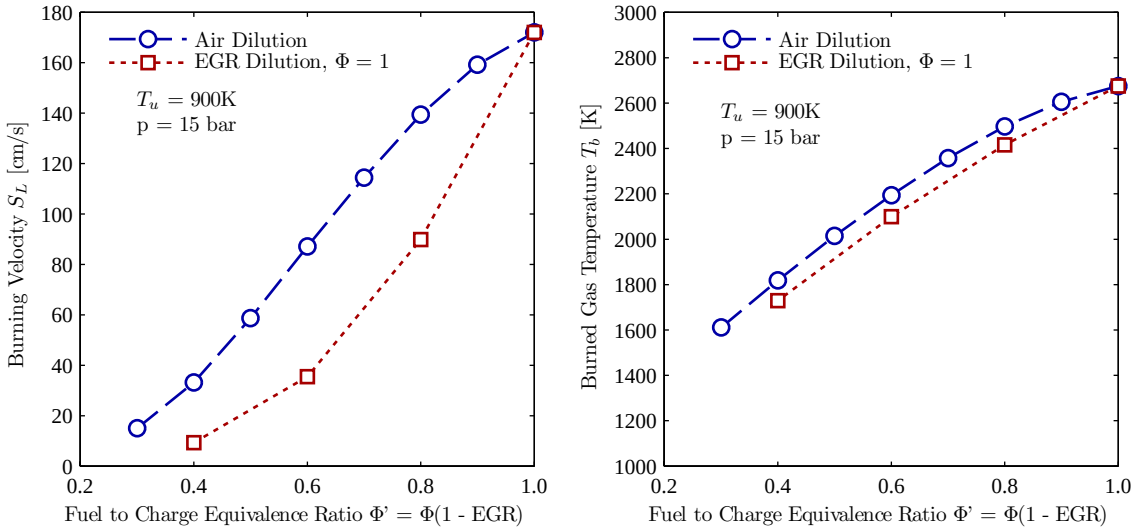

(a) Flame Speed

(b) Flame Temperature

Figure 2.2 Laminar burning velocity as a function of overall dilution Φ', at T_u = 900K, 15 bar, Figure 2.2(a). Conditions diluted with air exhibit higher burning velocities than those diluted with EGR. Corresponding burned gas temperatures are shown in 2.2(b), where small decreases in burned gas temperature are observed with EGR dilution, consistent with increases in the mixture heat capacity. Simulation results from HCT shown as symbols, lines connect points and do not imply additional data.

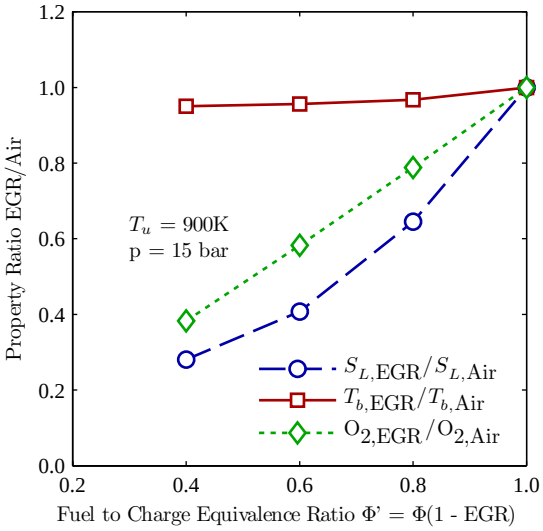

Figure 2.3 Ratios of reaction front properties for different dilution methods, EGR dilute value / Air dilute value. Data re-plotted from Figure 2.2 for reaction fronts at T_u = 900K, p = 15 bar. The similarity between the S_L and the reactant O_2 curves suggests that the decrease in S_L is related to the mixture O_2 concentration as well as T_b.

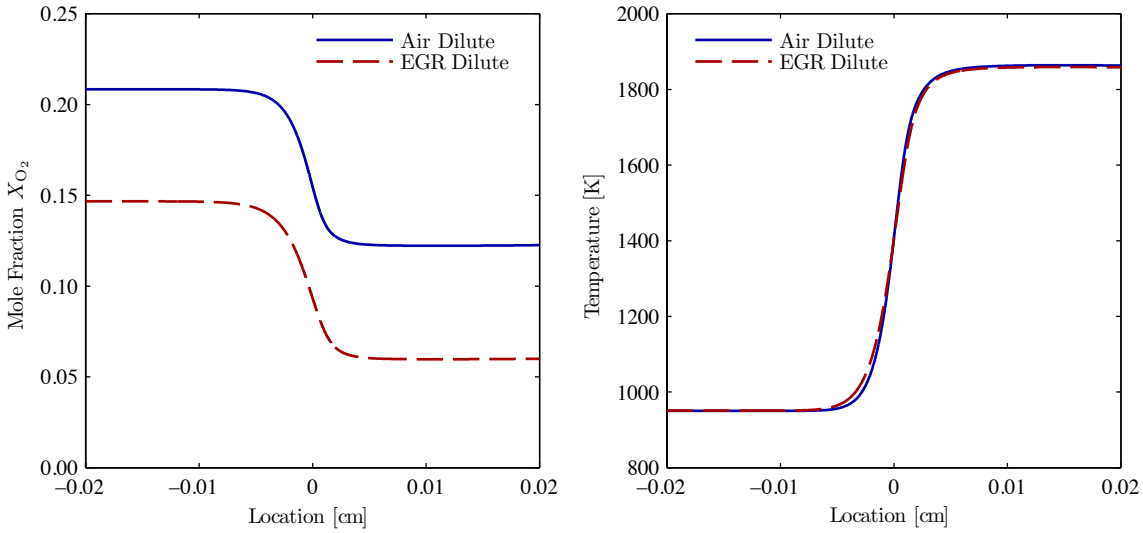

(a) Oxygen

(b) Temperature

Figure 2.4 Oxygen and Temperature profiles for an Air dilute reaction front with Φ = 0.4 and and EGR dilute reaction front with Φ = 0.7 and 40% EGR, both at T_u = 950K and 40 bar, detailed in Table 2.3. The temperature profiles for the two fronts are very similar, whereas the O_2 concentration varies significantly between the two cases. Here the S_L of the EGR dilute case is 17% less than the S_L of the air dilute case (23.2 cm/s vs. 28.9 cm/s), suggesting that the O_2 concentration has a strong influence on S_L. Profiles are location shifted such that the location of the average temperature between $T_{\max}$ and T_u occurs at X = 0 cm.

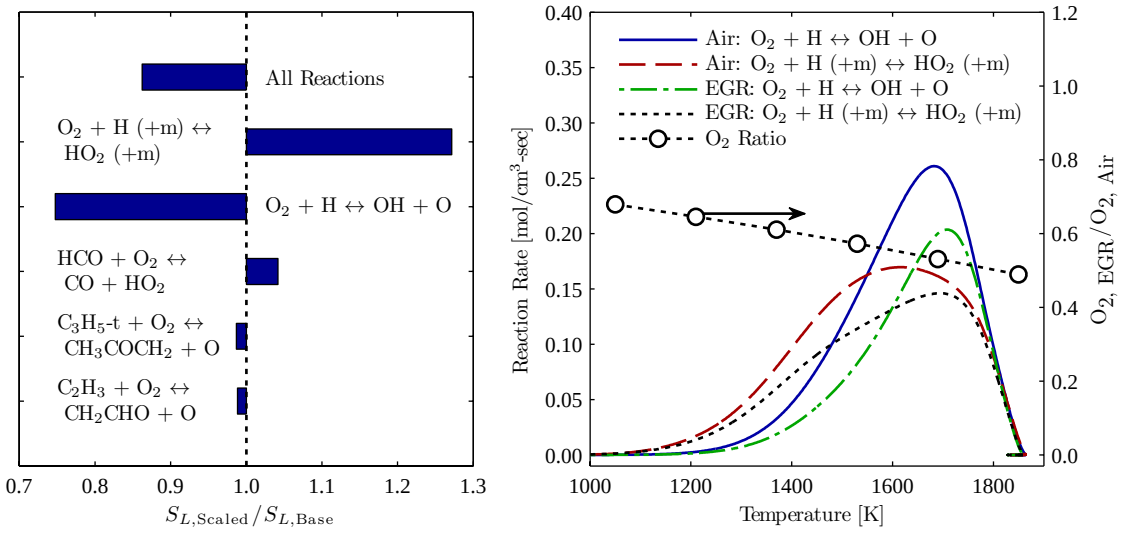

(a) Sensitivity (b) Reaction Rate

Figure 2.5 Response of laminar burning velocity S_L to a 50% decrease in O_2 concentration in kinetics, 2.5(a). S_L is most sensitive to the high temperature chain branching and chain terminating reactions, other reactions with very low sensitivities are not shown. Reaction rates for high temperature chain branching and chain terminating reactions for unmodified air dilute and EGR dilute flames from Table 2.3 vs. temperature, 2.5(b). The ratio of O_2 concentration between cases in the reaction zone is approximately 0.5, consistent with the 50% scaling in 2.5(a).

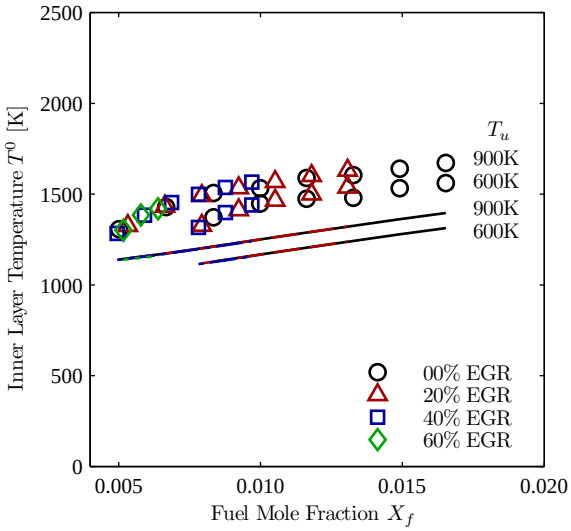

Figure 2.6 Inner layer temperature T^0 as a function of fuel mole fraction X_f at EGR dilution from 0% to 60%, T_u = 600 and 900K, pressure = 15 bar. HCT T^0 data evaluated at the maximum temperature gradient, shown as symbols, correlation values from Equation 2.16 as lines. EGR dilution effects collapse to a X_f dependence. The slight under-prediction of T^0 is consistent with the observations of Göttgens and Müller [110, 111].

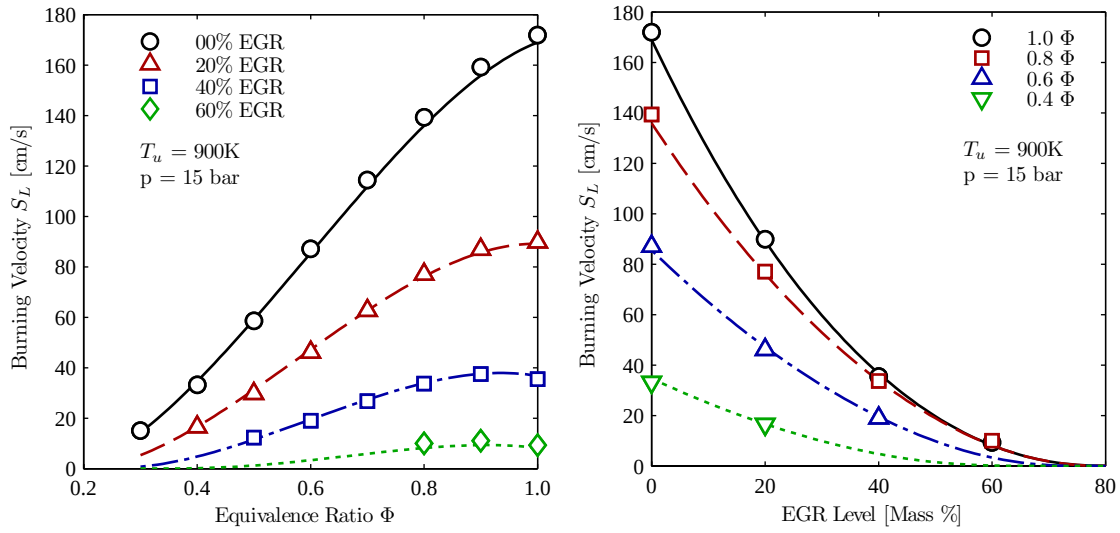

Figure 2.7 Isooctane-air-EGR laminar burning velocity at T_u = 900K, p = 15 bar, as a function of Equivalence Ratio Φ 2.7(a), and as a function of EGR dilution 2.7(b). Laminar burning velocity simulation results from HCT shown as symbols, correlation predictions from Equations 2.15-2.17 as lines.

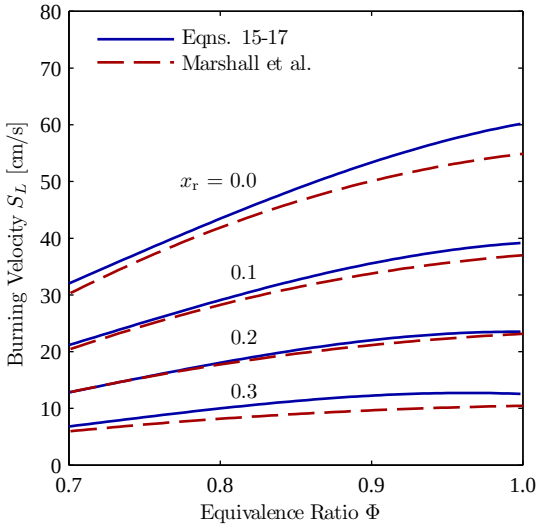

Figure 2.8 Laminar burning velocity correlations from Equations 2.15-2.17 of the current work (solid lines) and from Marshall et al. [115] (dashed lines) as a function of Φ and EGR mole fraction x_r. Conditions are as reported by Marshall, T_u = 500K and p = 5 bar. Good agreement between the correlations is observed for these conditions, with S_L differing by less than 10% over most of the range presented.

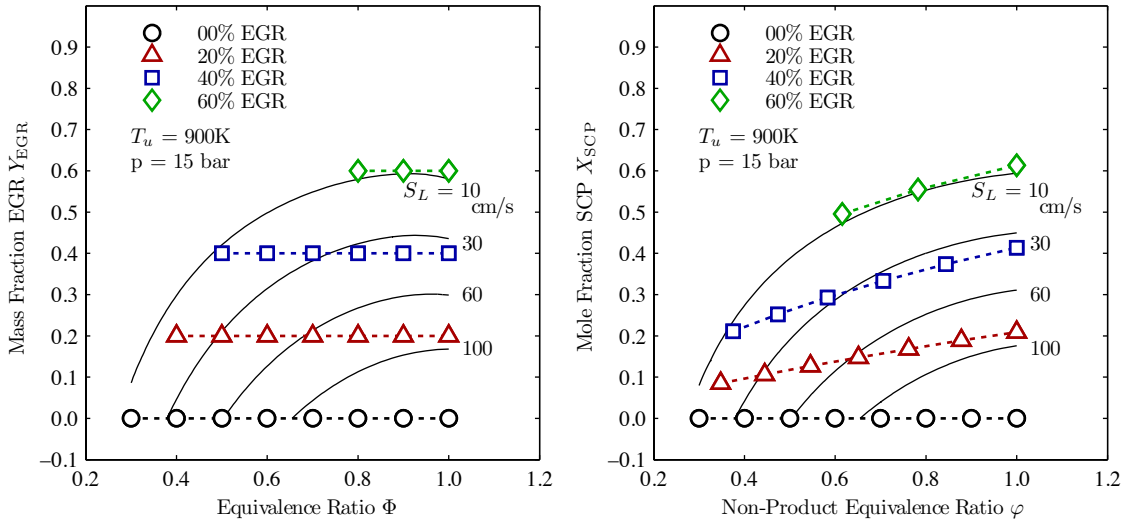

(a) Traditional Φ-EGR Space

(b) New φ-SCP Space

Figure 2.9 Flamespeed iso-lines and HCT simulation conditions in dilution space for T_u = 900K, p = 15 bar. Solid lines from Equations 2.15-2.17, simulation conditions indicated by symbols. In traditional Φ-EGR space 2.9(a), at high levels of EGR the burning velocity peaks near Φ = 0.9. The same data plotted in φ-SCP space 2.9(b) shows the expected behavior where increasing dilution decreases burning velocity.

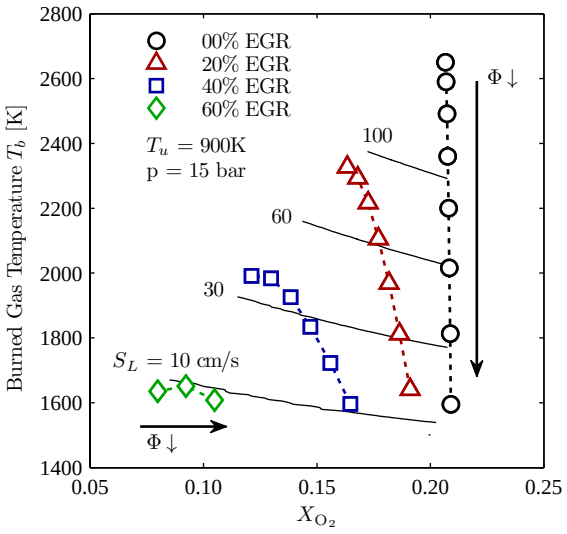

Figure 2.10 Flamespeed iso-lines and HCT simulation conditions in terms of the major influences on S_L, T_b and X_{O_2}, for T_u = 900K, p = 15 bar. Solid lines from Equations 2.15-2.17, simulation conditions indicated by symbols. The behavior of peak T_b corresponds well to the behavior of peak S_L in Figure 2.7(a).

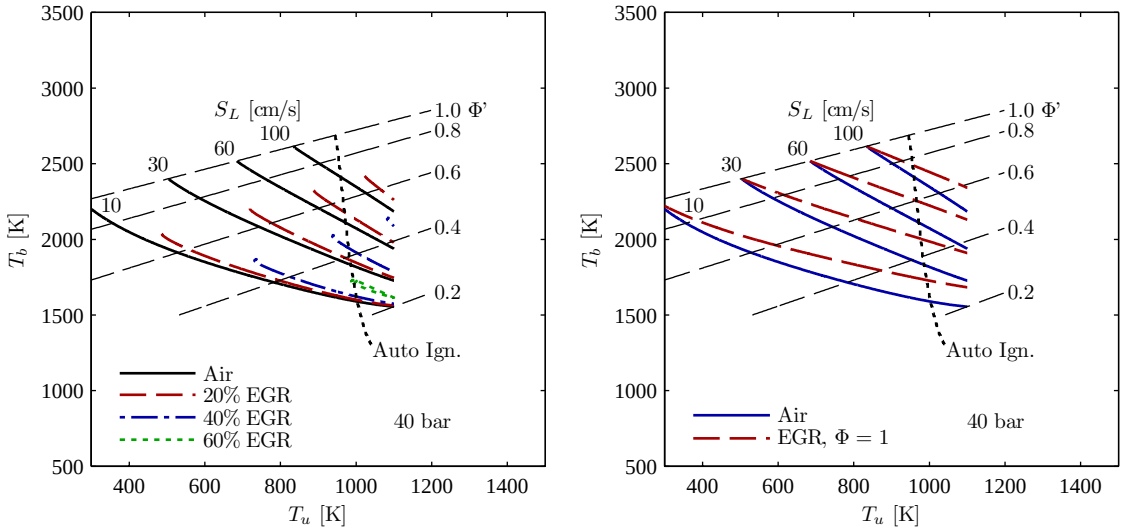

(a) EGR Level (b) Dilution Method

Figure 2.11 Laminar burning velocity contours from Equations 2.15-2.17 in the T_u-T_b domain at 40 bar. Auto ignition boundary reproduced from Figure 1.1 using the ignition delay correlation of He et al. [74]. Results plotted by EGR rate, 2.11(a), show qualitatively similar behavior for all EGR rates. Results plotted by dilution method, 2.11(b), show lower S_L at constant T_u-T_b for EGR dilute conditions when compared to air dilute conditions.

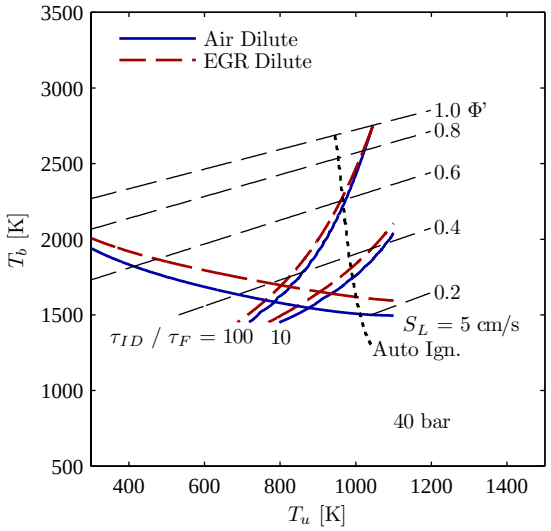

Figure 2.12 The ratio of ignition delay τ_{ID} from the correlation of He et al. [74] to correlated reaction front time, τ_F, with S_L from Equations 2.15-2.17 and δ from Equation 2.18 in the T_u-T_b domain at 40 bar. The region where steady flames with $S_L > 5$ cm/s and $\tau_{ID}/\tau_f > 10$ can be generated is smaller for purely EGR dilute conditions than for purely air dilute conditions. Limits for conditions diluted with a mixture of EGR and excess air fall between those indicated on the Figure.

Chapter 3
KIVA-CFMZ Model for Open Cycle Simulations

3.1 Modeling SACI Combustion in KIVA-3v

The SACI combustion model used in this work was implemented in the 3D CFD code KIVA-3v [134]. This framework was chosen for KIVA-3v's ability to spatially resolve the combustion chamber, intake, and exhaust manifolds, while accounting for moving valves and direct fuel injection, as well as the resulting thermal and compositional stratification in the combustion chamber. The current work adopts a SACI model recently developed at the University of Michigan, the Coherent Flamelet MultiZone model (KIVA-CFMZ) of Martz [70, 101], where an extensive model derivation is provided in the original work [70]. This model combines the Coherent Flamelet model [88,98,135,136] for treatment of reaction fronts with the fully coupled Multi-Zone chemistry model of Babajimopoulous [99, 132] for treatment of detailed chemical kinetics.

The dimensions of the computational cells typically used by KIVA-3v are too large to directly resolve turbulent reaction fronts. To overcome this limitation a sub-grid model is required to predict the contributions of the reaction front and chemically controlled auto-ignition to the combustion process in each cell. The KIVA-CFMZ model uses a generalized sub-grid model appropriate for modeling SI, SACI, and HCCI combustion. Each computational cell is divided into a maximum of three zones, shown conceptually in Figure 3.1, in a formulation that is physically consistent with optical images of SACI and HCCI combustion [61–63]. The zones in the model are:

- A Reactant Zone (u) upstream of the Reaction Front, accounting for heat release due to auto-ignition, treated as a homogeneous reactor. Also referred to as the 'unburned' zone or end-gas.

- A turbulent Reaction Front separating the Reactant and Product Zones, treated as a flamelet.

- A Product Zone (b) downstream of the reaction front, accounting for chemistry in the burned gasses produced by the Reaction Front, treated as a homogeneous reactor. Also referred to as the 'burned' zone or burned-gas.

The total mass in the computational cell is split into reactant and product zone masses, while the reaction front is treated as infinitely thin and contains negligible mass relative to the cell. The zone masses for species m are then related by:

$$m_m = m_{m,u} + m_{m,b} \tag{3.1}$$

Where the overall cell mass (m_m) and the reactant zone mass ($m_{m,u}$) are directly modeled by the solution of transport equations given in Section 3.1.1, while the product zone mass ($m_{m,b}$) is calculated from continuity. As the reaction front moves through a cell over a timestep it consumes mass from the reactant zone and deposits an equal mass of differing species composition in the product zone.

3.1.1 Governing Equations

Combustion in KIVA-3v is modeled through source terms in the species density and internal energy transport equations, Equations 3.2 and 3.3 respectively. The change in composition due to chemistry is captured by the $\dot{\rho}_m^C$ term in Equation 3.2, while the energy released during the combustion process is captured by the $\dot{Q}^C$ term in Equation 3.3.

$$\frac{\partial \rho Y_m}{\partial t} + \frac{\partial \rho u_k Y_m}{\partial x_k} = \frac{\partial}{\partial x_k}\left(\frac{\mu_t}{\sigma_m}\frac{\partial Y_m}{\partial x_k}\right) + \dot{\rho}_m^C + \dot{\rho}_m^S \tag{3.2}$$

In Equation 3.2, ρ is the mean density, Y_m is the mass fraction of species m, u_k is the cell velocity in direction k, μ_t is the dynamic turbulent viscosity and σ_m is the turbulent Schmidt number (set equal to 1.0 here). The addition of fuel to the gas phase due to fuel droplet vaporization is captured by the $\dot{\rho}_m^S$ source term.

$$\frac{\partial \rho I}{\partial t} + \frac{\partial \rho u_k I}{\partial x_k} = -p\frac{\partial u_k}{\partial x_k} + \frac{\partial}{\partial x_k}\left(\lambda \frac{\partial T}{\partial x_k}\right) + \frac{\partial}{\partial x_k}\left[\frac{\mu_t}{\sigma}\sum_{m=1}^{nsp} h_m \frac{\partial Y_m}{\partial x_k}\right] + \rho\varepsilon + \dot{Q}^C + \dot{Q}^W + \dot{Q}^S \tag{3.3}$$

In Equation 3.3, I is the specific internal energy, p is the gas pressure, λ is the mixture thermal conductivity, T is the mixture temperature, h_m is the specific enthalpy of specifies m, summed over all species in the chemical mechanism from m = 1 to nsp, while ε is the turbulent kinetic energy dissipation rate. External heat transfer to the solid walls is included as $\dot{Q}^W$, calculated using the Law of the Wall. Heat transfer between the gas phase and fuel droplets in the domain is accounted for with the $\dot{Q}^S$ source term.

The composition of the Reactant Zone is determined through the solution of an additional set of transport equations for the Reactant Zone species densities, Equation 3.4, while the temperature of the Reactant Zone is determined by solving for the sensible enthalpy of the zone, Equation 3.5. Both equations have been previously used by Baritaud et al. [88] for modeling SI combustion with a non-reacting end-gas, as well as by Martz for modeling SACI combustion with a reactive end-gas [70].

$$\frac{\partial \rho Y_{m,u}}{\partial t} + \frac{\partial \rho u_k Y_{m,u}}{\partial x_k} = \frac{\partial}{\partial x_k}\left(\frac{\mu_t}{\sigma_m}\frac{\partial Y_{m,u}}{\partial x_k}\right) + \dot{\rho}_{m,r}^C + \dot{\rho}_m^S \tag{3.4}$$

$$\frac{\partial \rho h_u}{\partial t} + \frac{\partial \rho u_k h_u}{\partial x_k} = \frac{\partial}{\partial x_k}\left(\frac{\mu_t}{Pr}\frac{\partial h_u}{\partial x_k}\right) + \rho\varepsilon + \frac{\rho}{\rho_u}\frac{\partial p}{\partial t} + \dot{Q}_{w,u} + \dot{Q}_{u,AI}^C + \dot{Q}_u^S \tag{3.5}$$

In Equation 3.4, $\dot{\rho}_{m,r}^C$ is the source term for species change due to chemical reactions. The mass fractions are defined using the mass of species m in the reactant zone, $m_{m,u}$, relative to

the total mass of the computational cell, m_{cell}, as:

$$Y_{m,u} = \frac{m_{m,u}}{m_{\text{cell}}} \tag{3.6}$$

It is also convenient for later calculations to define species mass fractions relative to the zone mass for both the Reactant (u) and Product (b) zones for zone z, given as:

$$Y_m^z = \frac{m_{m,z}}{m_z} \tag{3.7}$$

In Equation 3.5, $\dot{Q}^C_{u,AI}$ is the source term for auto-ignition in the Reactant zone, while the $\dot{Q}_{w,u}$ term accounts for external heat losses in the boundary cells, calculated from the Law of the Wall using the Reactant Zone state. Fuel droplet vaporization is included through the $\dot{Q}^S_u$ enthalpy source term. The turbulent Prandtl number (Pr) is set to 1.0, while the density of the Reactant zone, ρ_u, is defined relative to the Reactant zone mass and volume. It is assumed that the pressure and the specific turbulent kinetic energy dissipation rate (ε) are uniform between the Reactant Zone and the computational cell.

The Reactant Zone specific enthalpy, h_u, is calculated assuming that the Reactant zone is a mixture of ideal gases, with the enthalpies of each species determined from the Reactant zone temperature:

$$h_u = \frac{H_u}{m_u} = \sum_i Y_i^u h_{i,u} \tag{3.8}$$

The development and propagation of the reaction front through the combustion chamber is tracked through the solution of another transport equation for the flame surface density, Σ, the flame surface are per computational cell volume. The equation is similar to that of Baritaud et al. [88] and Martz [70], given as:

$$\frac{\partial \rho \Sigma}{\partial t} + \frac{\partial \rho u_k \Sigma}{\partial x_k} = \frac{\partial}{\partial x_k}\left(\frac{\nu_t}{\sigma_\Sigma}\frac{\partial \rho \Sigma}{\partial x_k}\right) + \rho\left(S_1 + S_2\right)\Sigma - \rho D \tag{3.9}$$

Where the source terms S_1, S_2 and sink term D are described in detail in Section 3.2.1. An

additional source term, S_3, was previously used in the KIVA-CFMZ model to account for spark ignition [70]; it is replaced with a more detailed spark ignition model described in Section 3.4.

3.1.2 Modeling EGR Dilution

An additional transport equation was added to the KIVA-CFMZ model to account for non-uniform EGR dilution throughout the domain, Equation 3.10. While the composition of a cell determined by Equations 3.2 and 3.4 is sufficient to calculate homogeneous chemistry using the MultiZone approach, it is insufficient to determine the reaction progress of the entire cell or of the Reactant zone. A typical approach to calculate reaction progress is to use the stoichiometry of a cell to re-construct the 'cold' reactant gases composed of unburned fuel and air as well as the complete equilibrium products, then to compare the enthalpy of formation of the current cell composition to the enthalpy of formation of those inferred mixtures [70]. For a cell containing EGR dilution such an approach will treat the EGR species (CO_2, H_2O) as combustion products and calculate a non-zero reaction progress, while a more convenient definition would include EGR in the reactants and calculate a zero reaction progress at intake valve closing. To accomplish this a transport equation is solved for the CO_2 present in the EGR dilution:

$$\frac{\partial \rho Y_{CO_2,EGR}}{\partial t} + \frac{\partial \rho u_k Y_{CO_2,EGR}}{\partial x_k} = \frac{\partial}{\partial x_k}\left(\frac{\mu_t}{\sigma_{CO_2}}\frac{\partial Y_{CO_2,EGR}}{\partial x_k}\right) \tag{3.10}$$

Where there are no terms for production or destruction of this EGR tracer CO_2 species, it does not participate in chemical reactions, and is not counted toward the cell or zone masses. Assuming that the H_2O and N_2 associated with EGR are transported along with the CO_2, the compositional relations developed in Section 2.6 can then be used to determine the initial mixture composition including EGR.

3.1.3 Solution Procedure

Equations 3.2, 3.3, 3.4, 3.5, 3.9, and 3.10 are integrated using the standard KIVA-3v method, where the equations are discretized with respect to time and space and the contribution of each physical process to the scalar evolution is determined through operator splitting. In Phase A, the source terms for $\dot{\rho}$ and $\dot{Q}$ are calculated and applied. In Phase B, the effect of species mass and energy diffusion is calculated. Finally, in Phase C the advection terms are calculated and the mixture state updated prior to adjusting the mesh and valve positions to account for movement of the piston and valves at the end of the timestep. A flow chart detailing the order of the major calculations related to combustion is presented in Figure 3.2, along with the sections discussing each process.

As indicated in Figure 3.2, the contribution of fuel vaporization is calculated prior to any of the combustion calculations. Before the spark ignition timing the model skips directly to Reactant zone chemistry solved using the Multi-Zone approach, replicating the behavior expected of an HCCI simulation. In each time step after the spark ignition timing, the model first updates the Product zone composition in all applicable cells, then checks to determine if the spark ignition model is active and either calls the spark sub-model or the coherent flamelet model before updating the Reactant zone with detailed chemical kinetics through the Multi-Zone approach.

3.2 Chemistry Calculations

The contributions of each sub-grid zone to the overall combustion processes are handled in separate steps for each physical process. As indicated in Figure 3.2, first the contribution of the Product zone chemistry is calculated, then the propagation of the reaction front, finally followed by end-gas chemistry in the Reactant zone. The source term for the change in

density of species m in Equation 3.2 is then decomposed by process as:

$$\dot{\rho}_m^C = \dot{\rho}_{m,u}^C + \dot{\rho}_{m,\mathrm{RF}}^C + \dot{\rho}_{m,b}^C \tag{3.11}$$

With a similar decomposition applied to Equation 3.4 for the Reactant zone composition as:

$$\dot{\rho}_{m,r}^C = \dot{\rho}_{m,u}^C + \dot{\rho}_{m,u,\mathrm{RF}}^C \tag{3.12}$$

The change in internal energy due to combustion in Equation 3.3 is given by:

$$\dot{Q}^C = \dot{Q}_u^C + \dot{Q}_{\mathrm{RF}}^C + \dot{Q}_b^C \tag{3.13}$$

While there is only one direct contribution to the reactant zone enthalpy, $\dot{Q}_{u,\mathrm{AI}}^C$, and no decomposition is required.

Calculation of the terms for the reaction front contribution, $\dot{\rho}_{m,\mathrm{RF}}^C$, $\dot{Q}_{\mathrm{RF}}^C$, and $\dot{\rho}_{m,u,\mathrm{RF}}^C$, is discussed in detail in Section 3.2.1. The contributions of end- and burned-gas chemistry, $\dot{\rho}_{m,u}^C$, $\rho_{m,b}^C$, $\dot{Q}_u^C$, and $\dot{Q}_{u,\mathrm{AI}}^C$, are discussed in detail in Section 3.2.2.

3.2.1 Reaction Front Modeling

Following the original development of the KIVA-CFMZ model [70], the propagation of the reaction front through the combustion chamber in this work is described by the Coherent Flamelet model [88,98,135,136]. This model was chosen by Martz for its physical treatment of flame wrinkling during the SACI combustion process [70]. The mass burning rate due to flame propagation in each cell is obtained using the previously mentioned flame surface density transport equation:

$$\frac{\partial \rho \Sigma}{\partial t} + \frac{\partial \rho u_k \Sigma}{\partial x_k} = \frac{\partial}{\partial x_k}\left(\frac{\nu_t}{\sigma_\Sigma}\frac{\partial \rho \Sigma}{\partial x_k}\right) + \rho(S_1 + S_2)\Sigma - \rho D \tag{3.9 revisited}$$

Where the source term S_1 accounts for flame stretch induced by the mean flow field, S_2 accounts for aerodynamic straining of the reaction front by turbulent eddies, while the sink term D accounts for destruction of flame surface area by complete reactant consumption and merging of adjacent flame fronts [137, 138]. Consistent with previous engine simulations S_1 is neglected here [70, 88, 98, 136, 139], while S_2 is provided by the phenomenological Intermittent Turbulence Net Flame Stretch (ITNFS) model of Meneveau and Poinsot [135] (also referred to as the CFM2 model [70, 137]).

The original derivation of the ITNFS model utilized two-dimensional direct simulation of a laminar flames interacting with vortex pairs to study the turbulent wrinkling of a flamelet [135]. Increases in the predicted heat release rate in the control volume were attributed to an increase in the flame front surface area due aerodynamic straining as the vortices interacted with the flame and were used to calculate a resulting flame stretch rate. Interactions over a range of turbulent eddy sizes and eddy-flame interaction frequencies expected in a turbulent flow field were integrated to determine the average hydrodynamic flame stretch ($\langle K \rangle$) as a function of the flow field parameters.

The source term S_2 is calculated using the approach of Meneveau and Poinsot [135]:

$$S_2 = \alpha_0 \Gamma_{\bar{K}} \frac{\varepsilon}{k} \tag{3.14}$$

Where ε is the turbulent dissipation rate, k is the turbulent kinetic energy, and α_0 is a model constant. The non-dimensionalized net flame stretch $\Gamma_{\bar{K}}$ is provided by the ITNFS model:

$$\Gamma_{\bar{K}} = \frac{\bar{K}}{\varepsilon/k} = \frac{\langle K \rangle}{\varepsilon/k} - \frac{3}{2}\left(\frac{L}{\delta}\right)\left(\frac{S_L}{u'}\right)\ln\left(\frac{1}{1-P_q}\right) \tag{3.15}$$

Where a full derivation of Equation 3.15 is presented by Duclos et al. [139]. The RMS turbulent velocity, u', and integral length scale L are calculated from the k–epsilon turbulence model selected in KIVA (standard or RNG), while the laminar flame speed, S_L, and the laminar flame thickness, δ, are calculated using the correlations previously presented in

Section 2.7. Equation 3.15 accounts for both aerodynamic strain promoting flame surface area growth as well as flame quenching offsetting that growth, by the first and second terms on the R.H.S. respectively.

Consistent with previous studies, the CFM-2a model was adopted in this work for the flame surface density destruction term [70, 98]:

$$D = \beta_0 \frac{S_L + Ck^{1/2}}{1 - \bar{c}_2} \Sigma_2 \tag{3.16}$$

Where β_0 and C are model constants, and the reaction progress, $\bar{c}_2$, is given by:

$$\bar{c}_2 = \left(\frac{h^0 - h_R^0}{h_p^0 - h_R^0} \right) \tag{3.17}$$

Where h^0 is the enthalpy of formation of the computational cell, h_p^0 is the enthalpy of formation of the major product species obtained from the cell stoichiometry, and h_R^0 is the enthalpy of formation of the reactant species while accounting for EGR dilution using the cell stoichiometry as well as the EGR tracer species described in Section 3.1.2.

Neither the source or destruction terms, S_2 and D, in Equation 3.9 are calculated prior to completion of the spark ignition model, consistent with previous studies [70, 98]. The details of the spark ignition model and the transition to the full turbulent flame model are described in detail in Section 3.4.

Interaction between the turbulent flame front and the solid walls of the combustion chamber is treated with the Flame Interacting with Surface and Turbulence (FIST) approach of Poinsot et al. [140]. The FIST model used a turbulent two dimensional direct simulation to study the effects of the flame-wall distance on the flame structure and was developed to correct for elevated non-physical flame surface densities near the walls predicted by the Coherent Flamelet model. The model accounts for flame quenching due to heat losses to the combustion chamber walls and for flame laminarization as the turbulent flame approaches the wall. A detailed description of the FIST model modifications to Σ is provided by Martz

in the original KIVA-CFMZ model derivation [70].

When the reaction front model is called in a given timestep, the reaction front propagates across each cell with non-zero flame surface density. Mass is consumed from the reactant zone and placed in the product zone, with the burned gas composition and temperature determined by constant pressure equilibrium calculations. The change in mass is then given by:

$$\dot{m}_b = -\dot{m}_u = \rho_u S_L \Sigma V \tag{3.18}$$

Where V is the cell volume and S_L is calculated from the correlations previously presented in Section 2.7.

The source term in Equation 3.11 for production/destruction of species m in the cell due to reaction front propagation is:

$$\dot{\rho}^C_{m,\mathrm{RF}} = \rho_u \left(Y^{\mathrm{EQ}}_m - Y^u_m\right) S_L \Sigma \tag{3.19}$$

Where the mass fraction Y^{EQ}_m composition generated by the flame is assumed to be constant pressure equilibrium products determined from the state of the reactant zone.

The source term in Equation 3.12 for the reactant zone species density of species m is:

$$\dot{\rho}^C_{m,u,\mathrm{RF}} = -\rho_u Y^u_m S_L \Sigma \tag{3.20}$$

Where there is no production of species in the reactant zone due to flame propagation.

The change in specific internal energy of the cell due to heat release as the reaction front consumes mass in Equation 3.13 is:

$$\dot{Q}^C_{\mathrm{RF}} = -\rho \frac{\left(\sum_m Y_m u^0_m\right)^{\mathrm{RF},e} - \left(\sum_m Y_m u^0_m\right)^{\mathrm{RF},i}}{\Delta t} \tag{3.21}$$

Where the superscript RF, e indicates the provisionally updated cell composition after the reaction front propagation has been calculated, RF, i indicates the composition prior to the

species update, and u_m^0 is the internal energy of formation of species m.

To improve the computational stability of the model, a small mass of each Reactant zone species is retained in each computational cell by preventing complete consumption of the Reactant zone by the reaction front. The timesteps used in Equations 3.19 and 3.20 are adjusted such that the reaction progress due to reaction front propagation does not exceed 0.999, defined as:

$$\bar{c}_1 = \left(1 - \frac{m_u}{m_{\text{cell}}}\right) \tag{3.22}$$

3.2.2 Multi-Zone Model for the Reactant and Product Zones

In the KIVA-CFMZ model, chemical kinetics calculations in the Reactant and Product zones are conducted using the fully coupled Multi-Zone approach of Babajimopoulos [99, 132]. This approach groups the tens of thousands of KIVA computational cells in an engine simulation into a smaller number of chemistry zones with similar thermodynamic states. By grouping cells in this way the computational cost of detailed chemistry can be reduced by an order of magnitude or more relative to calculating a chemical kinetic update in every cell, addressing one of the most computationally expensive steps of a KIVA simulation [141]. The chemistry zones discussed here exist only within the Multi-Zone chemistry subroutine and are different from the Product and Reactant zones defined in the sub-grid model.

Each chemistry zone is treated as a constant volume homogeneous reactor initialized with state information from the source KIVA cells composing the zone. Kinetic calculations are then performed for each reactor over the simulation time step. After the calculations are complete, updated species composition and state information is passed back to the original KIVA cells using a remapping process described below.

As in the original Multi-Zone formulation of Babajimopoulos [99], the computational cells were grouped into zones based on temperature and progress equivalence ratio φ,

defined as:

$$\varphi = \frac{2C^{\#}_{-CO_2} + \frac{1}{2}H^{\#}_{-H_2O} - \frac{z}{x}C^{\#}_{-CO_2}}{O^{\#}_{-CO_2-H_2O} - \frac{z}{x}C^{\#}_{-CO_2}} \tag{3.23}$$

Where $C^{\#}_{-CO_2}$, $H^{\#}_{-H_2O}$, and $O^{\#}_{-CO_2-H_2O}$ are the number of C, H, and O atoms not including those in the complete combustion products (CO_2 and H_2O). The z/x term is the ratio of oxygen to carbon atoms in the fuel, equal to zero for non-oxygenated fuels such as isooctane. For mixtures with zero reaction progress this definition is identical to the fuel/O_2 equivalence ratio. For a lean mixture φ is less than 1.0, while for a stoichiometric mixture φ = 1.0. Rich mixtures range from $\varphi > 1.0$ to ∞, when the mixture is composed of pure fuel. To better capture this wide range of potential conditions that may occur in a direct injected engine a new progress equivalence ratio is adopted in this work:

$$\varphi^* = \begin{cases} \varphi & : \varphi \leq 1.0 \\ 2 - \frac{1}{\varphi} & : \varphi > 1.0 \end{cases} \tag{3.24}$$

Where the range of φ^* is 0.0 to 2.0 from pure air to pure fuel. This scaling prevents the model from creating an excessively large number of chemistry zones for rich cells with high levels of reaction progress, which can have extremely large differences in φ for very similar compositions.

For lean mixtures φ and φ^* provide a measure of reaction progress, ranging from the global equivalence ratio Φ for no combustion to zero for complete combustion. Unfortunately φ is invariant for stoichiometric conditions, and does not agree with the global equivalence ratio when EGR is present in the cell. To address the stoichiometric invariance, Kodavasal extended the Multi-Zone grouping procedure to include the mass average internal energy of formation (u_f) of each cell [142]. However, to address both shortcomings this work neglects the u_f criteria and substitutes the fraction of stoichiometric combustion products in the cell, X_{SCP} as defined in Chapter 2.

In the current work, computational cells are grouped into chemistry zones using

maximum zone sizes of 0.03 in φ^* and 0.1 in X_{SCP}. This resolution in φ^* is similar to that used by Kodavasal for Multi-Zone studies of NVO and direct injection charge preparation strategies under HCCI operation [16]. For operating conditions with large thermal stratification, as found in the NVO engines simulated in this work, the 100 K zone temperature limits used by Babajimopoulos [99] provided poor agreement with simulations with detailed chemistry in every cell. Kodavasal overcame this limitation by imposing a maximum zone size of 5 K, at the cost of increased computational expense throughout the simulation. A new approach was developed where the maximum temperature width of each chemistry zone is a function of the lowest temperature cell assigned to the zone. The zone temperature widths used in this work are presented in Figure 3.3, where the highest resolution of 5 K is used from 900 K to 1200 K where accurate predictions of auto-ignition chemistry are most critical for predicting combustion behavior.

The average temperature, pressure, and composition of the computational cells in each chemistry zone are used to perform chemical kinetic calculations over the timestep with CHEMKIN [143]. After the kinetics calculation is complete, the new composition is remapped from the zone to the individual cells through a variable *ch*, which represents the number of C and H atoms in non-product species:

$$ch = 2\mathrm{C}^{\#}_{-\mathrm{CO_2}} + \frac{\mathrm{H}^{\#}_{-\mathrm{H_2O}}}{2} \tag{3.25}$$

For all species except CO_2, H_2O, O_2 and N_2, the new mass of species m is calculated by:

$$m_m = \frac{ch_{\mathrm{cell}}}{ch_{\mathrm{zone}}} m_{m,\mathrm{zone}} \tag{3.26}$$

The new masses of CO_2, H_2O, O_2 and N_2 are calculated through atom balances in the cell to enforce that the overall cell mass remains invariant over the chemistry calculation, as well as ensuring atom conservation. Additional details of the remapping procedure are provided in the original formulation of the Multi-Zone model [99, 142].

In the KIVA-CFMZ model two separate calls to the Multi-Zone chemistry model are conducted, as indicated by Figure 3.2. Each call uses the species composition in one of the sub-grid model zones, Product or Reactant, as the cell composition for Multi-Zone chemistry. For simulation stability the Product zone calls only consider cells where 5% or more of the cell mass has been consumed by the reaction front:

$$\bar{c}_1 = \left(1 - \frac{m_u}{m_{\text{cell}}}\right) \tag{3.27}$$

The chemical source terms in Equations 3.11 and 3.12 for species density change due reactions in the Product (b) or Reactant (u) zones is given for zone z by:

$$\dot{\rho}^C_{m,z} = \frac{m_z}{V}\left(\frac{Y_m^{z,\text{MZ},e} - Y_m^{z,\text{MZ},i}}{\Delta t}\right) \tag{3.28}$$

While the source terms in Equation 3.13 for zone z are calculated given by:

$$\dot{Q}^C_z = -\rho \frac{\left(\sum_m Y_m u_m^0\right)^{\text{MZ},e} - \left(\sum_m Y_m u_m^0\right)^{\text{MZ},i}}{\Delta t} \tag{3.29}$$

The Reactant zone enthalpy source term is calculated in a similar manner using the enthalpy of formation of species m, h_m^0:

$$\dot{Q}^C_{u,\text{AI}} = -\rho \frac{\left(\sum_m Y_m^u h_m^0\right)^{\text{MZ},e} - \left(\sum_m Y_m^u h_m^0\right)^{\text{MZ},i}}{\Delta t} \tag{3.30}$$

Where the superscript MZ, e indicates the provisionally updated cell composition after the Multi-Zone chemistry calculation, and MZ, i indicates the composition prior to the species update.

3.3 Fuel Injection and Vaporization

The dimensions of the computational cells typically used by KIVA-3v are too large to directly resolve fuel droplets from introduced from an injector. To facilitate modeling of engines with port or direct fuel injection, KIVA-3v provides a framework for tracking fuel particles in a Lagrangian manner independent of the computational grid resolution. Rather than track the extremely high number of individual fuel droplets from an automotive fuel injector, KIVA groups particles of similar size and velocity into 'parcels' and tracks those instead. In the following discussion, the terms 'particle', 'parcel' and 'droplet' will be used interchangeably.

The source terms for the change in species density, internal energy, and unburned enthalpy due to fuel vaporization in Equations 3.2, 3.4, 3.3 and 3.5 are calculated by summing the contributions of each particle within a given computational cell:

$$\dot{\rho}_m^S = \left(\sum_{p=1}^{np} \Delta m_p \right) \frac{1}{\Delta t} \tag{3.31}$$

$$\dot{Q}^S = \left(\sum_{p=1}^{np} \Delta I_p \right) \frac{1}{\Delta t} \tag{3.32}$$

Where np is the number of droplets in the cell, Δm_p is the mass vaporized from droplet p during the timestep, and ΔI_p is the change in internal energy due heat transfer between the cell gas phase and droplet p. When the droplet temperature, T_p, is below the saturation temperature, T_{sat}, at the current pressure, the standard KIVA-3v methods for vaporization of liquid droplets and wall films are used to calculate Δm_p and ΔI_p. Under conditions where T_p is equal to or greater than T_{sat}, the newly implemented methods for fuel boiling described in Section 3.3.2 are used instead.

3.3.1 Direct Injection Model

An existing fuel injection model for gasoline injectors was added to the KIVA-CFMZ model to facilitate open cycle simulations. The direct injection model was previously developed at the University of Michigan by Chryssakis for SI engine simulations [144–148]. The model addresses sprays emerging from a high-pressure swirl injector typical of those expected to be available in a gasoline engine implementing SACI combustion. It accounts for both the primary and secondary atomization of fuel, as well as the transition of the initial pre-swirl spray with a solid cone to the steady state behavior of the main injection event with a hollow-cone structure. The primary breakup model was based on the Linearized Instability Sheet Atomization (LISA) model [149, 150], while the droplet size was calculated with a Rosin-Rammler cumulative distribution [151]. Secondary droplet breakup was calculated with the Taylor Analogy Breakup (TAB) model [152]. Spray-wall impingement is accounted for using a model developed by Grover et al. [153]. This model has previously been validated and showed good agreement with experimental PLIF measurements in an optical engine.

3.3.2 Fuel Boiling Model

New sub-models for liquid fuel boiling were developed and implemented into the KIVA-CFMZ model to address shortcomings in the standard KIVA-3v fuel vaporization methods. Under conditions where T_p is equal to or greater than T_{sat} and boiling should occur, KIVA-3v instead converts the entire fuel droplet from liquid to vapor instantaneously and deposits all of the fuel mass and energy into the computational cell. For hydrocarbon fuels of interest with positive heats of vaporization, this leads to significant decreases in cell temperature and can result in non-physical negative temperatures and fatal simulation instabilities. The newly implemented boiling models described below were developed to replace this undesirable behavior with physically correct calculations of the Δm_p and ΔI_p terms required by Equations 3.31 and 3.32.

Three new sub-models were implemented to capture fuel boiling behavior under different physical configurations:

- Free droplets boiling with $T_p = T_{\text{sat}}$
- Wall film particles boiling with $T_p = T_{\text{sat}}$
- Particles flash boiling with $T_p > T_{\text{sat}}$

Under conditions where $T_p = T_{\text{sat}}$, heat transfer into the liquid determines the fuel boiling rate based on the heat of vaporization of the fuel. Alternatively, when the liquid is superheated, $T_p > T_{\text{sat}}$, there is no heat transfer between the liquid fuel and the ambient cell, energy in the liquid simultaneously vaporizes the fuel and the remaining liquid in the droplet cools to T_{sat}.

Free Droplet Boiling

The free particle boiling model is invoked for fuel droplets with T_p within 1 K of T_{sat} in cells with ambient temperatures, T_{cell}, greater than T_p. The liquid droplet is assumed to be spherical and at constant uniform temperature throughout the timestep, with no dissolved gas. Under these assumptions particle boiling is a well understood process, summarized by Law [154], included as model problems in text books [155, 156] and CFD software user manuals (Fluent) [157].

Conservation of energy for a spherical control volume of arbitrary radius r around the particle gives:

$$\frac{d}{dr}\left(r^2 \frac{dT}{dr}\right) = \frac{\dot{m}_b C_{p,g}}{4\pi k} \frac{dT}{dr} \tag{3.33}$$

Where $\dot{m}_b$ is the mass boiling rate through the control surface, $C_{p,g}$ is the heat capacity of the gas, and k is the thermal conductivity of the gas.

Solving for $T(r)$ with boundary conditions ($T(r \to \infty) = T_{\text{cell}}$ and $T(r = r_p) = T_p$) gives:

$$T(r) = \frac{\left(T_{\text{cell}} - T_{\text{p}}\right) e^{\frac{-Z\dot{m}_b}{r}} - T_{\text{cell}} e^{\frac{-Z\dot{m}_b}{r_p}} + T_{\text{p}}}{1 - e^{\frac{-Z\dot{m}_b}{r_p}}} \tag{3.34}$$

Where r_p is the droplet radius and Z is defined for convenience as:

$$Z = \frac{C_{p,g}}{4\pi k} \tag{3.35}$$

At the interface between the liquid and vapor phases the heat transfer into the droplet provides the energy required to vaporize the liquid fuel based on the heat of vaporization h_{fg}:

$$\dot{Q} = 4\pi k r_p^2 \frac{dT}{dr}\bigg|_{r_p} = \dot{m}_b \left(h_{vap} - h_{liq}\right) = \dot{m} h_{fg} \tag{3.36}$$

Accounting for heat transfer due to droplet motion relative to the ambient gas, and solving for the mass boiling rate $\dot{m}$ gives:

$$\dot{m}_b = \frac{4\pi k r_p}{C_{p,g}} \left(1 + 0.23 Re_d^{(1/2)}\right) \ln\left(B+1\right) \tag{3.37}$$

$$B = \frac{C_{p,g}\left(T_{\text{cell}} - T_p\right)}{h_{fg}} \tag{3.38}$$

The resulting particle source term contributions for a boiling particle are:

$$\Delta m_p = \dot{m}_b \Delta t \tag{3.39}$$

$$\Delta I_p = \dot{m}_b h_{fg} \Delta t \tag{3.40}$$

Wall Film Boiling

The wall film boiling model is invoked for wall film parcels with T_p within 1 K of T_{sat} in cells with ambient temperatures, T_{cell}, greater than T_p. The derivation presented here is based on the original wall film model in KIVA, where the wall functions for heat transfer were adjusted to account for the presence of a vaporizing liquid film [158]. In the KIVA wall film model, the 'parcels' located on the wall track the film height rather than a droplet radius, complicating the geometry of the boiling model.

Assuming that the liquid wall film is at a constant temperature T_p, heat transfer into the film results mass boiling based on the heat of vaporization of the liquid fuel, h_{fg}:

$$\dot{m}_{fl,b} h_{fg} = \dot{q}_{bl,w} + \dot{q}_{bl,g} \tag{3.41}$$

Where $\dot{m}_{fl,b}$ is the mass boiling rate, $\dot{q}_{bl,w}$ is the heat transfer rate from the solid wall to the film, and $\dot{q}_{bl,g}$ is the heat transfer rate from the ambient gas to the film, all on a per unit area basis.

Heat transfer from the solid wall to the film is calculated with the Rohsenow film boiling correlation [159]:

$$\dot{q}_{bl,w} = \mu_l h_{fg} \sqrt{\frac{g(\rho_l - \rho_v)}{\sigma}} \left(\frac{C_{p,l} T_{\text{wall}} - T_p}{c_r h_{fg} Pr_l^n} \right) \tag{3.42}$$

Where c_r and n are empirical constants for n-pentane boiling on polished copper, equal to 0.0154 and 1.7, respectively. The liquid viscosity is μ_l, surface tension is σ, while the densities of the liquid and gas phases of the fuel are ρ_l and ρ_v respectively, and Pr_l is the Prantl number of the liquid. The acceleration by gravity, g, is calculated assuming the film is on top of the solid surface, consistent with fuel injected onto the back of an intake valve or pooling on the piston top.

Heat transfer from the film to the gas is calculated using the modified wall function:

$$\dot{q}_{bl,g} = \frac{\dot{m}_{fl,b} C_{p,g} (T_{\text{cell}} - T_p)}{e^{\dot{m}_{fl,b} ht} - 1} \tag{3.43}$$

Where ht is the heat transfer coefficient calculated by the Law of the Wall before accounting for vaporization.

The resulting equation for the mass boiling rate is:

$$\dot{m}_{fl,b} h_{fg} = \mu_l h_{fg} \sqrt{\frac{g(\rho_l - \rho_v)}{\sigma}} \left(\frac{C_{p,l} T_{\text{wall}} - T_p}{c_r h_{fg} Pr_l^n} \right) + \frac{\dot{m}_{fl,b} C_{p,g} (T_{\text{cell}} - T_p)}{e^{\dot{m}_{fl,b} ht} - 1} \tag{3.44}$$

Where the mass boiling rate $\dot{m}_{fl,b}$ is solved for numerically.

The resulting particle source term contributions for a boiling film are:

$$\Delta m = \dot{m}_{fl,b} A_{\text{wall}} \Delta t \tag{3.45}$$

$$\Delta I = \left(\dot{m}_{fl,b} h_{fg} - \dot{q}_{bl,w} \right) A_{\text{wall}} \Delta t \tag{3.46}$$

Flash Boiling

The flash boiling model is invoked for fuel droplets and wall film parcels with T_p more than 1 K above T_{sat}. Flash boiling occurs when a droplet is superheated and contains more energy than it can stably hold at its current temperature. The 'extra' energy associated with the superheating vaporizes part of the droplet mass while simultaneously decreasing the temperature of the remaining liquid until it reaches T_{sat}.

Treating the particle as a control mass, conservation of mass gives:

$$m_{\text{vap}} + m_{\text{sat}} = m_{\text{p}} \tag{3.47}$$

Where m_{vap} is the mass of vapor generated by the flash boiling process, m_{p} and m_{sat} are the initial and final masses of liquid, respectively.

Conservation of energy for a control mass undergoing a constant pressure process with no external heat transfer gives:

$$h_v m_{\text{vap}} + e_{\text{sat}} m_{\text{sat}} = e_{\text{p}} m_{\text{p}} \tag{3.48}$$

Where the h_v is specific enthalpy of the gas, and the enthalpy of the liquid has been approximated with the specific internal energy, e, by assuming that the specific volume is low. The process is transient and the fuel is vaporized continuously while the droplet temperature decreases from T_p to T_{sat}. Therefore a completely rigorous treatment would

integrate h_v over the process, but for simplicity h_v is evaluated at the average temperature between T_p and T_{sat}.

Solving Equations 3.47 and 3.48 simultaneously for the particle mass after flash boiling gives:

$$m_{\text{sat}} = m_{\text{p}} \frac{e_{\text{p}} - h_f}{e_{\text{sat}} - h_f} \tag{3.49}$$

The resulting source term contributions for a particle that flash boils are then simply:

$$\Delta m_p = m_{\text{vap}} \tag{3.50}$$

$$\Delta I_p = m_{\text{vap}} h_{fg} \tag{3.51}$$

3.4 Spark Ignition Modeling

A new spark ignition model was developed and implemented into the KIVA-CFMZ model to reduce dependence on the mesh resolution in the vicinity of the spark plug. In the original KIVA-CFMZ formulation [70], and previous implementations of the Coherent Flamelet model [98], a source term, S_3, was included in the flame surface density transport equation, Equation 3.9. Those models applied S_3 to a single 'ignition' cell to initialize Equation 3.9. While these previous implementations provided good overall agreement between model predictions and experimental data, the potential for mesh dependence is un-desirable and is addressed with a new spark ignition model.

Prior to the spark ignition timing and the invocation of the spark model, there are no reaction fronts present in the combustion chamber, and the flame surface density, Σ, is zero everywhere. When the spark model is initialized, a spherical laminar flame kernel is established at the specified spark plug location with an initial radius of 0.5mm, consistent with observations from optical engine experiments [160, 161]. The spark kernel location and growth rate are tracked by a sphere of Largrangian particles expanding outward from the initial spark location, similar to the approach of Tan and Reitz [162], with existing KIVA-3v

subroutines leveraged for particle motion. The expansion speed of each ignition particle, i, is determined from the combination of the stretch corrected laminar flame speed, $S_{L,I}$, and effective plasma velocity, S_{plasma}:

$$\frac{dr_i}{dt} = \frac{\rho_u}{\rho_b}\left(S_{L,I} + S_{\text{plasma}}\right) \tag{3.52}$$

Where ρ_u is the density of the unburned gas in front of the kernel and ρ_b is the density of the burned gas within the kernel.

The effective plasma velocity is obtained from the thermodynamic model of Tan and Rietz [162]:

$$S_{\text{plasma}} = \frac{\dot{Q}_{\text{spark}}\eta_{\text{eff}}}{4\pi r_i^2\left[\rho_u\left(U_k - h_u\right) + p\frac{\rho_u}{\rho_k}\right]} \tag{3.53}$$

Where U_k is the specific internal energy of the burned gas at the adiabatic flame temperature, and h_u is the unburned gas enthalpy.

The instantaneous spark discharge rate, $\dot{Q}_{\text{spark}}$, is calculated from the correlation of Lim et al. [163]:

$$\dot{Q}_{\text{spark}} = 1.6088\left(\frac{t_{\text{ign}}}{t_{\text{dur}}^2} + \frac{1.78621}{t_{\text{dur}}}\right)Q_{\text{total}} \tag{3.54}$$

Where t_{ign} is the time from the start of the spark discharge and t_{dur} is the total discharge duration, while Q_{total} is the total spark energy deposited throughout the entire discharge process.

The instantaneous spark efficiency during the discharge phase is estimated with the correlation of Ko et al. [164]:

$$\eta_{\text{eff}} = 0.435\text{e}^{\frac{-t_{\text{ign}}}{8.0\times10^{-4}}} \tag{3.55}$$

The stretch corrected laminar flame speed, $S_{L,I}$, is derived from the expressions presented

by Herweg and Maly for a stretched flame [160]:

$$S_{L,I} = S_L I_0 \tag{3.56}$$

$$I_0 = 1 - K_l \tag{3.57}$$

$$I_0 = 1 - 2\frac{\delta}{S_L}\frac{1}{r_i}\frac{dr_i}{dt} \tag{3.58}$$

$$I_0 = 1 - 2\frac{\delta}{S_L}\frac{1}{r_i}\frac{\rho_u}{\rho_k}\left(S_L + S_{\text{plasma}}\right) \tag{3.59}$$

The Lewis number is assumed to be unity for these calculations, and any negative $S_{L,I}$ predictions are set to 0.

Following the approach of Boudier et al. [136], as the ignition kernel grows it transitions from a purely laminar phase to a laminar-turbulent phase and begins to wrinkle. The resulting kernel area, A_{kernel}, is integrated according to:

$$\frac{dA_{\text{kernel}}}{dt} = \frac{d}{dt}\left(4\pi r_k^2\right) + K_t A_{\text{kernel}} \tag{3.60}$$

Where r_k is the average radius of the ignition kernel, and K_t is supplied by the ITNFS flame stretch model discussed in Section 3.2.1:

$$K_t = S_2 = \alpha_0 \Gamma_{\bar{K}} \frac{\varepsilon}{k} \tag{3.61}$$

Consistent with the previous work of Boudier et al. [136], the turbulent stretch term, K_t is not calculated until 0.1 ms after the start of the spark ignition event.

The flame surface density in cells containing ignition particles is directly imposed based on the fraction of the kernel area contained within the cell:

$$\Sigma_{\text{cell}} = \frac{n_{p,\text{cell}}}{n_{p,\text{total}}}\frac{A_{\text{kernel}}}{V_{\text{cell}}} \tag{3.62}$$

Where the $n_{p,\text{cell}}$ is the number of ignition particles in the cell and $n_{p,\text{total}}$ is the total number

of ignition particles in the kernel.

The species and internal energy changes due to the ignition kernel propagation through the computational cells is accounted for with calls to the coherent flamelet model subroutines. Source terms previously described in Section 3.2.1 by Equations 3.19-3.21 are calculated with the imposed Σ_{cell} and S_L replaced by the kernel expansion speed $S_k = (S_{L,I} + S_{\text{plasma}})$.

The ignition routine remains active until a series of exit criteria are met. First is that the plasma velocity is less than 10% of the kernel expansion speed, $S_{\text{plasma}} < 0.1\ S_k$, indicating that the spark energy discharge phase has completed. Second is that the kernel has reached sufficient size to be wrinkled by turbulence. The second criteria is met when either the turbulent strain, K_t, exceeds the geometric strain, K_l, or when the kernel radius reaches 2 mm, consistent with previous modeling and experimental observations of wrinkling kernels [160, 161]. When the ignition model exits, the imposed Σ_{cell} values are mapped onto Equation 3.14 to initialize the Coherent Flamelet model.

3.5 Computational Improvements to Enable Open Cycle Simulations

A number of computational improvements were made to base KIVA-3v code that serves as the framework for the KIVA-CFMZ combustion model. Small improvements such as high efficiency sorting algorithms, adjustments to memory management and array access ordering, and accelerated input/output performance are not discussed here. Two major improvements that are key enablers for open cycle simulations and repeated cycle simulations are discussed below.

3.5.1 Chemical Mechanism Substitution

During the breathing portion of an open cycle simulation, where the valves are open, a large fraction of the computational cost in KIVA-3v is associated with the solution of the

transport equations for each species density. This is particularly pronounced immediately after a valve opens as the gas experiences a large pressure gradient and accelerates through the valve open area. For the 215 species isooctane mechanism of Tham et al. [124] used for laminar flame simulations in Chapter 2, the KIVA-CFMZ model must solve 432 species transport equations (mixture averaged species, Reactant zone species, EGR, and Σ). Initial simulations with this mechanism required execution times in excess of 200 hours to model the breathing process from shortly before EVO to IVC. This is prohibitively expensive and limits the model from being applied for parametric studies of SACI combustion, or from simulated repeated cycles.

To address this issue subroutines were developed to substitute one chemical mechanism with another mechanism midway through a simulation. There are two types of substitution possible, from a small mechanism to a large mechanism, and from a large mechanism to a small mechanism.

In the first case, a small mechanism containing only major species can be used from simulation initialization through the open cycle breathing process. By reducing the number of species from 215 to 5 (Fuel, O_2, N_2, CO_2, and H_2O), the simulation execution time from EVO to IVC can be reduced to less than 20 hours. At IVC a simulation restart file is written containing the entire simulation state. When the model is re-initialized with a larger mechanism, it reads this restart file, identifies the location of each of the species from the small mechanism in the new mechanism and imposes the species density from the restart file in that segment of the new species density array. Species density for all species in the large mechanism that are not found in the small mechanism are set to zero. Cell temperature is held constant and the internal energy is re-calculated with the new mechanism, to account for any differences in the species properties between mechanisms. This procedure is used extensively in the simulations described in Chapters 4-6.

The second case, reducing a large mechanism to a small one, is more complicated. After combustion there may be trace non-zero densities for most or all species in a mechanism, so

they cannot be simply 'removed'. When the code is invoked to reduce a mechanism, the user specifies a threshold mass fraction. All species with mass fractions greater than the threshold value, anywhere in the simulation domain, are retained for use with the reduced mechanism. Species that do not meet the threshold are zeroed, and the remaining species densities are adjusted to maintain the total cell mass. The remapping procedure described in Section 3.2.2 is used in each cell to calculate the new mass fractions required to maintain cell *ch*, total mass, atomic composition, and equivalence ratio. Internal energy is re-calculated at constant cell temperature with the new compositions to eliminate any apparent heat release from the mechanism exchange. Mechanism exchange in this manner can be used after the completion of combustion to facilitate repeated cycle simulations with reasonable run-times. Initial testing showed that the results a repeated cycle simulation were sensitive to the choice of threshold value, as well as the crank angle location where the mechanism reduction occurred. Further study was not conducted in the current work.

3.5.2 Parallel Chemistry using MPI

As mentioned in Section 3.2.2, chemical kinetics calculations account for a large portion of the computational cost of a KIVA simulation near TDC. The increased Multi-Zone resolution required to capture the thermal and compositional stratification observed in an open cycle simulation with direct injection adds significantly to this cost. To improve simulation speed and scalability, the chemistry subroutines were parallelized to take advantage of currently available multi-core computing platforms.

A Master-Slave parallel configuration was implemented using the standardized Message Passing Interface (MPI) communications interface [165–167], with a conceptual diagram of the configuration presented in Figure 3.4. The Master node performs all of the KIVA-CFMZ calculations in the same manner that a serial simulation of a single processor would, except the Multi-Zone model and the Coherent Flamelet model. In the Multi-Zone model, when the computational domain is divided into chemistry zones the state of each zone is stored in

a queue for parallel evaluation. The Master node assigns a chemistry zone to each of the Slave nodes, which perform the chemical kinetics calculations to determine the new zone state and return the result to the Master for re-mapping back to the physical domain. When a result is returned the next zone in the queue is assigned to the Slave node. No predictive or adaptive scheduling is used for this process. The same configuration is used in the Coherent Flamelet model to parallelize the calculation of the equilibrium composition all of the cells containing reaction fronts.

The speedup from parallel execution varied throughout a simulation. Near TDC where chemistry costs are a high fraction of the total computational expense very good scaling was observed, while earlier in the simulation near IVC parallelization provided little benefit. These scaling results are consistent with known well behavior of parallel computing, stated by Amdahls law [168] as:

$$S(N) = \frac{1}{(1-P) + \frac{P}{N}} \tag{3.63}$$

Where $S(N)$ is the maximum speedup using N processors and P is the fraction of the program that can be parallelized. The implication of this law in the context of the KIVA-CFMZ model is that parallelization becomes more beneficial as the chemistry costs increase. These new MPI based chemistry subroutines facilitate simulations with increased chemical mechanism sizes and increased Multi-Zone resolutions (up-to chemistry in every cell).

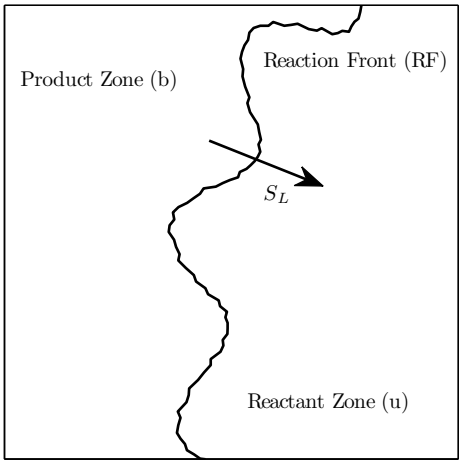

Figure 3.1 Conceptual diagram of the KIVA-CFMZ sub-grid model for each computational cell.

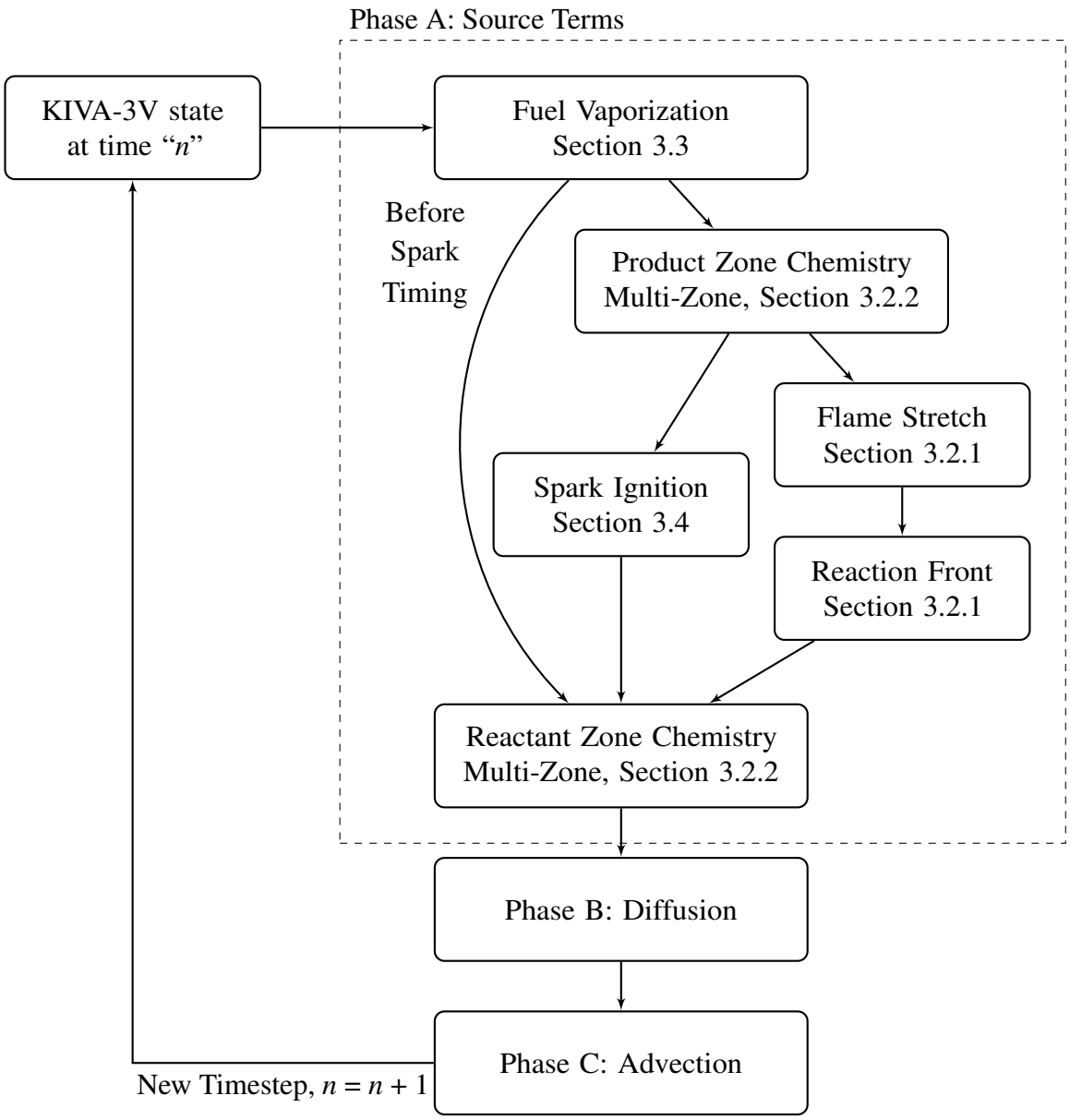

Figure 3.2 Flow chart for major KIVA-CFMZ model solution steps related to combustion modeling. Sections discussing specific steps as indicated.

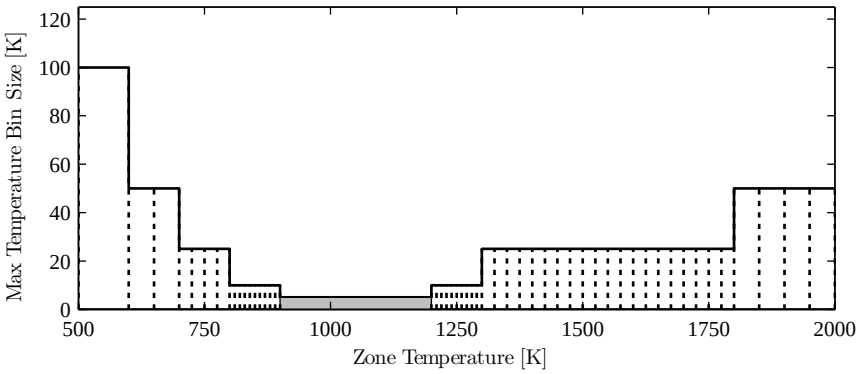

Figure 3.3 Variable maximum temperature bin size used in the Multi-Zone chemistry model. The highest resolution of 5 K wide temperature bins is between 900 K and 1200 K, indicated by the filled grey region. This corresponds to the temperature region where auto-ignition chemistry is most sensitive to changes in temperature.

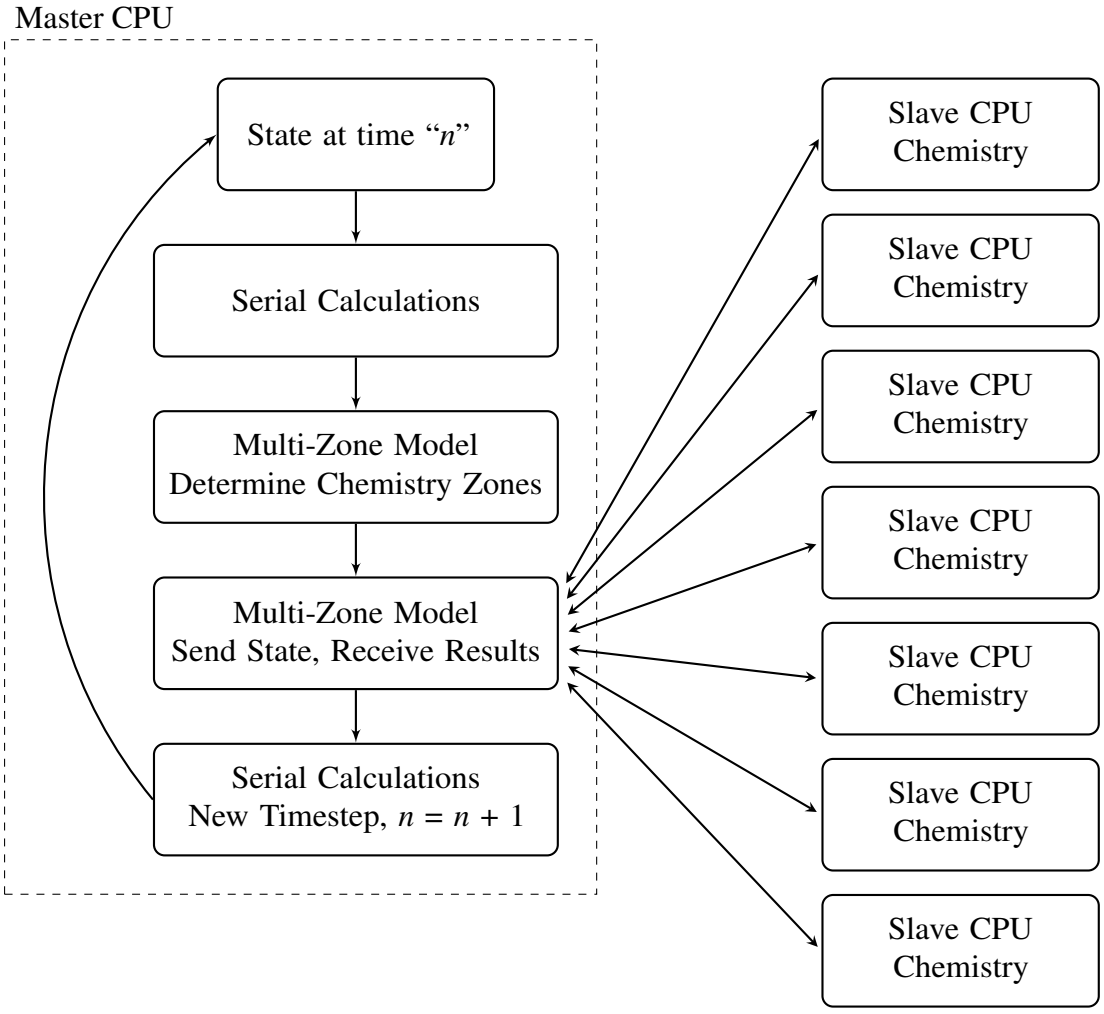

Figure 3.4 Schematic of parallel processing configuration for KIVA-CFMZ using MPI. Master CPU performs most KIVA calculations serially, then assigns expensive chemical kinetic updates for chemistry zones within the Multi-Zone model to slave CPUs for parallel execution.

Chapter 4

Comparison of KIVA-CFMZ Model Predictions with Engine Experiments

Several sets of experimental SI, HCCI, and SACI data were used to evaluate the predictive capabilities of the KIVA-CFMZ model. Previous and concurrent investigations with this model have shown good agreement with HCCI, SI and SACI engine data under primarily air dilute operating conditions [70, 101], as well as under EGR dilute HCCI conditions [16]. Additional evaluation here serves as a test of the laminar flame speed and thickness correlations developed in Chapter 2 for EGR dilute conditions, as well as providing baseline confidence for detailed investigations of SACI combustion behavior in later chapters. This chapter describes the experimental setup modeled, provides the model configurations and settings used throughout this work, and presents some of the evaluation metrics that will be used to compare the model predictions to experimentally reported SACI combustion behavior.

4.1 Experimental Engine Setup

Experimental data for SI, HCCI, and SACI combustion were provided by Dr. Laura Olesky. Detailed documentation of the experimental facility and results are reported in other publications [29, 38, 48, 67] and not repeated here. Key geometric parameters of the fully flexible valve actuation (FFVA) direct-injected single cylinder research engine are provided in Table 4.1.

The FFVA system provided independent control of lift, timing, and duration of each valve.

Symmetric negative valve overlap (NVO) operation was used to retain high temperature internal exhaust gas residuals to enable SACI combustion in the 12.4:1 compression ratio engine. Intake valve closing (IVC) was held constant at 150° before top dead center (bTDC of combustion), while exhaust valve opening (EVO) was constant at 150° after top dead center (aTDC). An external EGR loop allowed for the addition of cooled EGR dilution through the intake. The fuel in the experiments was 87-octane research grade gasoline, injected during NVO at 330° bTDC to allow time for mixing prior to spark ignition. A centrally mounted spark plug with a maximum coil energy of 70 mJ was used to initiate flame propagation during SI and SACI operation.

High speed cylinder pressure data were collected at 0.1° CA resolution for 200 consecutive cycles for each condition studied. Dynamic absolute pressure data were also collected at the same resolution in the intake and exhaust manifolds. Heat release analysis of these data was conducted using the approach developed by Ortiz-Soto [37], which includes estimates of the residual fraction during NVO operation from Fitzgerald et al. [169].

4.2 Model Configuration

All of the combustion conditions simulated with the KIVA-CFMZ model reported in this work were configured in a consistent manner as described in the following sections.

4.2.1 Computational Mesh

An approximately 156,000 cell detailed 3D mesh matching the geometry of the metal engine of Olesky et al. [38, 48, 67] was used in this study. The mesh includes the open intake and exhaust ports, pent roof cylinder head, asymmetrical bowl-in piston, and moving valves. At TDC the combustion chamber was composed of approximately 22,000 cells. Key geometric parameters of the mesh and engine are included in Table 4.1. Two views of the mesh are presented in Figure 4.1, oriented such that the asymmetrical intake ports are on the right and

the symmetric exhaust ports are on the left.

Model valve motion is imposed from the experimentally reported high speed lift measurements for each valve under each operating condition. The FFVA system's hydraulically controlled valves do not follow traditional cam profiles, but instead have fast nearly linear motion during opening and closing while holding a constant lift for most of the duration. Figure 4.2 shows a typical set of lift profiles for an HCCI operating condition with 160° NVO. Other lifts and durations at other operating conditions maintain the same characteristic shape for the lift profile.

A ringpack and crevice blowby model was used in these engine simulations, configured based on measurements of the experimental piston and rings. The model was developed based on the work of Namazian and Heywood [170] and Zhao and Lee [171], and is presented in detail as implemented in KIVA-CFMZ by Martz [172]. The top-land crevice volume was 0.473 cm^3, approximately 1% of the clearance volume. At peak pressure approximately 3% of the total charge mass was predicted to enter the crevice. For all simulations the rings remained seated firmly on the bottom of the ring grooves with negligible blowby predicted during the combustion process.

4.2.2 Boundary Conditions

The thermal boundary conditions on the solid surfaces of the mesh used in this work are included in Table 4.2. Cylinder wall, head, piston top, and intake valve surface temperatures were estimated based on zero-dimensional cycle simulations conducted in GT-Power [173, 174], while the exhaust valve temperatures are based on the optical measurements of exhaust valve surfaces from Omrane et al. [175]. Temperatures were varied with engine load, where the SACI operating conditions at approximately 6 bar $IMEP_g$ were assigned temperatures 25 K higher than the HCCI and SI operating conditions between 3-4 bar $IMEP_g$.

The intake temperature and composition at the open boundary were set based on the

experimentally reported measurements on a case by case basis. External EGR was assumed to be composed of complete combustion products at the experimentally measured global equivalence ratio. The exhaust boundary temperature and composition was set in a similar manner by assuming complete combustion products in the exhaust. There is no "last in first out" in the model to account for reversing flow at the exhaust boundary, however this is not expected to impact the combustion behavior predictions.

Crank angle varying boundary pressures in the intake and exhaust manifolds were imposed on a case by case basis from the high speed manifold pressure measurements of the experiments. Figure 4.3 presents example manifold pressure data for a SACI operating condition described in further detail in Section 4.5. There are significant pressure variations in the vicinity of the valve closures, with peak to peak amplitudes of approximately 0.2 bar in both manifolds. Due to differences between the location of the pressure measurements and the location of the mesh boundary, there is some uncertainty in the behavior of the pressure dynamics and the resulting pressure at the valve seat the instant the valve closes. To compensate for this uncertainty, the intake and exhaust manifold pressures used in the simulations were shifted by applying an offset of up to 0.1 bar. Offsets for each experimental condition modeled were varied such that the model pressure predictions at TDC of NVO and 20° bTDC of firing agreed with the experimentally measured pressures.

4.2.3 Simulation Procedure

Open cycle KIVA-CFMZ simulations were conducted for all of the HCCI, SI, and SACI combustion conditions studied in this work. A schematic of the simulations with key events is presented in Figure 4.4. Simulations were initialized at 640° bTDC of combustion, during the expansion stroke of the previous engine cycle, prior to exhaust valve opening. The cylinder pressure was initialized with the experimental pressure at 640° bTDC, composition was assumed to be complete combustion products at the experimentally measured equivalence ratio, while the initial temperature was calculated with the equation of state using an estimate

of the total trapped mass supplied by GT-Power and the approach of Ortiz-Soto [37,173,174]. The standard k-epsilon turbulence model was used for closure of the Reynold's stress and flux terms appearing in the RANS transport equations, while the initial velocity and turbulent kinetic energy of the flow field were imposed from the results of a motored simulation where the model was run 720° through the entire breathing process back to the initial crank angle.

To reduce the computational expense of the open cycle, the KIVA simulations used a non-reacting 5 species mechanism (isooctane, O_2, N_2, CO_2 and H_2O) during the gas exchange process, including the trapping and recompression of residuals during NVO, fuel injection, and the intake of fresh air and external EGR. Liquid isooctane fuel was injected directly into the cylinder at 330° bTDC, during expansion of NVO, modeled using the approach described in Section 3.3. At 120° bTDC, shortly after IVC at 150° bTDC, a restart file was written and the simulations were re-initialized for detailed chemistry with a full mechanism. The chemical mechanism used for end- and burned-gas chemistry in this work was the skeletal 215 species isooctane mechanism of Tham et al. [124], derived from the detailed mechanism of Curran et al. [42]. Isooctane is a commonly used surrogate fuel for modeling gasoline, and this choice is consistent with the laminar flame studies and correlations presented in Chapter 2.

For each engine operating condition modeled an iterative tuning procedure was conducted. Perturbations of ± 0.1 bar were introduced in both manifolds and the offsets required to match the model predictions to the experimental data as described in Section 4.2.2 were calculated and applied to future simulations. Flow from the cylinder to the intake manifold between 180° bTDC and IVC at 150° bTDC was observed for all conditions modeled, resulting an approximately 10% reduction of the trapped fuel mass at IVC relative to the total fuel mass injected (prescribed based on the experimentally measured fuel flow). Under steady state operation the fuel lost to the intake manifold would be re-inducted during subsequent cycles and may alter the fuel air distribution in the cylinder at IVC relative to the model predictions for a single cycle. To compensate for this loss and achieve the desired

equivalence ratio in the cylinder at IVC for the single cycle modeled here, the injected fuel mass was increased.

4.3 Comparison of Simulated and Experimental HCCI Results

The predictive capabilities of the KIVA-CFMZ model for HCCI combustion were evaluated by simulating an experimental intake manifold temperature sweep as listed in Table 4.3. The engine was operated un-throttled at 2000 rpm, with 157° NVO and 4 mm valve lifts trapping an estimated 40% internal EGR mass fraction. Fueling was held constant at 9.4 mg/cycle for an equivalence ratio of ≈0.6 and ≈3.2 bar $IMEP_g$. In order to replicate the combustion phasing of the experiments, the simulations required a constant 10 K increase in intake manifold temperature. Similar increases in intake temperature have been observed in experimental HCCI studies comparing gasoline to isooctane at constant combustion phasing [176], indicating that the required change in temperature for the model may be due to the use of isooctane as a surrogate fuel.

Figure 4.5 compares the model predictions of cylinder pressure to the mean experimental pressure for the three conditions in Table 4.3. Good agreement between the model and the experiment is observed, with both showing that as intake temperature is decreased phasing retards and peak pressure decreases. While the model shows excellent trend-wise agreement with the experiment, it over-predicts the peak cylinder pressure and pressure rise rate. Simulations of similar HCCI operating conditions reported by Kodavasal using a multi-component gasoline surrogate mechanism with the same mesh and multizone chemistry model showed better predictions of peak pressure and pressure rise rates [16], indicating that the discrepancies noted in Figure 4.5 may be related to the choice of isooctane as a surrogate mechanism.

4.4 Comparison of Simulated and Experimental SI Results

The SI combustion conditions simulated with the KIVA-CFMZ model were taken from an engine load sweep and are listed in Table 4.4. The engine was operated throttled and stoichiometric at 2000 rpm with 17° positive valve overlap and no external EGR. Spark ignition was modeled with the spark ignition model described in detail in Section 3.4, using an energy input of 80 mJ over a duration of 1.5 ms.

The primary tuning constant in the Coherent Flamelet model, α_0 in Equation 3.14, was set to 1.6 for these SI simulations. This value agrees well with values of 1.6 [177], 1.8 [139], 1.9 [70] and 2.1 [136] from previously reported engine studies. Consistent with those prior studies, the flame surface density destruction terms in Equation 3.16, β_0 and C, were assigned values of 1 and 0, respectively.

Figure 4.6 compares the model predictions of cylinder pressure to the mean experimental pressure for the conditions in Table 4.4. Excellent agreement is observed between the model and the experiment for these conditions. The magnitude and location of peak pressure are well predicted, as is the rate of pressure rise.

4.5 Comparison Procedure for SACI Results

Initial simulations of SACI combustion using the KIVA-CFMZ model were conducted with the flame model tuning parameters established for SI combustion in Section 4.4. With these settings the model significantly over predicted cylinder pressure during flame propagation prior to auto-ignition. To bring the model predictions in line with the experimental measurements the tuning parameter α_0 in Equation 3.14 was decreased from 1.6 for the SI simulations to 0.9 for SACI simulations. Such adjustment was not required in previous use of the KIVA-CFMZ model for closed cycle simulations of air dilute SI and SACI reported by Martz [70]. There are several differences between the simulations in the current work

and those conducted previously that may account for this discrepancy, including differences in the charge preparation and turbulence from modeling the open cycle breathing and direct fuel injection, differences in the engine speed range modeled (1500-2000 rpm for SI and 700 rpm for SACI previously, 2000 rpm for all conditions in the current work), and potential inaccuracies in the laminar flame speed and thickness estimations under EGR dilute conditions. As noted in Chapter 2, the correlations developed to predict laminar flame speed and thickness replicate the results of the detailed HCT simulations very well over the range of EGR dilute conditions relevant for SACI combustion. However, the lack of high pressure, EGR dilute laminar flame data leaves uncertainty as to the accuracy of the HCT simulations under these conditions. To assess this possibility as an alternative to adjusting α_0 for SACI operation, scaling factors on the predicted S_L and thickness were investigated. While maintaining $\alpha_0 = 1.6$, a factor of 0.5 was required on S_L to replicate the effect of reducing α_0, alternatively a factor of 2.0 was required on flame thickness, or simultaneous factors of 0.75 for S_L and 1.5 for thickness were required to achieve similar cylinder pressure predictions. Sensitivity to the fuel injection model was also observed, where simulations with imposed constant composition at IVC exhibited slower rates of flame growth relative to simulations with stratification introduced from the spray model. However, reducing stratification alone was insufficient to account for the differences in the required α_0. For all of the SACI simulations presented in this document α_0 was set to 0.9 and no adjustments were made to the S_L and flame thickness predictions.

Figure 4.7 shows the KIVA-CFMZ model predictions of cylinder pressure for a stoichiometric SACI combustion condition with 114° NVO and 44° bTDC spark timing, discussed in further detail in Chapter 5. It is evident from the figure that there are significant differences between the model predictions and the typically reported “mean” experimental pressure, with the model predicting higher pressures during the early flame propagation phase, higher peak pressures, and higher rates of pressure rise. However, significant cycle to cycle variation is observed between the 200 individual experimental cycles collected at this

condition, with the KIVA-CFMZ model predictions falling within the range covered by the individual experimental cycles. Figure 4.7(b) compares the KIVA-CFMZ model predictions to a selected subset of 10 experimental cycles with peak pressures most closely matching the peak pressure from the KIVA-CFMZ results, showing significantly better agreement between the model and the experiment. Pressure predictions up to 5° aTDC agree well with the experiment, as does the pressure rise rate during auto-ignition, with peak pressure and auto-ignition phasing for the model delayed by approximately 2° crank angle relative to the experiments. Additionally, there are no measured experimental cycles that agree well with the "mean" pressure trace; cycles with similar early behavior have higher peak pressure while cycles with similar peak pressure exhibit lower pressures at TDC. Figure 4.8 applies the same procedure to the second HCCI condition simulated in Section 4.3, where less cycle to cycle variability is observed and selecting a subset of experimental cycles makes less of an impact on the agreement between the model and experiment. Based on these results all subsequent SACI simulations analyzed in this work will be compared to subsets of the experimental data.

To further understand the cycle to cycle variability observed in the experimental data for SACI combustion, a representative condition from each combustion mode was examined in more detail. Figure 4.9 presents the experimental pressure data for the second HCCI condition in Table 4.3 as Figures 4.9(a)-4.9(b), the second SI case in Table 4.4 as Figures 4.9(c)-4.9(d), and the SACI condition previously mentioned as Figures 4.9(e)-4.9(f). Plots on the left show all 200 experimental cycles measured at each condition, while plots on the right show the distributions of peak pressure found within the 200 cycle sample. The calculated "mean" experimental cycle is included, as is the cycle with the median peak pressure, and the cycle closest to the mode peak pressure. Both the HCCI and SI conditions show fairly tight normal distributions of peak pressure, with variations on the order of 8 bar, while the calculated "mean" cycle lies in the middle of the distribution and is a good representation of both the median and mode cycles. The SACI condition

in Figures 4.9(e)-4.9(f) exhibits significantly greater cycle to cycle variability, with peak pressure variation on the order of 30 bar in a non-normal distribution with a longer tail on the low pressure side than the high pressure side. This non uniformity shifts the resulting "mean" pressure to lower peak pressure values than either the median or the mode cycles, which are located in the middle of the main distribution.

Figure 4.10 shows the normalized peak pressure and normalized $IMEP_g$ for the conditions in Figure 4.9. The commonly reported metric for combustion stability, the coefficient of variation (CoV) of IMEP for these conditions was 0.6%, 0.5%, and 2.9% for HCCI, SI, and SACI, respectively, and all three conditions were reported as acceptably stable. For the HCCI and SI conditions the normalized $IMEP_g$ is well within 5% of the mean for all cycles, while the SACI condition exhibits up to 10% variation skewed to low $IMEP_g$ at low peak pressure. As seen in Figure 4.10(f), the large differences in peak pressure during SACI operation are present without correspondingly large variations in $IMEP_g$, similar to the variation apparent for SI combustion in Figure 4.10(d). This indicates that the *CoV* of $IMEP_g$ is not a sufficient metric on its own to quantify the cycle to cycle variation in pressure behavior during SACI engine operation.

4.6 Summary

This Chapter presented the open cycle simulation configuration used for the KIVA-CFMZ model simulations in this work and assessed the model's ability to replicate HCCI, SI, and SACI combustion. Excellent predictive capability was demonstrated for an HCCI intake manifold temperature sweep and an SI load sweep. The KIVA-CFMZ model replicated the experimentally reported trends using configurations consistent with prior studies. Extending the model to SACI combustion diluted with EGR required adjustment to the flame model tuning parameters, a change that was not required in previous closed cycle simulation studies of primarily air dilute SI and SACI combustion. This change highlights the need for further

fundamental data to validate the sub models included in the KIVA-CFMZ model. A method was developed to compare SACI combustion simulations to experimental SACI combustion data with large degrees of cycle to cycle variability.

Table 4.1 Engine and Mesh Geometry

Parameter	Value	Unit
Displacement	550	cm^3
Bore	86.0	mm
Stroke	94.6	mm
Con. Rod Length	156.5	mm
Compression Ratio	12.4:1	

Table 4.2 Mesh Thermal Boundary Conditions.

	HCCI	SI	SACI	
Cylinder Wall	450	450	475	[K]
Piston Top	480	480	505	[K]
Head / Firedeck	450	450	475	[K]
Intake Valve	480	480	505	[K]
Exhaust Valve	650	650	675	[K]

Table 4.3 HCCI operating conditions studied for model validation, 3.2 bar $IMEP_g$, 157° NVO, 4 mm valve lifts, at 2000 rpm.

Φ Exp.	Φ Model	T_{intake} Exp. [K]	T_{intake} Model [K]
0.58	0.59	368	378
0.57	0.58	359	369
0.55	0.55	337	347

Table 4.4 SI operating conditions studied for model validation, 318 K intake temperature, 4 mm valve lifts, at 2000 rpm.

$IMEP_g$ bar	Spark Timing $^\circ$ bTDC	Fuel Mass [mg]	P_{intake} [bar]
3.0	26	9.9	0.34
3.9	24	12.8	0.42
4.6	23	14.8	0.47

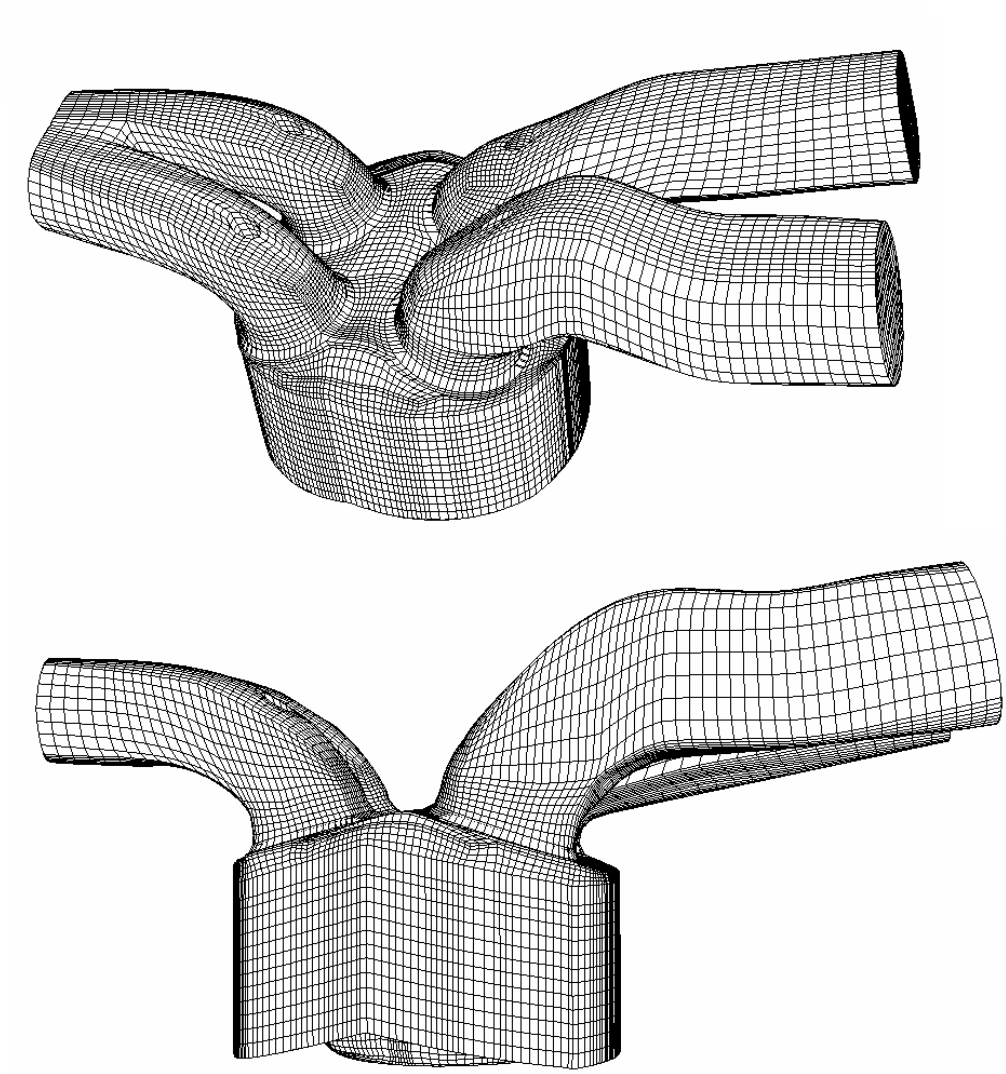

Figure 4.1 Computation mesh used in this work, containing ≈156,000 cells, based on the FFVA engine of Olesky et al. [38, 67]. Exhaust ports on the left, intake ports on the right.

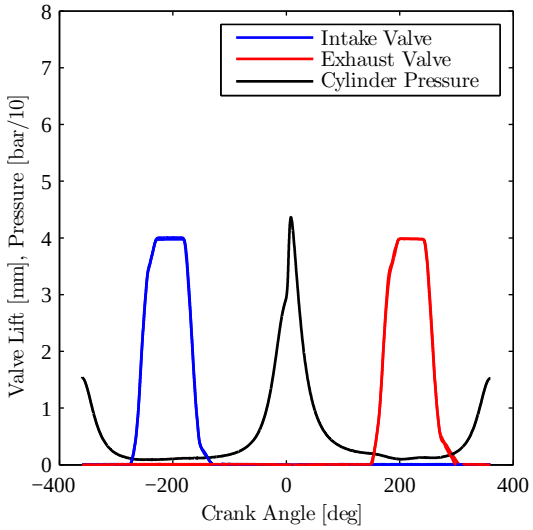

Figure 4.2 FFVA valve lifts for HCCI operation with negative valve overlap.

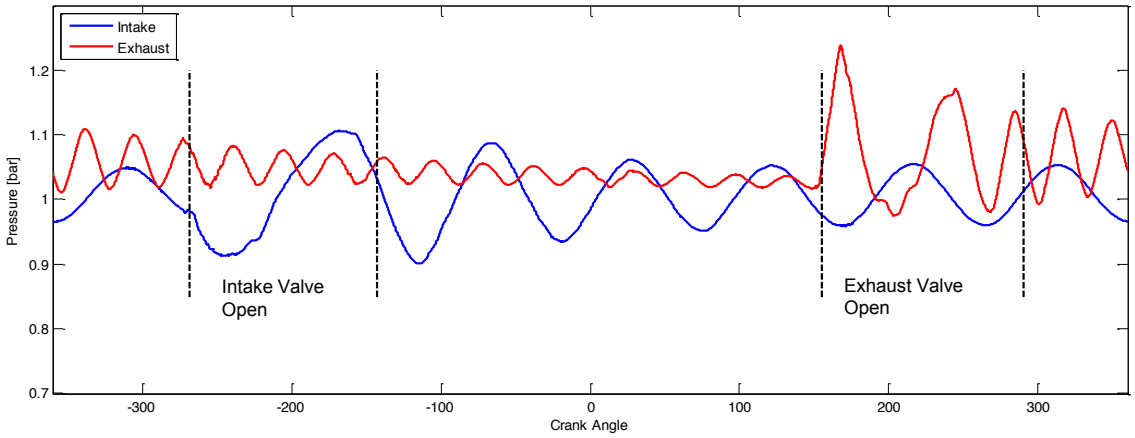

Figure 4.3 High speed manifold pressure measurements in the exhaust and intake manifolds, for SACI operation. The intake valve is open between the set of dashed lines on the left, while the exhaust valve is open between the pair on the right. Valve opening corresponds to the left line of each pair, while valve closure corresponds to the right. Pressure waves in the manifolds with peak to peak amplitudes of 0.2 bar are observed near the time of each valve closure.

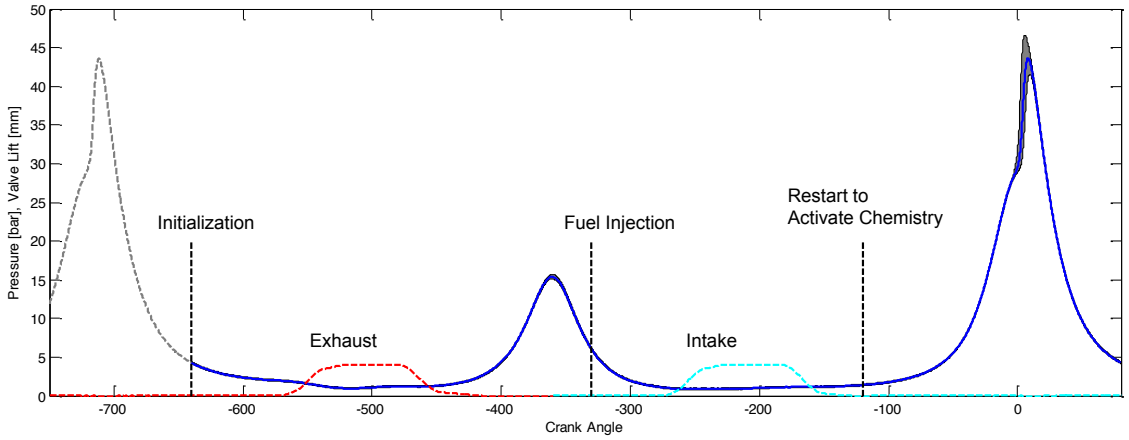

Figure 4.4 Common simulation configuration. Simulations are initialized prior to exhaust valve opening and run through the gas exchange and fuel injection process using a 5 species chemical mechanism with no reactions. Shortly after IVC at 120° bTDC the simulations are stopped and restarted with the 215 species isooctane mechanism of Tham et al. [124].

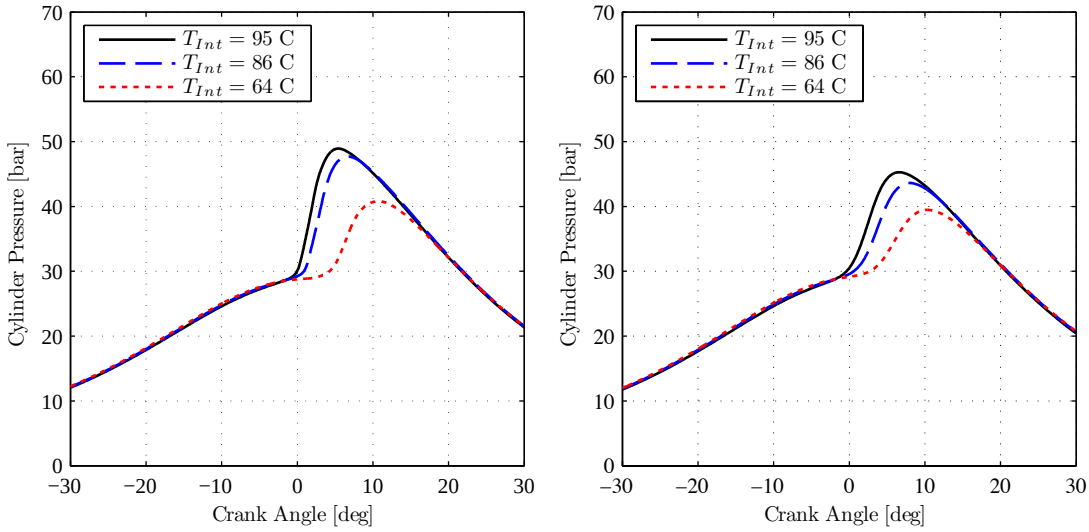

(a) Simulation Predictions

(b) Mean Experimental Cycles

Figure 4.5 Cylinder Pressure vs. Crank Angle for HCCI operation, for conditions described in Table 4.3. Model predictions 4.5(a) show good agreement with experimental data 4.5(b).

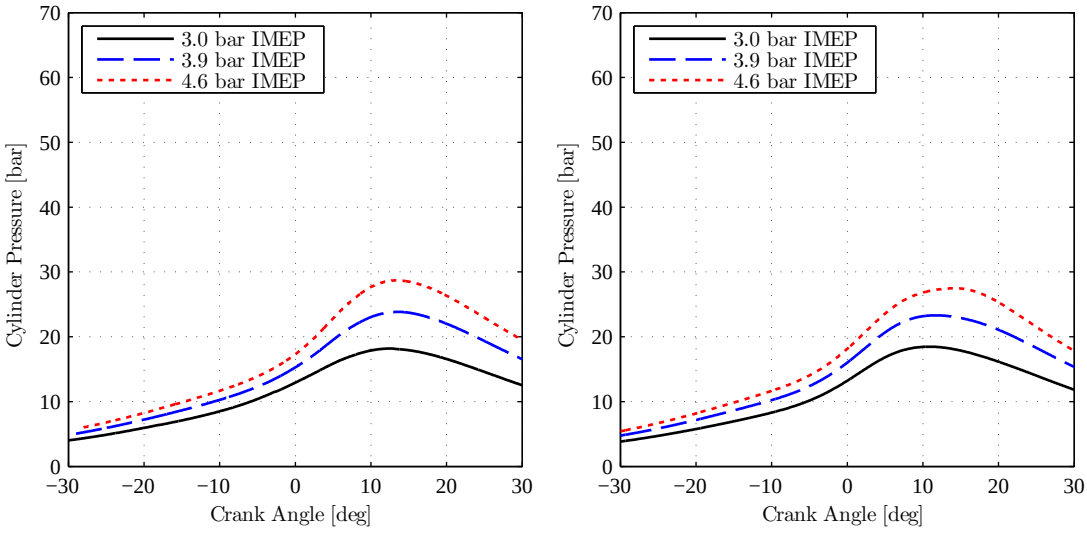

(a) Simulation Predictions (b) Mean Experimental Cycles

Figure 4.6 Cylinder Pressure vs. Crank Angle for SI operation, for conditions described in Table 4.4. Model predictions 4.6(a) show good agreement with experimental data 4.6(b).

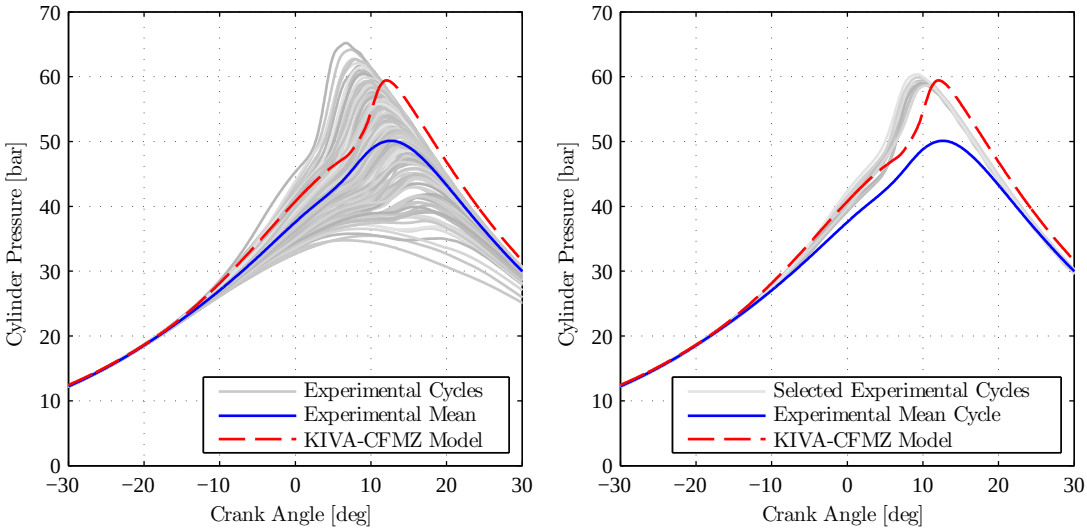

(a) All 200 Experimental Cycles (b) Select Experimental Cycles

Figure 4.7 Cylinder Pressure vs. Crank Angle for SACI operation. Complete 200 cycle experimental record shows large cycle to cycle variations 4.7(a), while a 10 cycle subset of the experimental data provides good agreement with the KIVA model predictions 4.7(b).

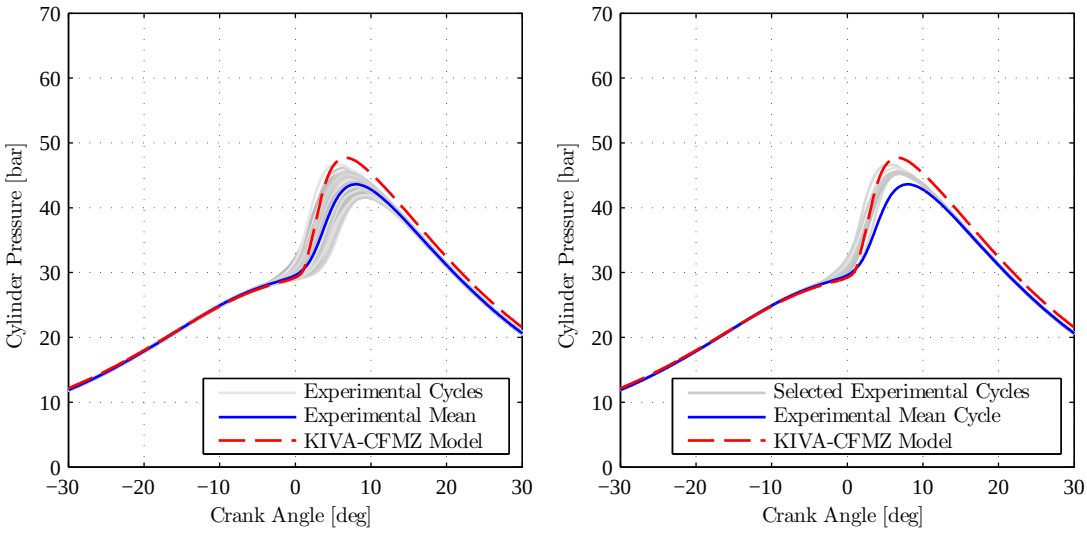

(a) All 200 Experimental Cycles

(b) Select Experimental Cycles

Figure 4.8 Cylinder Pressure vs. Crank Angle for HCCI operation. Complete 200 cycle experimental record shows similar cycle to cycle behavior 4.8(a), while a 10 cycle subset of the experimental data improves agreement between the model and experiment slightly 4.8(b).

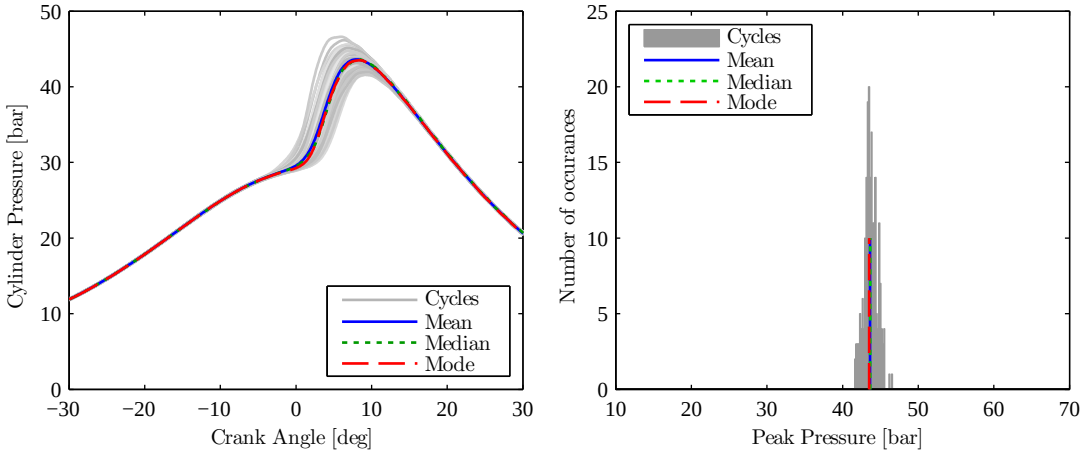

(a) HCCI Cylinder Pressure (b) Frequency

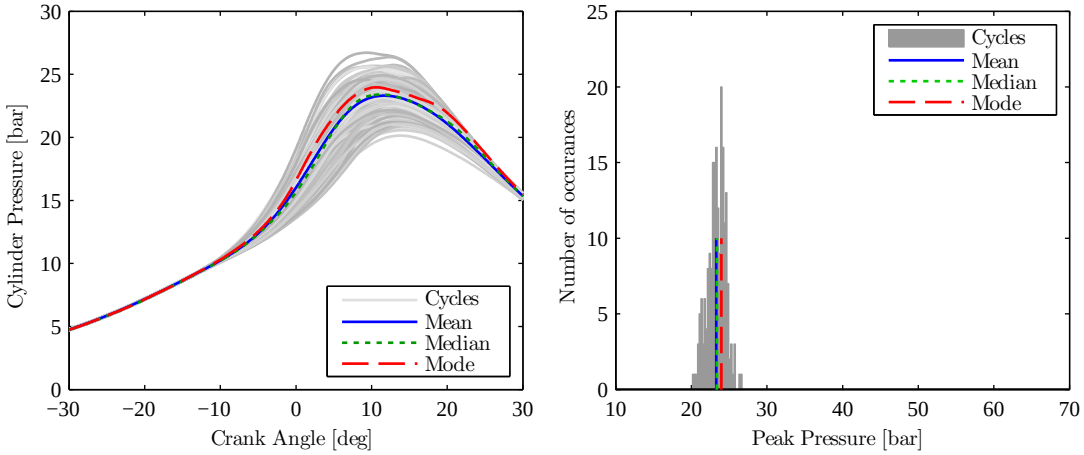

(c) SI Cylinder Pressure (d) Frequency

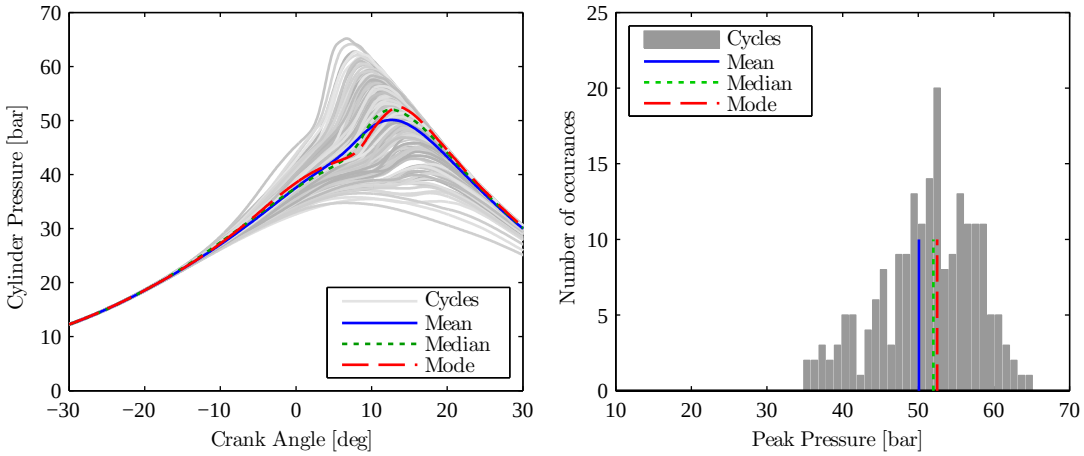

(e) SACI Cylinder Pressure (f) Frequency

Figure 4.9 Cycle to cycle variation in pressure data for HCCI, SI, and SACI combustion.

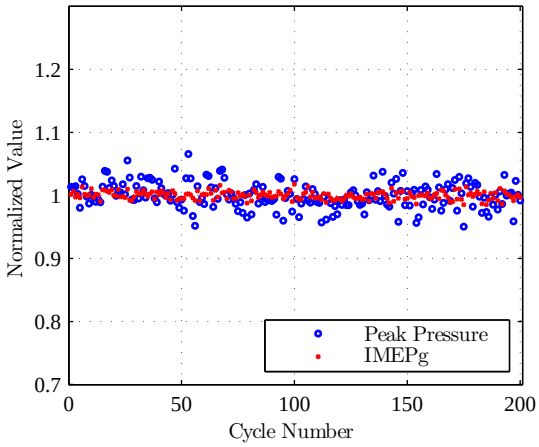

(a) HCCI CoV IMEP = 0.6%

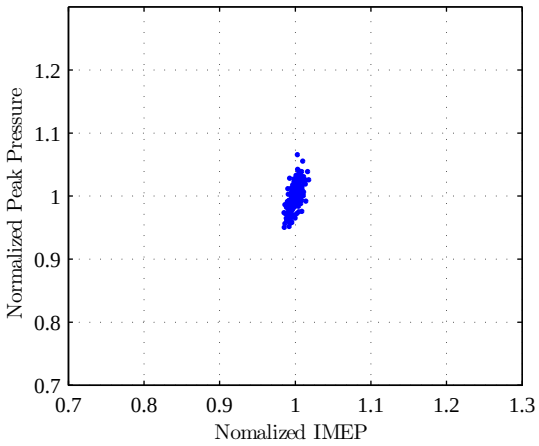

(b) HCCI CoV IMEP = 0.6%

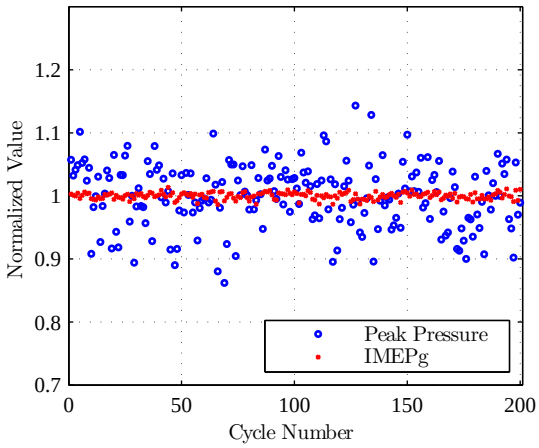

(c) SI CoV IMEP = 0.5%

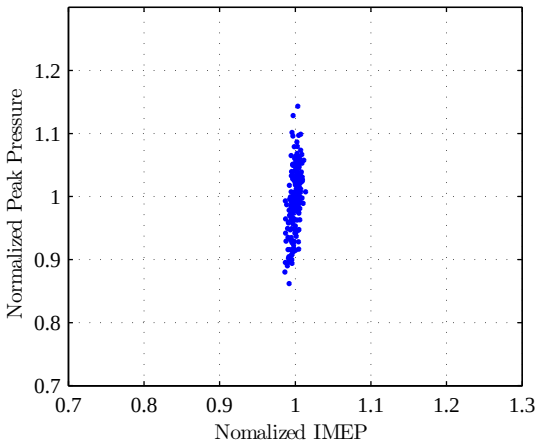

(d) SI CoV IMEP = 0.5%

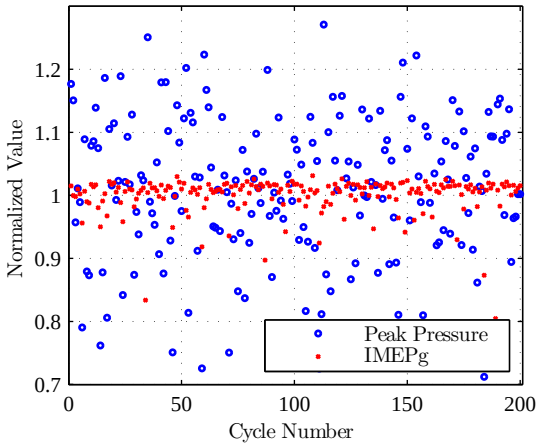

(e) SACI CoV IMEP = 2.9%

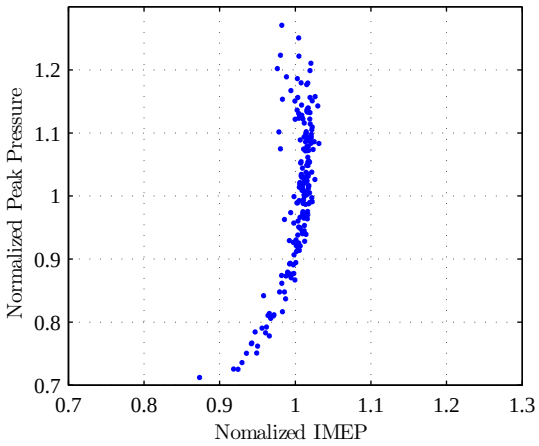

(f) SACI CoV IMEP = 2.9%

Figure 4.10 Variation in IMEP and peak pressure for HCCI, SI, and SACI.

Chapter 5

The Effect of Spark Timing and T_{IVC} on SACI Combustion

Recent experimental work has shown that the heat release rate of SACI combustion can be varied by controlling the relative contributions of the flame and auto-ignition combustion modes at constant combustion phasing [57, 67], where phasing is defined as the crank angle of 50% mass fraction burned (CA50). To adjust the balance between modes, the temperature at intake valve closing (T_{IVC}) and spark timing were adjusted simultaneously. For a given combustion phasing, a lower T_{IVC} required more spark advance (and associated flame compression of the end-gas) to achieve the end-gas temperature required for auto-ignition. Using this strategy the peak heat release rate was reduced by 40% with a 75% reduction in ringing intensity and 20% reduction in estimated end-gas mass at autoignition, without a significant reduction in thermal efficiency. While these studies demonstrated the potential of such strategies, the mechanism(s) affecting the peak heat release rates have not been identified or quantified. Such information will enable the development of SACI strategies to achieve a wider engine operating regime.

The primary objective of this chapter was to better identify the physical processes governing the behavior of SACI combustion at constant phasing as the fraction of flame and auto-ignition heat release are varied at constant composition. The previously described KIVA-CFMZ model was used to replicate the experimentally observed behavior of decreasing peak heat release rates with simultaneously increasing spark advance and decreasing T_{IVC}. Detailed analysis of the simulated end-gas states was performed to identify the factors responsible for the changes in the overall heat release rate. The results presented

in this chapter have been submitted for publication in the 35th Combustion Symposium [102].

5.1 Model Configuration

Open cycle KIVA-CFMZ simulations were configured based on the engine operating conditions of Olesky et al. [67], given in Table 5.1. All simulations followed the procedure described in detail in Chapter 4. The experiments were conducted with a constant intake temperature of 318 K, while the simulations required increasing intake temperature to maintain combustion phasing as spark timing was retarded. As indicated in Table 5.1, temperature adjustments of up to 15 K were applied to the model to adjust the phasing to match peak pressure location across simulations. As a result the predicted equivalence ratio at IVC also shifted by up to 1.6%, within the range of uncertainty in the experimentally reported values.

5.2 Comparison of KIVA Model Predictions with Experiments

Figure 5.1 presents a comparison of the in-cylinder pressure of the simulation results with selected cycles from the experimental data for the three spark timing/NVO/T_{IVC} conditions. Figure 5.1(b) shows 10 individual experimental cycles for each case, selected with peak pressures closest to those predicted by KIVA. Individual engine cycles were used for model assessment rather than the 'mean' ensemble averaged experimental pressure, as the 'mean' cycle fails to represent the exact experimental behavior, due to the significant cyclic variability under SACI operation, as discussed in Section 4.5. For both the model predictions and the experimental results, the cases with earlier spark advance and lower T_{IVC} have higher pressures at TDC compared to those with later spark at higher T_{IVC}. The model predictions of peak pressure and rate of pressure rise are consistent with behavior observed in the individual experimental cycles shown in Figure 5.1(b), with the predicted location of

peak pressure approximately 2° CA later than the experimental data.

Figure 5.2 presents the model results for the time histories for mass fraction burned and heat release rate for the three conditions in Table 5.1. The predicted mass fraction burned profiles were derived from the detailed accounting of each combustion mode available in KIVA. The overall mass fraction burned and the fraction due to flame front propagation are presented in Figure 5.2(a). The amount of burned mass produced by end-gas autoignition is omitted for clarity. The computations indicate a rapid transition from flame propagation, where the overall (solid line) and flame front (dashed line) data overlap, to auto-ignition. The results also show the flame contribution to the combustion process is minimal beyond end-gas thermal runaway, consistent with detailed flame simulations exhibiting a rapid transition from flame to auto-ignition combustion at the time of end-gas ignition [69]. The predicted mass fraction burned by the flame increases with increasing spark advance, from 27% to 50%, consistent with the experimentally reported decrease.

The heat release data (Figure 5.2(b)) show a significant decrease in the peak rate of heat release with increasing spark advance, consistent with the trends reported by Olesky et al. [67] for these conditions. Inflection points near 7° ATDC correspond to the transition from the low rates of heat releases associated with flame propagation to the higher rates associated with bulk auto-ignition of the end-gas. Advancing spark timing from 25° bTDC to 44° bTDC resulted in a 43% reduction in the peak rate of heat release. However, the reduction in the end-gas mass prior to auto-ignition was only 23%. Understanding the conditions in the end-gas responsible for the additional 20% reduction in heat release rate was the focus of the following analysis.

Figure 5.3(a) shows the model predictions of the mean end-gas temperature. The case with the most advanced spark timing and lowest T_{IVC} has the lowest unburned temperature at the time of spark, as well as the lowest temperature throughout the early stages of combustion. Additional flame propagation is associated with the lower T_{IVC} cases, and the simulation results show that approaching TDC, compression heating from the additional

flame propagation causes the predicted unburned temperatures to converge at approximately 1000 K. Consistent with the fixed CA50 requirement of the experiments, the three simulation cases follow a common mean temperature rise from 1000 K to 1050 K and the transition to the high rate of temperature change corresponds to the onset of end-gas auto-ignition. Dashed lines in the figure indicate the temperature predictions for simulations where the spark event was disabled and there is no flame propagation. The impact of compression heating from flame propagation is evident as the motored cases are up to 100 K colder at TDC and do not exceed 975 K. Model predictions of the laminar flame speed for the mean unburned gas state are presented in Figure 5.3(b). As the spark is advanced and unburned gas temperature decreased, the laminar flame speed decreases. The additional compression heating predicted for the 44° bTDC case relative to the 24° bTDC case is attributed to the additional time for the flame to propagate, wrinkle and grow.

Due to the direct injection fueling strategy used, there is potential for both compositional stratification as well as temperature stratification in the cylinder. To better understand the state of the end-gas just prior to auto-ignition, the model predictions were analyzed on a cell-by-cell basis. The cells were sorted into bins of similar thermodynamic conditions based on temperature and non-product equivalence ratio φ^* (defined in Section 3.2.2), then the mass in each bin was determined. Here φ^* is equivalent to the fuel to O_2 equivalence ratio when the end-gas reaction progress is zero.

Figure 5.4 shows the mass-temperature and mass-φ^* distributions of the end-gas at 5° aTDC, which is immediately prior to auto-ignition at 7° aTDC. The temperature distributions in Figure 5.4(a), generated with 5 K bins, show that the latest spark timing case exhibits notably higher masses on the high temperature side of the distribution, i.e. between 1050 K and 1125 K, as well as slightly higher masses on the low temperature side, i.e. below 1000 K, consistent with this case having the greatest total unburned mass at this crank angle. The leading edge of all three distributions is located at the same temperature, indicating that the start of auto-ignition for all three cases should occur at the same timing. Smaller differences

in the mass-temperature distributions are also observed between the earliest and middle spark timing cases. Compositional distributions in Figure 5.4(b), generated with 0.01 φ^* bins, show that the latest timing case also has more mass on the rich side of the distribution compared to the earlier timing cases.

Figure 5.5(a) presents the mass-temperature distributions at 5° aTDC for simulations with the spark event disabled. All three cases show self similar temperature distributions with longer tails on the cold side than on the hot side, offset from each other consistent with the differences in T_{IVC}. Corresponding mass-φ^* distributions are presented in Figure 5.5(b). The 24° bTDC case with a 0.028 higher mean Φ exhibits a shift in the φ^* distribution to higher values relative to the 44° bTDC case. The influence of flame propagation is assessed for a given T or φ^* bin by subtracting the motored distributions from the spark-on distributions, presented in Figure 5.6(a) for mass-temperature and Figure 5.6(b) for mass-φ^*. In these figures, positive values denote mass that exists at a particular state because of the influence of the flame, negative values denote mass that was shifted to another state by the presence of the flame or consumed by flame propagation. In Figure 5.6(a) the positive values between 1000 K and 1100 K indicate the effect of compression heating shifting the temperature distributions to higher temperature conditions. In Figure 5.6(b) there are no significant positive values, indicating that the flame is not altering the composition of the end-gas and is merely consuming mass. The symmetric distribution centered near $\varphi^* = 1.0$ indicates that flame propagation is preferentially consuming mass fastest at equivalence ratios nearest to stoichiometric, consistent with increased laminar flame speeds near $\varphi = 1.0$ reported in Chapter 2.

Figure 5.7 combines the results for thermal and compositional stratification from Figure 5.4 into one figure by plotting the difference between the mass-state distributions of the SA = 25° bTDC and 44° bTDC cases. The negative values are red and indicate the presence of more mass at a given T and φ^* in the SA = 25° bTDC case, while positive values are blue and indicate more mass in the SA = 44° bTDC case. The results show the

additional mass at high temperatures is co-located with the rich equivalence ratios in the late spark timing case. Higher temperatures and equivalence ratios will have lower ignition delays, as indicated in Figure 5.7 by dashed iso-lines calculated using the correlation of He et al. [74]. Similarly, higher temperatures and equivalence ratios closer to 1.1 will have higher laminar flame speeds, indicated in Figure 5.7 by dotted iso-lines calculated using the correlation of Chapter 2 [100]. These results suggest that advancing spark timing not only allows a larger fraction of the charge to be consumed by flame propagation, it also alters the distribution of thermodynamic states in the end gas remaining at auto-ignition toward conditions with lower reactivity.

Figure 5.8(a) shows the total rate of heat release due to end-gas auto-ignition decrease with increasing spark advance, consistent with the overall heat release rate trends presented in Figure 5.2(b). Normalizing the results of Figure 5.8(a) by the total end-gas mass undergoing auto-ignition gives the specific heat release rate of the end-gas, presented in Figure 5.8(b). The results show that the end-gas of the latest spark timing case has 20% higher specific heat release rate than the earliest spark timing case. Figure 5.9(a) shows the integrated mass above a given specific heat release rate, generated at 10° aTDC, which is in proximity to where the overall peak end-gas heat release rate occurs. The integration is performed by sorting the domain by the specific rate of heat release of each cell from high to low value, calculating the mass of the associated cell, and then summing the masses while moving from high to low specific rate of heat release. A higher value on the plot indicates a greater mass above a given specific heat release rate, while the cumulative mass at 0 specific rate of heat release is the total mass of the end-gas. Normalizing these integrals by the total end-gas mass yields the mass fraction integral presented in Figure 5.9(b). A higher value on this plot indicates a greater fraction of the end-gas mass at higher reaction rates, leading to the higher intensive heat release in Figure 5.8(b). These results indicate that both the overall mass remaining in the end-gas at auto-ignition (not consumed by flame propagation) as well as the thermal and compositional distribution of the end-gas contribute to the decrease in

peak heat release rate with advancing spark timing.

5.3 Summary

This Chapter investigated the variations in the peak rate of heat release observed at a constant phasing during SACI combustion when the fraction of flame and auto-ignition heat release were adjusted through changes in spark timing and T_{IVC}. Simulations conducted with the KIVA-CFMZ model successfully reproduced experimental trends, where the fraction of flame propagation increased as spark timing was advanced and T_{IVC} was decreased. The simulation predictions showed that in the earliest spark timing cases the larger difference between the end-gas temperature at the time of spark and the temperature required to initiate auto-ignition requires additional time for flame propagation and compression heating to achieve the end-gas auto-ignition temperature at a similar crank angle.

While some of the reduction in the end-gas rate of heat release was associated with the reduced end-gas mass available for auto-ignition as the flame consumed more of the charge, the specific end-gas heat release rates also differed between the predicted cases. Detailed analysis of the end-gas state prior to auto-ignition showed that not only did the total end-gas mass decrease as spark timing advanced, but that the thermal and equivalence ratio distributions also shifted to lower peak values. This shift leads to a reduction in the specific energy release rate at the early spark timing, which has less mass in regions of high heat release rate. The observed reduction in overall heat release rate with increasing spark advance therefore results from the reduction in end-gas mass available at auto-ignition, as well as a shift in the distribution of temperatures and equivalence ratios toward lower reactivities.

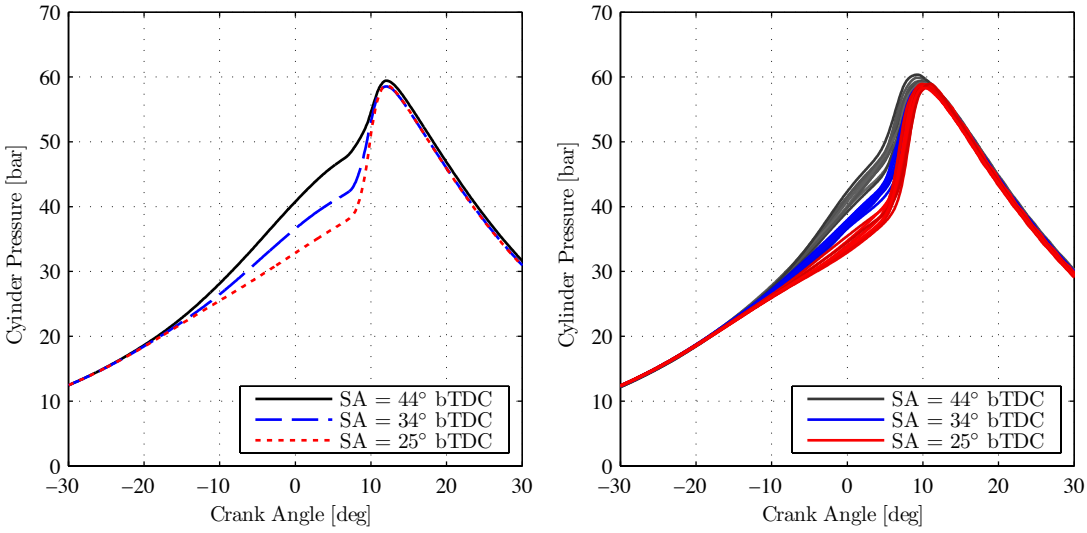

(a) Simulation Predictions (b) Select Experimental Cycles

Figure 5.1 Cylinder Pressure vs. Crank Angle for SACI operation, where spark advance and NVO duration are simultaneously adjusted to maintain constant combustion phasing (CA50).

Table 5.1 SACI operating conditions studied, 6 mm valve lifts at 2000 rpm.

Spark Timing °bTDC	NVO °CA	Φ Exp	Φ Model	Internal EGR [%]	External EGR [%]	Total EGR [%]	T_{intake} Model [K]
44	114	0.96	0.968	22.8	17.0	39.8	318
34	128	0.97	0.966	25.5	14.4	39.9	326
25	136	0.98	0.996	27.4	11.9	39.3	333

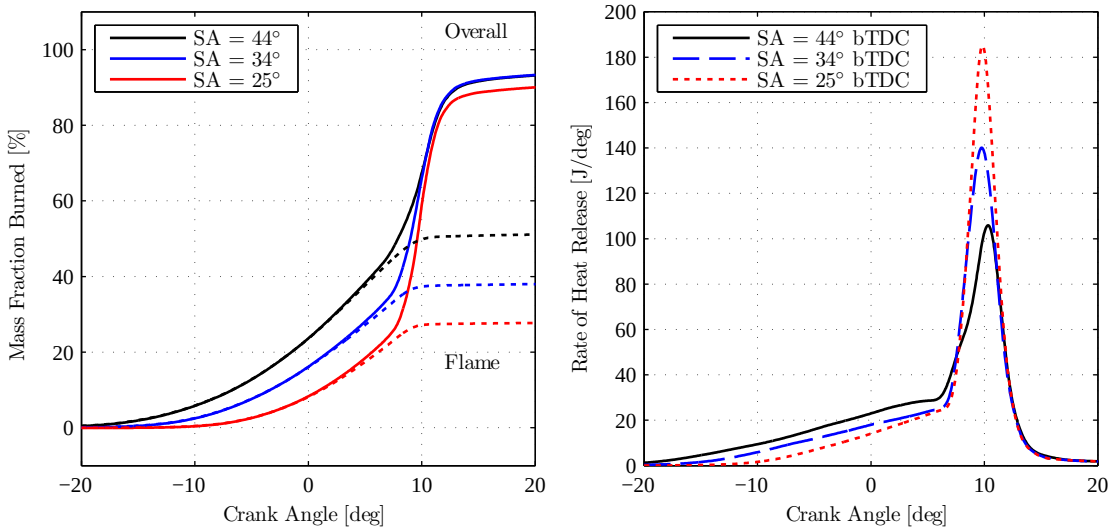

(a) Mass Fraction Burned (b) Rate of Heat Release

Figure 5.2 Model predicted mass fraction burned profiles, which shows that advancing spark timing from 25° bTDC to 44°bTDC increases the fraction of flame based heat release 5.2(a) and reduces the peak rate of heat release by 43% 5.2(b).

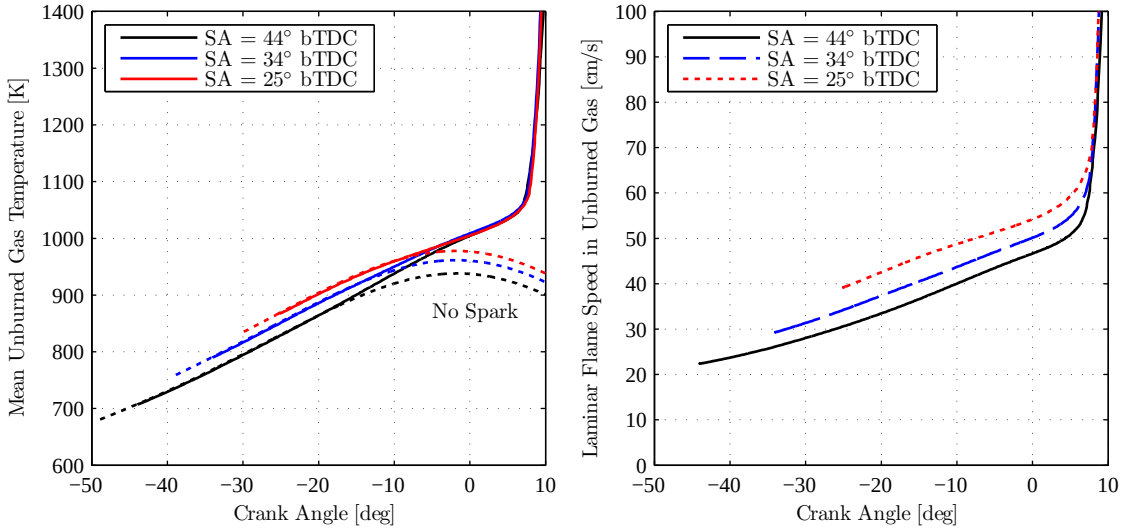

(a) Unburned Temperature (b) Laminar Flame Speed

Figure 5.3 Model predicted mean unburned gas temperatures in 5.3(a) are initially lower for cases with the greatest spark advance, converging toward a common path prior to the onset of end-gas auto-ignition. Simulations with the spark event disabled are denoted by dashed lines and indicate the impact of compression heating on the unburned gas temperature. Predicted laminar flame speeds in 5.3(b) show conditions with lower unburned gas temperatures exhibiting lower flame speeds.

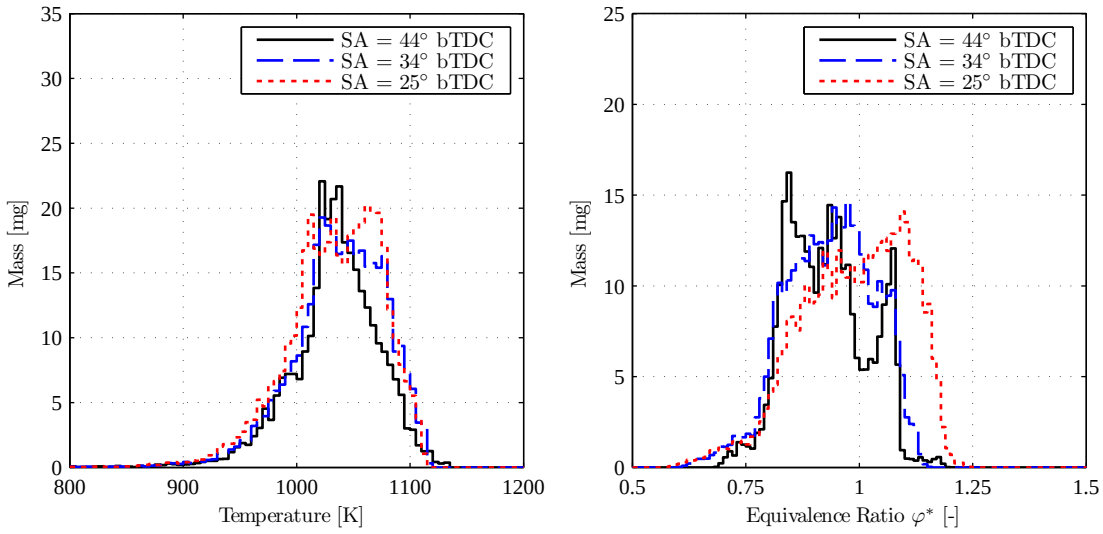

(a) Temperature (b) Composition

Figure 5.4 Unburned gas state distributions at 5° aTDC, immediately prior to autoignition. Figure 5.4(a) generated with 5 K temperature bins, Figure 5.4(b) with 0.01 φ^* bins. The 25° bTDC timing case with the highest peak rate of heat release has more mass at high temperatures and rich equivalence ratios than the earlier timing cases.

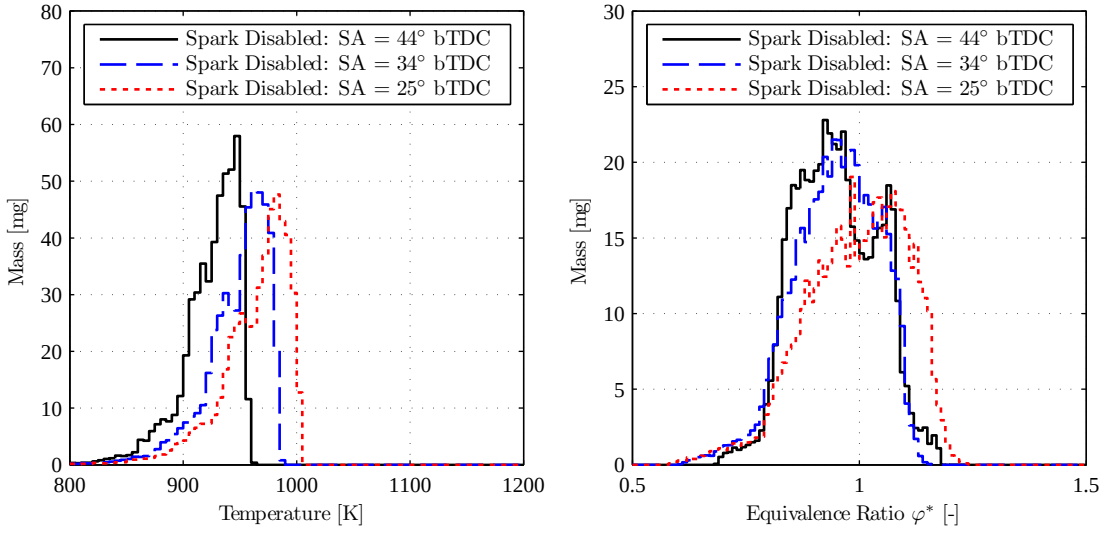

(a) Motored Temperature (b) Motored Composition

Figure 5.5 Unburned gas state distributions 5° aTDC for motored conditions with the spark event disabled, mass-temperature 5.5(a) and mass-φ^* 5.5(b).

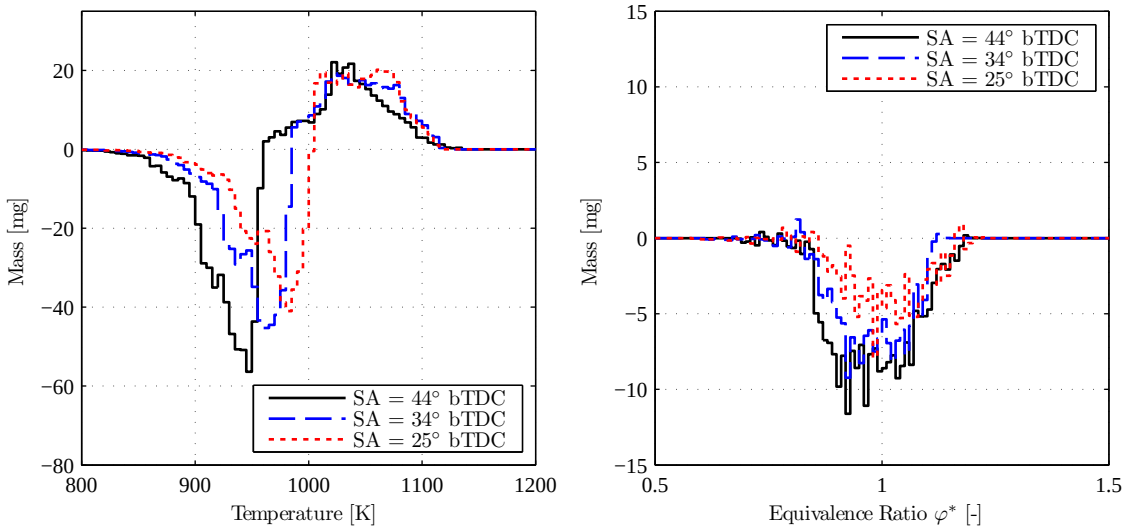

(a) T Difference: Flame - Motored

(b) φ^* Difference: Flame - Motored

Figure 5.6 Difference in unburned gas state distribution between the spark-active and motored simulations. Mass-temperature in 5.6(a) and mass-φ^* in 5.6(b), indicating the influence of flame propagation on the end-gas state prior to auto-ignition.

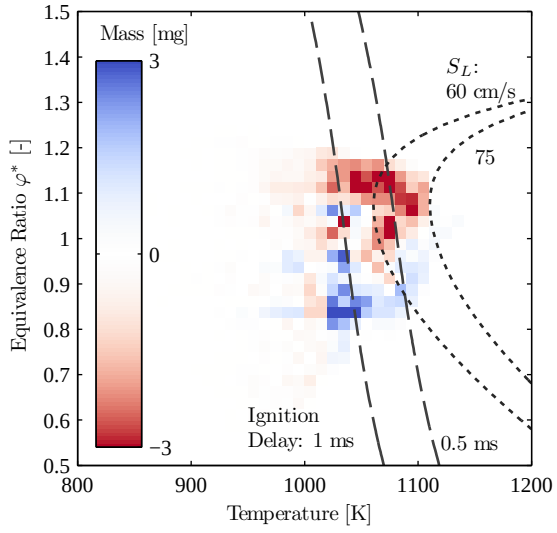

Figure 5.7 Difference between the unburned gas state distributions for the 44° bTDC and 25° bTDC cases at 5° aTDC, immediately prior to autoignition. Generated with 10 K temperature bins, and 0.025 φ^* bins. Red/negative values indicate more mass in the 25° bTDC case. The 25° bTDC timing case with the highest peak rate of heat release has more mass at high temperatures and rich equivalence ratios than the earlier timing cases, corresponding to lower ignition delay and higher S_L.

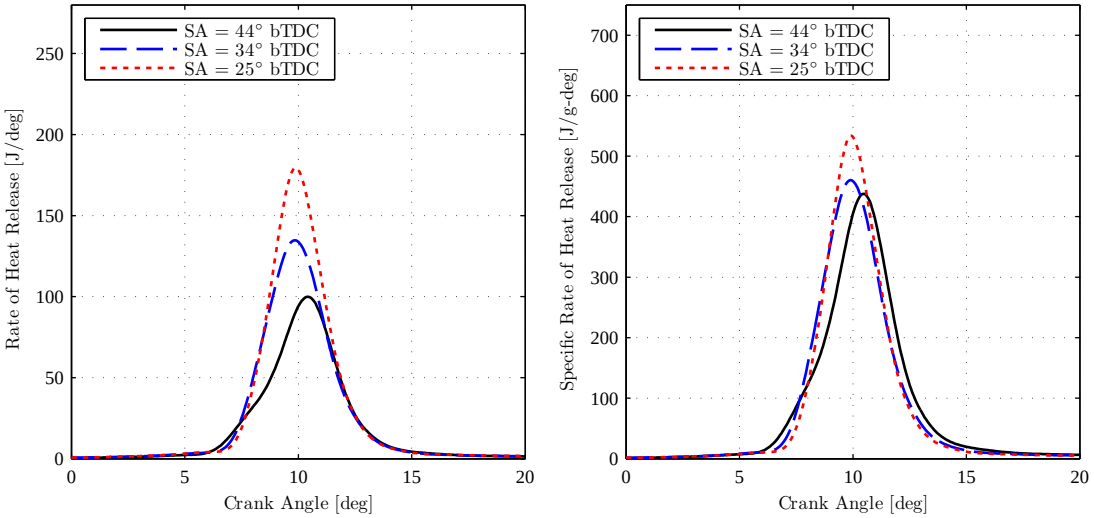

(a) Extensive (b) Intensive

Figure 5.8 End gas contribution to the overall heat release rate shows decreasing heat release with increasing spark advance, on both an overall 5.8(a) and a per mass 5.8(b) basis.

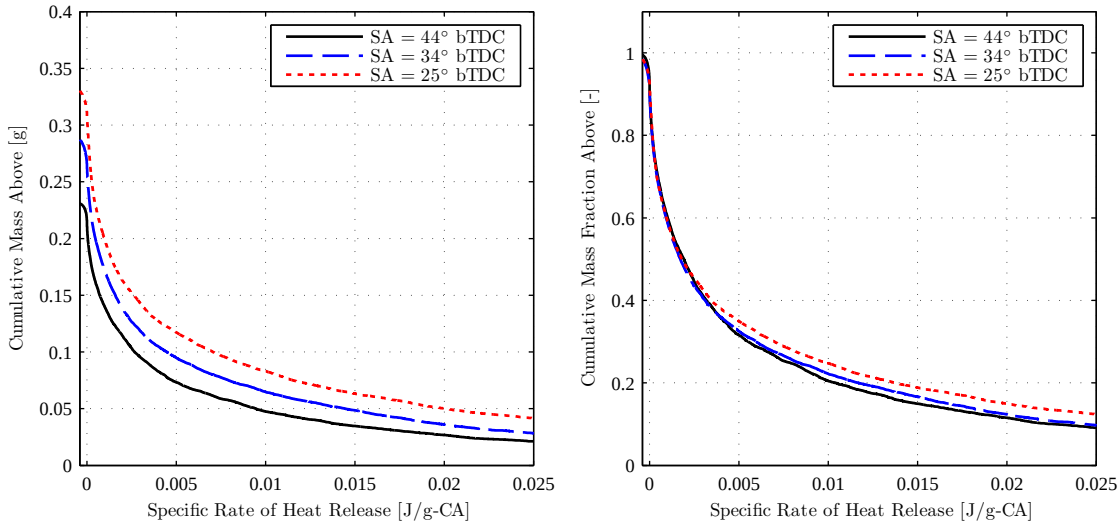

(a) Integral (b) Fraction

Figure 5.9 At the time of the peak heat release rate, the latest spark timing case has more total mass at high heat release rates than the earlier timing cases 5.9(a), as well as a higher fraction of end-gas mass at higher heat release rates 5.9(b).

Chapter 6

The Effect of Diluent Oxygen Concentration on SACI Combustion

Recent experimental work has shown that the heat release rate of SACI combustion can be varied by controlling the diluent composition in the mixture at constant combustion phasing [48], where phasing is defined as the crank angle of 50% mass fraction burned (CA50). To shift the balance between the relative contributions of the flame propagation auto-ignition combustion modes, the fraction of EGR in the intake manifold and intake temperature were simultaneously adjusted. As the EGR fraction is reduced the mixture O_2 fraction increases, while the intake temperature required to maintain constant combustion phasing decreases. Using this strategy, the early heat release attributed to flames increased with increasing O_2 fraction, while the peak rate of heat release decreased by 25%. An observed increase in thermal efficiency of 4% (relative), was offset by a significant increase in engine out NO_X of 260%, exceeding the 1g/kg-fuel threshold requiring NO_X aftertreatment.

The objective of this chapter was to better understand the physical processes governing the behavior of SACI combustion at constant phasing as the mixture O_2 concentration and temperature were varied. To establish confidence in the KIVA-CFMZ model's capability to capture trends related to O_2 concentration, simulations of HCCI combustion with varying O_2 concentration and T_{IVC} were conducted and compared to experimental results. The KIVA-CFMZ model was then used to replicate the experimentally observed SACI combustion behavior of decreasing peak heat release rates with simultaneously increasing O_2 concentration and decreasing T_{IVC}. Analysis of the detailed end-gas states was performed to identify the factors influencing the overall heat release rate.

6.1 Model Configuration

Open cycle KIVA simulations were configured based on the engine operating conditions of Olesky et al. [48], given in Table 6.1 for HCCI operation and Table 6.2 for SACI operation. All simulations followed the procedure described in detail in Chapter 4. For each set of conditions, the fraction of external EGR in the intake was adjusted while maintaing fueling, affecting a change in the charge equivalence ratio (Φ) and O_2 concentration. Simulation intake manifold temperatures were adjusted to match combustion phasing between the model predictions. As indicated in the first three lines of Table 6.1, the HCCI simulations at constant intake temperature required a constant T_{intake} increase of 10 K, consistent with the previously presented HCCI simulations at constant equivalence ratio in Section 4.3. For HCCI conditions where equivalence ratio and intake temperature were simultaneously varied to maintain combustion phasing (last three lines of Table 6.1), a variable intake temperature adjustment ranging from 0 K for the highest equivalence ratio case to +25 K for the lowest equivalence ratio case was required. The SACI conditions required a similar set of variable T_{intake} adjustments (Table 6.2), where the highest equivalence ratio case required a reduction of 10 K and the lowest equivalence ratio case an increase of 31 K. Due to the large residual fractions present under these operating conditions, for every 10 K T_{intake} adjustment an approximately 6 K change in T_{IVC} was observed. With these T_{intake} adjustments the range of T_{IVC} values in the simulations agree with the trend and range observed in the experimentally estimated conditions, with a constant +22 K offset for all SACI simulations relative to the experiments. This change is consistent with experimentally observed differences between isooctane and gasoline for HCCI combustion, where Dec reported that isooctane required intake temperatures $\approx$20 K hotter than gasoline to maintain constant combustion phasing in an 18:1 compression ratio engine without large internal residual fractions [176]. Adjustments to T_{intake} are one method of compensating for uncertainties in the simulation initial conditions and charge preparation during the open portion of the cycle. Other methods could be used to achieve a similar IVC state, such as manipulations to the initial temperature estimate at

the start of the simulation or adjustments to the exhaust boundary pressure and resulting trapped mass during NVO.

6.2 Comparison of KIVA Model Predictions with Experiments

6.2.1 HCCI Sensitivity to Compositional Changes

Figure 6.1 shows a comparison between the in-cylinder pressure predicted by the KIVA-CFMZ model and the reported experimental data for the first three conditions listed in Table 6.1. For both the model and the experiment, increasing molar O_2 concentration from 9.0% to 10.7% at constant intake temperature advanced combustion phasing by approximately 8° crank angle. The model results show excellent trend-wise agreement with the experiments, while predicting slightly higher peak pressures and pressure rise rates relative to the experiment, similar to simulations at constant composition reported in Chapter 4.

Figure 6.2 presents the simulation results and experimentally reported data for the last three conditions listed in Table 6.1. Both the model and the experiments show very similar pressure rise rates and peak pressures when intake temperature is adjusted simultaneously with equivalence ratio to maintain constant combustion phasing. The model once again predicts peak pressures slightly higher than the experimental mean, along with higher pressure rise rates. However, the trend-wise behavior of nearly constant pressure rise rate at constant phasing independent of charge O_2 concentration is well captured.

Model predictions of the mean unburned gas temperature prior to auto-ignition for both HCCI studies are presented in Figure 6.3. Conditions with constant T_{intake} in Figure 6.3(a) show no difference in temperature with changing O_2 concentration until approximately 5° bTDC. At this time temperature predictions begin to diverge as conditions with higher O_2 auto-ignite before conditions with lower O_2. This is consistent with the well established

influence of reactant concentration on chemical reaction rates, leading to the inclusion of O_2 concentration terms in published ignition delay correlations such as He et al. [74]. When intake temperature is adjusted to hold combustion phasing constant in Figure 6.3(b), conditions with higher O_2 concentrations require lower temperatures to initiate end-gas auto-ignition, with an approximately 30 K increase in T_u at TDC required to compensate for a 6.2% decrease in O_2.

The KIVA-CFMZ model predictions agree well with experimentally reported trends in HCCI combustion as diluent composition and mixture O_2 concentration are varied. These results provide confidence in the model's ability to replicate the auto-ignition portion of SACI combustion under conditions with varying O_2 concentration.

6.2.2 SACI Sensitivity to Compositional Changes

Figure 6.4 shows a comparison of the in-cylinder pressure predictions from the simulation with selected cycles from the experimental data for the three EGR/O_2/T_{IVC} conditions in Table 6.2. Figure 6.4(b) shows 10 individual experimental cycles for each case, selected for constant location of peak pressure for all cases. This location of peak pressure was chosen based on the experimental cycles that most closely agreed with the magnitude of peak pressure predicted by KIVA for the Phi = 0.90 operating condition. For both the experimental results and the model predictions, the cases with the lowest equivalence ratio and highest O_2 concentration exhibit higher pressures immediately after TDC compared to more EGR dilute conditions with lower O_2 concentrations. The differences between the cases are subtle, with cycle to cycle variability even within a small set of 10 experimental cycles obscuring most of the differences. Figure 6.4(c) more clearly illustrates the trendwise behavior with varying O_2 concentration by plotting the mean of the 10 selected cycles for each condition. The model predictions of peak pressure and rate of pressure rise agree well with the selected individual experimental cycles, with the predicted location of peak pressure approximately 2° CA later than the experimental data, consistent with the SACI simulations

discussed in Chapter 5.

Figure 6.5 presents the model predictions for the crank angle histories of mass fraction burned and rate of heat release for the three EGR/O_2/T_{IVC} conditions. The overall mass fraction burned and the fraction due to flame propagation are presented in Figure 6.5(a), with the contribution of end-gas auto-ignition omitted for clarity. The model predicts a rapid transition from flame propagation, where the overall and flame front data overlap, to auto-ignition, with minimal flame contribution beyond end-gas thermal runaway for all conditions modeled, independent of O_2 concentration. As the O_2 concentration in the mixture increases, the predicted mass fraction burned by the flame also increases from 23.7% to 33.6%. Predicted heat release rates in Figure 6.5(b) show slightly higher rates with increasing O_2 concentration during the early flame propagation phase, leading to a 10% reduction in peak rate during auto-ignition. While this is a smaller reduction than the experimentally reported 25%, it is trend-wise consistent with the experimental behavior and consistent with the 10% change in mass burned by the flame (relative to the total mass). Some of the discrepancy between the magnitude of the experimentally reported trends and the model predictions can be attributed to the use of the ensemble average pressure in the experimental analysis. Inflection points in the curves near 8° aTDC indicate the transition from flame propagation with low rates of heat release to end-gas auto-ignition with significantly higher heat release rates, occurring at the same crank angle location for all of the cases studied.

Model predictions of the mean end-gas temperature between the time of spark and auto-ignition are presented in Figure 6.6. The most EGR dilute case with the lowest O_2 concentration and the highest T_{IVC} also has the highest unburned temperature at the time of spark, and throughout the combustion process, as seen in Figure 6.6(a). As the simulations approach 5° aTDC the increased flame based heat release associated with the higher O_2 cases provides additional compression heating and reduces the temperature difference between the cases. However, as shown in Figure 6.6(b), the mean unburned temperatures do not converge

to a common value prior to auto-ignition. The 11.9% O_2 case requires mean temperatures approximately 20 K higher than the 17.1% O_2 case to initiate end-gas auto-ignition at 8° aTDC.

The contribution of flame propagation during the early stage of SACI combustion is governed by the growth of the flame kernel, which is in turn dependent on the laminar flame speed of the mixture and the turbulent wrinkling affecting the flame [88, 135]. Under the conditions studied, with constant valve timing and engine speed, the turbulent intensity and length scale predicted by the KIVA model were approximately constant between cases. Figure 6.7 shows the predicted laminar flame speeds for the mean unburned gas conditions as mixture O_2 concentration varies. Flame speeds are predicted to increase with increasing O_2 concentration, despite the corresponding decrease in unburned gas temperature. This is consistent with the discussion in Chapter 2 where the laminar flame property correlations used in the KIVA model were developed.

To investigate the potential thermal and compositional stratification in the unburned gas due to the direct fuel injection used, the model predictions of the end-gas state just prior to auto-ignition were analyzed on a cell by cell basis. The cells were sorted into bins of similar thermodynamic conditions and the mass in each bin was determined. Figure 6.8 shows the mass-state distributions in the end-gas at 5° aTDC, prior to the onset of end-gas auto-ignition at 8° aTDC. The mass-temperature distributions in Figure 6.8(a) show that all three conditions have very similar temperature distributions below 1050 K. On the hot side of the distribution near 1100 K, the 11.9% O_2 case with the highest mean unburned gas temperature also has the most mass, indicating that the higher mean temperature is due to the contribution of the hottest portion of the charge. Figure 6.8(b) shows the mass-φ^* distributions (where φ^* is defined in Section 3.2.2 and is analogous to the fuel to O_2 equivalence ratio) also at 5° aTDC. As the mean Φ of the mixture drops and O_2 concentration increases the distributions shift to lower φ^*, as well as into narrower distributions with higher peaks.

Figure 6.9 combines the results for the thermal and compositional stratification together

for the 11.9% O_2 case 6.9(a) and the 17.1% O_2 case 6.9(b). Both distributions are nearly symmetrical with respect to φ^*, with the 11.9% O_2 case exhibiting a slightly wider distribution toward low equivalence ratios near 1000 K. There is no strong correlation predicted between temperature and equivalence ratio for these conditions, with only a slight bias toward higher equivalence ratios at the highest temperatures in the upper right hand corner of each distribution. Some level of positive correlation is expected when injecting fuel into the residual gas during NVO, as noted by Kodavasal [16].

Model predictions of the end-gas rate of heat release are presented in Figure 6.10, on an overall basis in 6.10(a) and on a per end-gas mass basis in 6.10(b). These values are generated by differentiating the model predictions of mass fraction burned, using a method consistent with experimental heat release analysis. As O_2 concentration is increased from 11.9% to 17.1%, the model predicts an 8.3% reduction in overall end-gas heat release rate, with a 4.4% increase in the heat release per unit unburned mass. However, more detailed analysis of the model predictions provides further insight into this behavior. Figure 6.11 presents the rate of end-gas heat release calculated by summing the energy released in every CFD cell during each timestep. The overall heat release rates in Figure 6.11(a) show a trend consistent with the smooth heat release curves from differentiation in Figure 6.10(a), but includes significant timestep to timestep noise in the predicted heat release rate. The per unit unburned mass predictions in Figure 6.11(b) show that the previously calculated 4.4% increase in heat release rate is within the timestep to timestep accuracy of the KIVA model predictions; the uncertainty in calculation prevents the model from identifying the cases of such a small change in the peak rate of heat release. These results indicate that the observed decrease in the overall heat release rate with increasing mixture O_2 concentration is due primarily to a decrease in the end-gas mass present at auto-ignition.

Simulation work by Kodavasal [16] reported that HCCI burn durations were significantly more sensitive to changes in temperature stratification than to compositional stratification at the same mean equivalence ratio. Those results provide insight into the mass-temperature

distributions in Figure 6.8(a) and the resulting end-gas heat release rates in Figure 6.11. The figures suggest that the differences predicted in the overall peak heat release rate is due to the additional mass present on the high temperature side of the mass-temperature distribution, while the similar peak heat release rates on a per end-gas mass basis are a result of the similar temperature distributions below 1050 K controlling the rate of cascading auto-ignition.

6.3 Summary

This Chapter investigated variations in SACI combustion behavior at constant combustion phasing and constant spark timing as the intake EGR fraction was replaced with fresh air and the resulting mixture O_2 concentration varied. Simulations conducted with the KIVA-CFMZ model successfully reproduced the experimentally reported trends, where the fraction of flame propagation increased as the O_2 concentration in the mixture increased and T_{IVC} decreased. The simulation predictions for both HCCI and SACI operation showed that mixtures with higher O_2 concentrations required lower unburned gas temperatures to initiate end-gas auto-ignition at a similar crank angle.

The peak rate of heat release decreased by 10% as O_2 concentration increased from 11.9% to 17.1% and the mass fraction burned by the flame increased from 23.7% to 33.6%. Detailed analysis of the end-gas state prior to auto-ignition showed negligible differences in thermal stratification below 1050 K for all three cases, with the lowest O_2 conditions having more mass at the highest temperatures near 1100 K. The heat release rate per unit mass of end-gas undergoing auto-ignition was predicted to be insensitive to the O_2 concentration. As a result, the observed reduction in overall peak heat release rate is attributed to reductions in the unburned mass at the time of auto-ignition.

Table 6.1 HCCI operating conditions studied, constant fueling of 13.4 mg/cycle resulting in 4.2 - 4.4 bar $IMEP_g$ at 2000 rpm with 4 mm valve lifts.

Φ Exp.	Φ Model	φ Model	Model O_2 [mole %]	$EGR_{internal}$ Exp. [%]	$EGR_{external}$ Exp. [%]	NVO [° CA]	T_{intake} Exp. [K]	T_{intake} Model [K]
0.97	0.98	0.95	9.0	48	12	172	318	328
0.92	0.93	0.86	10.0	49	10	172	318	328
0.89	0.89	0.80	10.7	48	9	172	317	327
0.94	0.94	0.88	9.5	41	18	153	394	394
0.79	0.80	0.68	12.5	40	12	153	357	369
0.61	0.64	0.52	15.7	40	0	153	318	343

Table 6.2 SACI operating conditions studied, at 2000 rpm with 100° NVO duration and 23% internal EGR, 6 mm valve lifts, and 32° bTDC spark timing. Constant fueling of 17.5 mg/cycle resulting in 6.2 - 6.4 bar $IMEP_g$.

Φ Exp.	Φ Model	φ Model	Model O_2 [mole %]	$EGR_{external}$ Exp. [%]	T_{intake} Exp. [K]	T_{intake} Model [K]	T_{IVC} Exp. [K]	T_{IVC} Model [K]
0.97	0.95	0.92	11.9	21	405	395	479	501
0.90	0.90	0.84	13.0	18	371	381	472	494
0.67	0.69	0.63	17.1	5	329	360	452	472

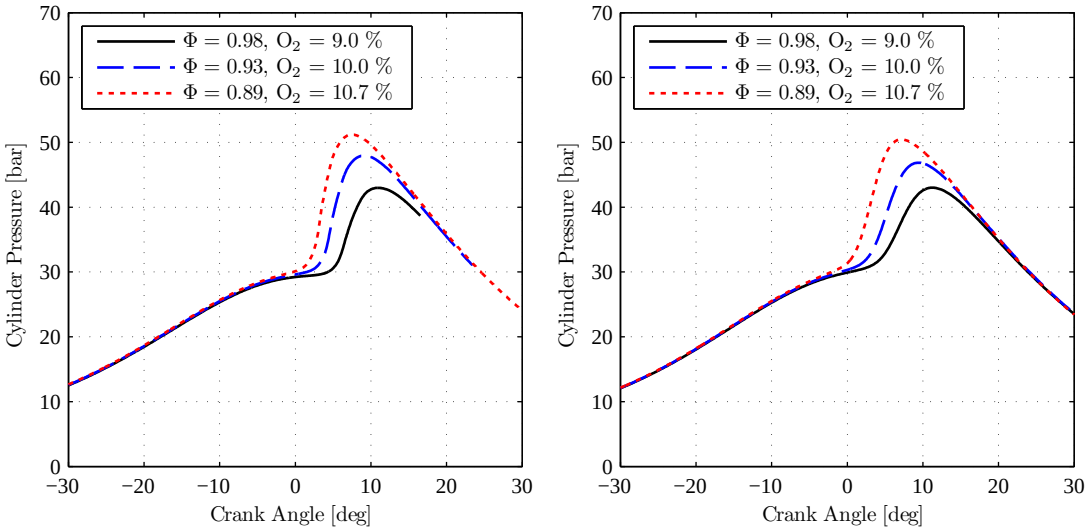

(a) Simulation Predictions (b) Mean Experimental Cycles

Figure 6.1 Cylinder Pressure vs. Crank Angle for HCCI operation, where diluent composition is varied at constant fueling and intake temperature.

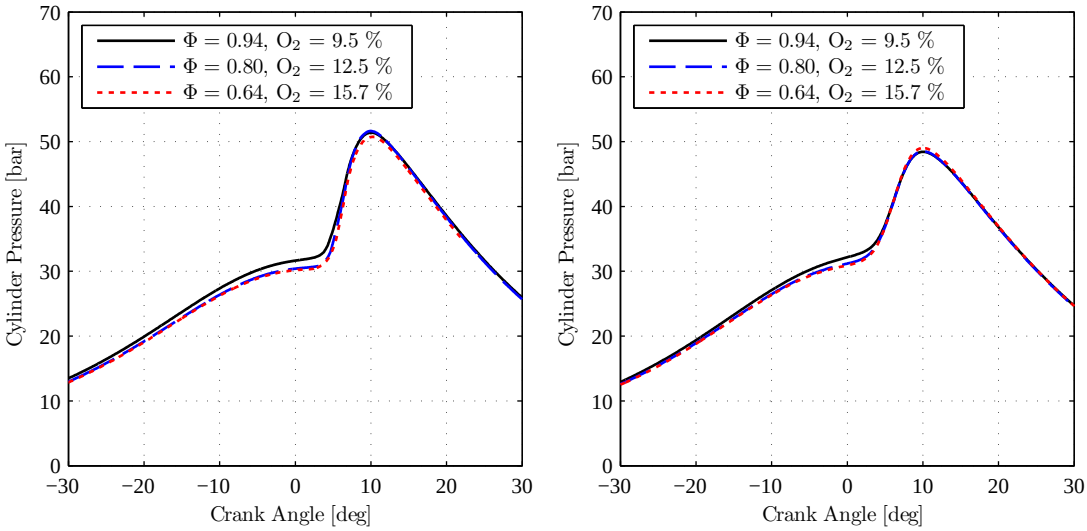

(a) Simulation Predictions (b) Mean Experiment Cycles

Figure 6.2 Cylinder Pressure vs. Crank Angle for HCCI operation, where diluent composition and intake temperature are simultaneously varied to maintain constant combustion phasing (CA50).

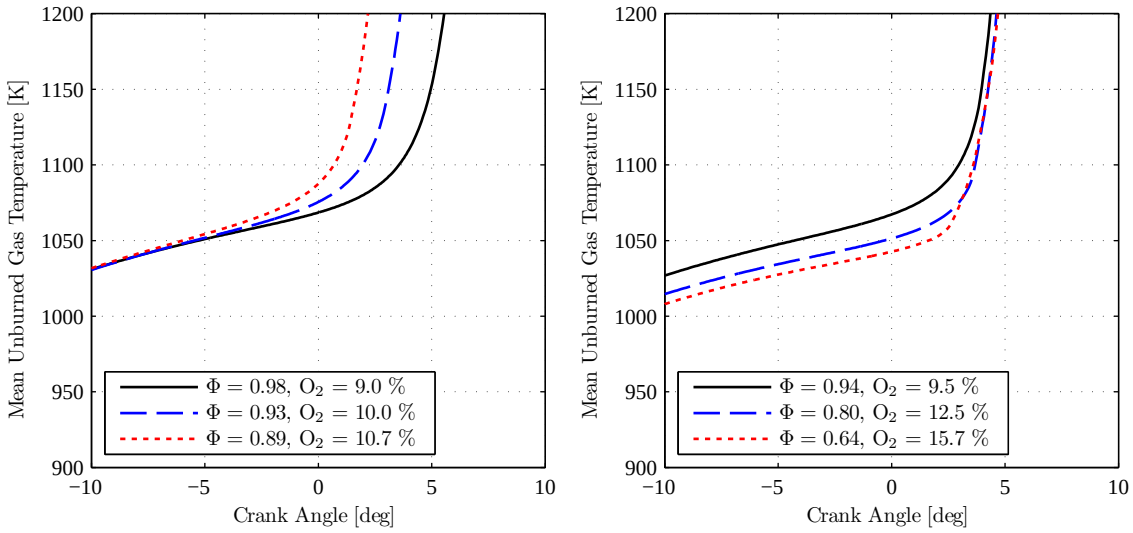

(a) Constant T_{IVC} (b) Constant CA50

Figure 6.3 Model predictions of mean unburned gas temperatures for HCCI operation as diluent composition varies. For constant T_{intake} in 6.3(a), the end of compression temperatures immediately prior to auto-ignition are constant for all three cases. At constant phasing in 6.3(b) conditions with higher O_2 require lower temperatures to initiate end-gas auto-ignition, by approximately 30 K for a 0.33 reduction in Φ.

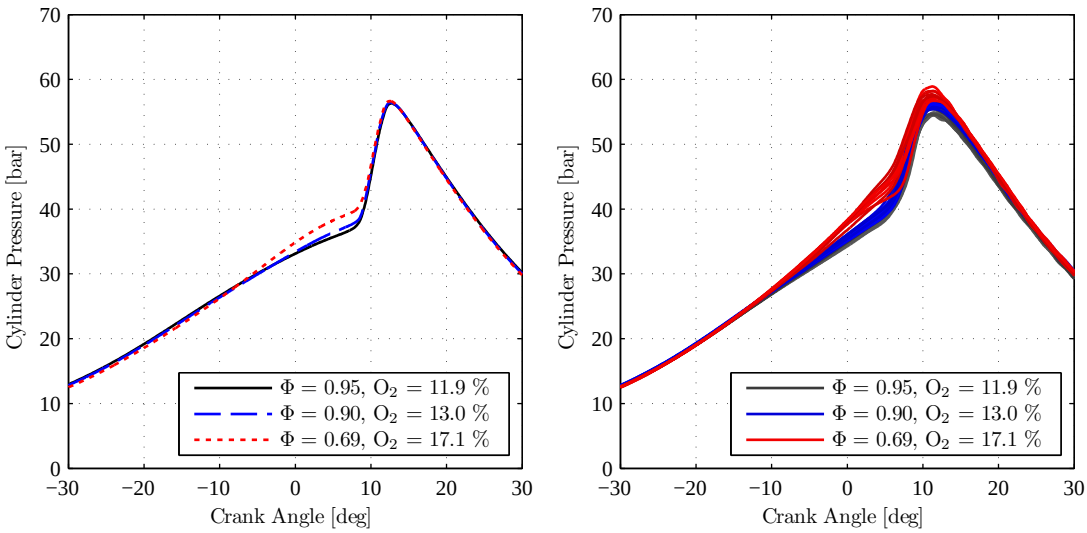

(a) Simulation Predictions

(b) Select Experimental Cycles

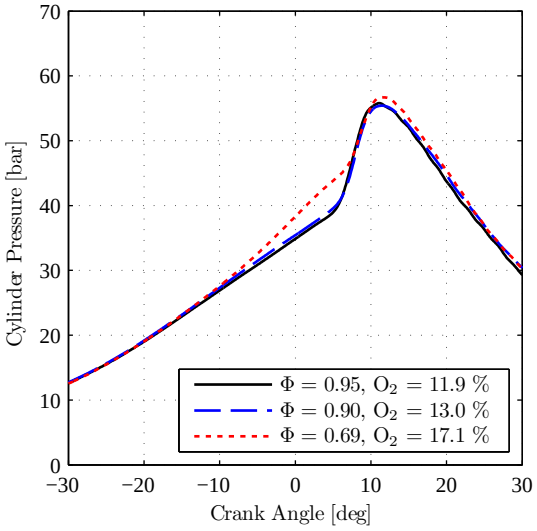

(c) Mean of Selected Cycles

Figure 6.4 Cylinder Pressure vs. Crank Angle for SACI operation, where diluent composition and intake temperature are simultaneously adjusted to maintain constant combustion phasing (CA50).

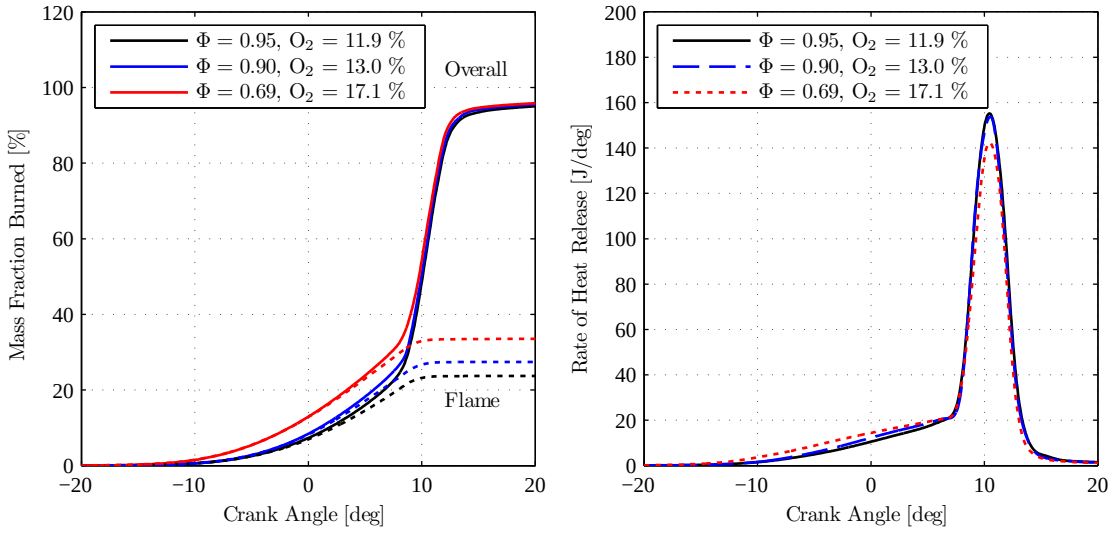

(a) Mass Fraction Burned (b) Rate of Heat Release

Figure 6.5 Model predicted mass fraction burned profiles, which shows that increasing O_2 concentration from 11.9% to 17.1% increases the fraction of flame based heat release 6.5(a) and reduces the peak rate of heat release by 10% 6.5(b).

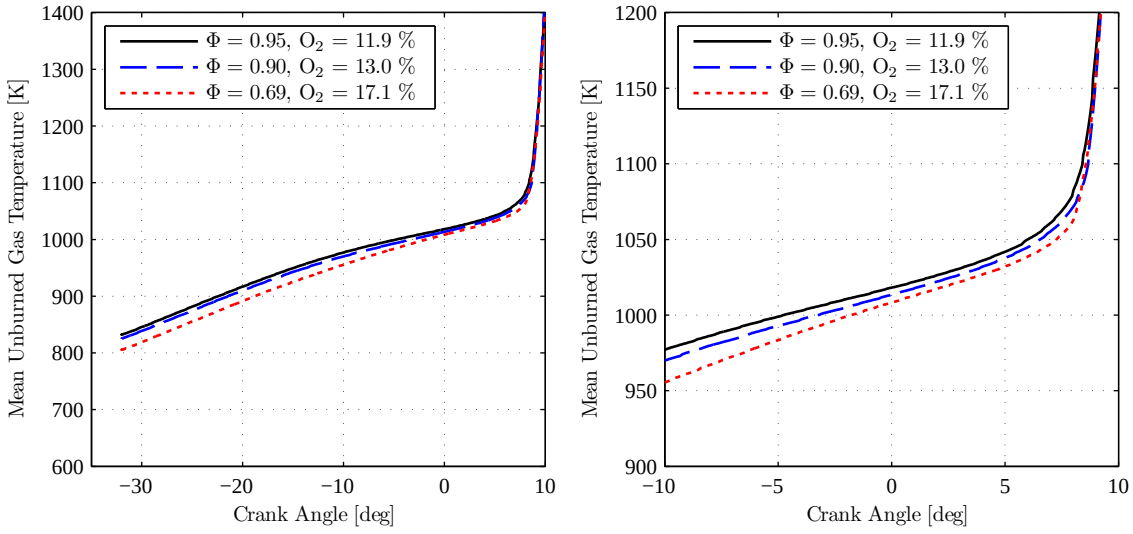

(a) End-gas Temperature (b) Temperature Detail

Figure 6.6 Model predicted mean unburned gas temperatures in 6.6(a) are initially lower for conditions with the highest O_2 concentration, with the temperature difference between the cases diminishing as they approach the onset of end-gas auto-ignition. At 8° aTDC where auto-ignition begins a 20 K difference in mean unburned gas temperature is observed 6.6(b).

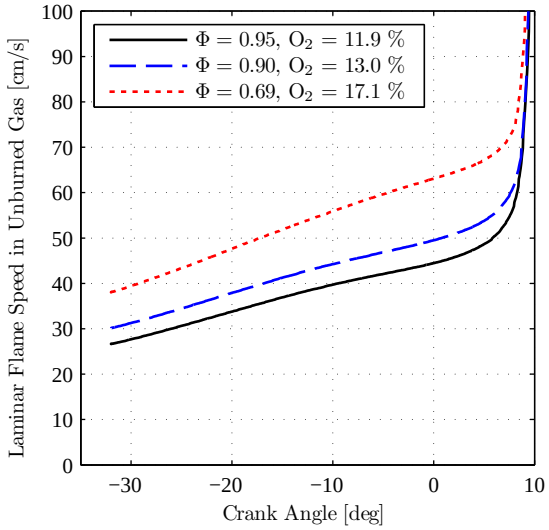

Figure 6.7 Model predicted laminar flame speed for the mean end-gas conditions. Higher O_2 concentration leads to higher flame speeds, despite decreased unburned mixture temperatures.

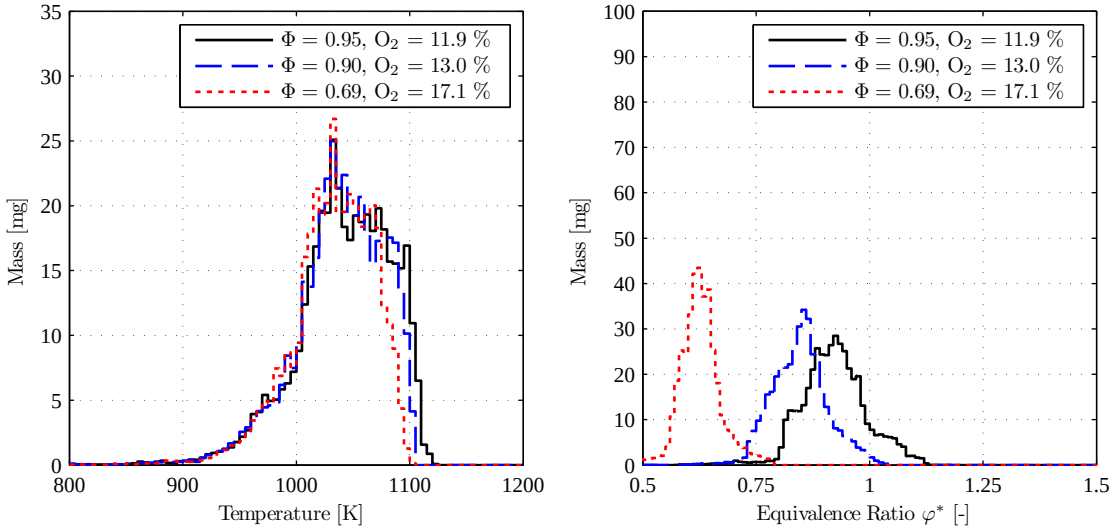

(a) Temperature (b) Composition

Figure 6.8 Unburned gas state distributions at 5° aTDC, immediately prior to autoignition. Figure 6.8(a) generated with 5 K temperature bins, Figure 6.8(b) with 0.01 φ^* bins.

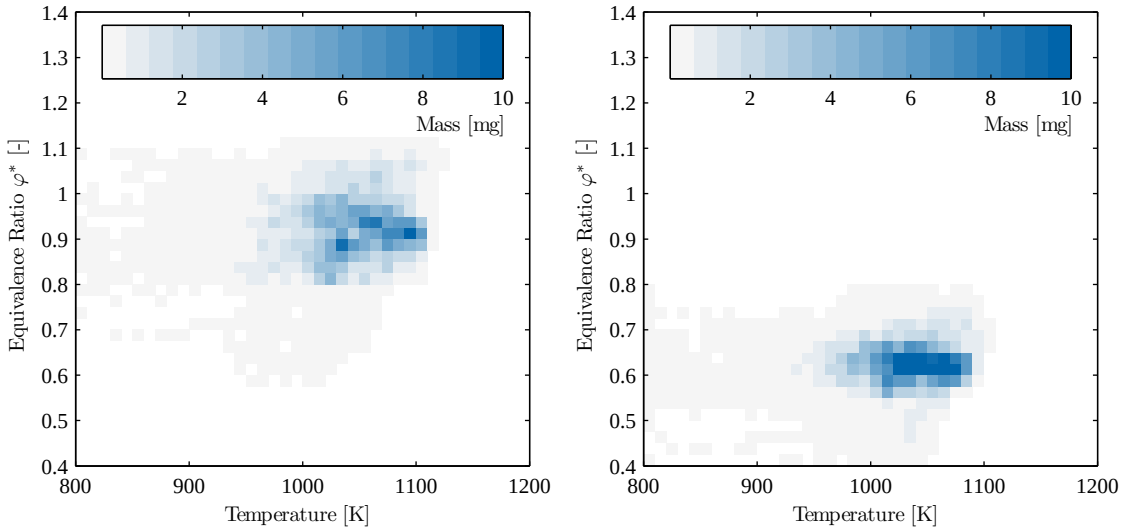

(a) $\Phi = 0.95$, 11.9% O_2 (b) $\Phi = 0.67$, 17.1% O_2

Figure 6.9 Mass and φ^* distributions at 5° aTDC for the 11.9% O_2 case 6.9(a) and the 17.1% O_2 case 6.9(b). No strong correlation between temperature and equivalence ratio is predicted.

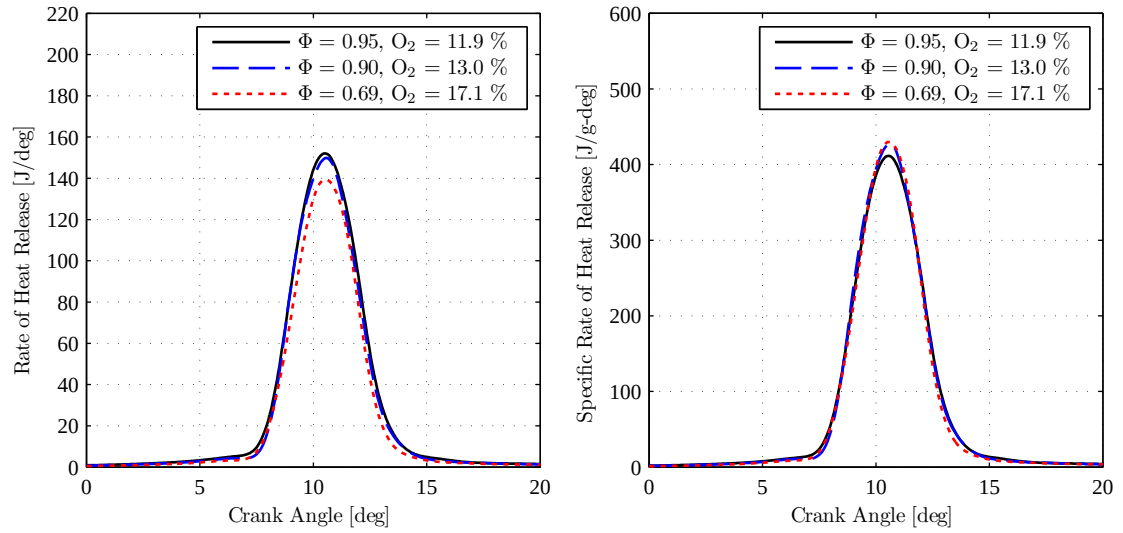

(a) Extensive (b) Intensive

Figure 6.10 End-gas contribution to the overall heat release rate calculated by differentiating the model predictions of mass fraction burned. Heat release rate is predicted to decrease by 8.3% with increasing O_2 concentration on an overall basis 6.10(a), while increasing 4.4% on a per mass 6.10(b) basis.

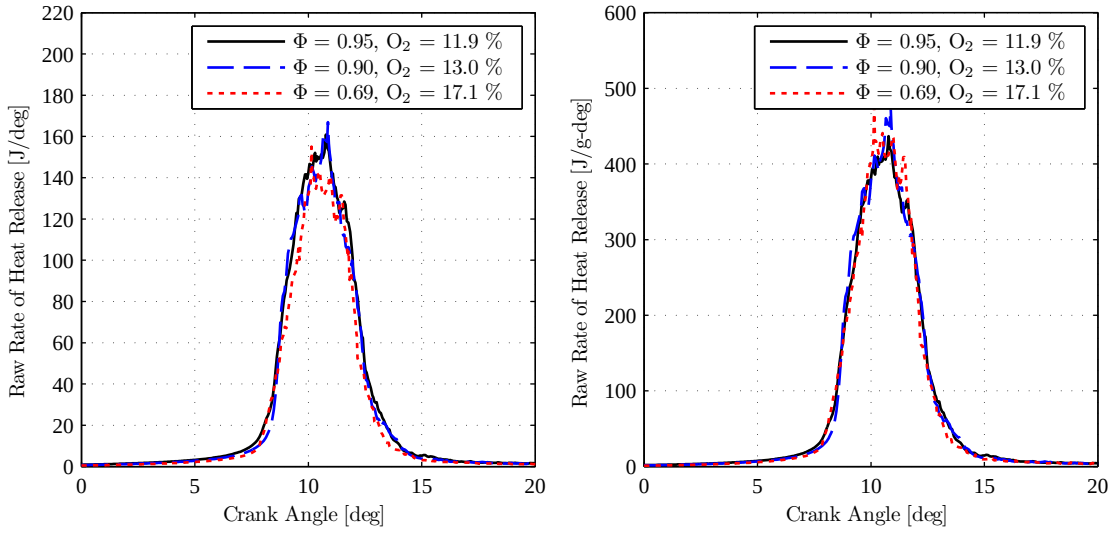

(a) Extensive

(b) Intensive

Figure 6.11 End-gas contribution to the overall heat release rate calculated by summing the contributions of each cell shows some timestep to timestep noise. Heat release rate is predicted to decrease slightly with increasing O_2 concentration on an overall basis 6.11(a), with no discernible difference on a per mass basis 6.11(b).

Chapter 7
Summary, Conclusions and Recommendations

7.1 Summary and Conclusions

The work presented in this document focused on applying detailed computational models to conditions diluted with EGR in order to better understand combustion behavior in the SACI combustion regime. In Chapter 2, the need for pre-mixed isooctane-air-EGR laminar reaction front data under the highly dilute, high preheat temperatures relevant for SACI combustion was addressed. Simulations of steady, one dimensional premixed laminar reaction fronts were conducted over a range of fuel-air equivalence ratios, unburned gas temperatures, pressures and EGR levels ranging from Φ = 0.1 to 1.0, T_u = 298 to 1000 K, p = 1 to 250 bar, EGR = 0 to 60% (by mass). These simulations extend an earlier study which covered a similar range of temperatures, pressures, and equivalence ratios but did not address dilution with EGR. Reaction fronts with moderate burning velocities could be achieved for highly EGR dilute mixtures typical of mid to high load HCCI and SACI operation, provided that the preheat temperatures were sufficiently elevated. Independent of EGR dilution level, it was noted that burned gas temperatures in excess of 1450 K were required to sustain burning velocities greater than 5 cm/s.

Reaction fronts diluted with EGR produced lower laminar burning velocities than air diluted reaction fronts with the same unburned and burned gas temperatures. Scaling studies were conducted to identify the chemical reactions exhibiting the greatest influence on S_L with changing O_2 concentration. Results showed that S_L is most sensitive the high temperature chain branching reaction between molecular oxygen and atomic hydrogen and the competing

chain terminating reaction between the same species. Under the conditions studied, burning velocity variations between conditions with EGR dilution and air dilution resulted primarily from decreases in the reaction rates of the O_2 kinetics between conditions.

Correlations for laminar burning velocity, burned gas temperature, and flame thickness were developed from the steady simulation results and showed good agreement with the simulation predictions. A method of characterizing fuel-air-EGR mixtures was developed to account for charge stratification in advanced combustion engines in a formulation particularly applicable to CFD modeling. In this formulation, a non-product equivalence ratio (φ) and a mole fraction of stoichiometric combustion products (X_{SCP}) replace the traditionally used global equivalence ratio (Φ) and EGR fraction.

A previously developed CFD model capable of capturing HCCI, SI, and SACI combustion modes, KIVA-CFMZ (KIVA Coherent Flamelet Multi-Zone), was extended to account for open cycle breathing and charge preparation typical of practical engines utilizing SACI combustion, discussed in detail in Chapter 3. The KIVA-CFMZ model combines the Coherent Flamelet Model for turbulent reaction front propagation with the fully coupled Multi-Zone model for detailed end- and product-gas chemical kinetics, using the laminar flame speed and thickness correlations from Chapter 2 as key inputs. New sub-models were added to the KIVA-CFMZ model to account for the presence of EGR in the mixture, to model direct fuel injection and evaporation during NVO, and to model spark ignition independent of mesh resolution. A transport equation was added to the model to account for non-uniform EGR dilution in the cylinder due to internal residual gases trapped from one cycle to the next. Additional improvements were also made to limit computational expense during open cycle calculations and facilitate modeling of several sequential cycles (however, the effects of sequential cycles were beyond the scope of this work).

In Chapter 4, the KIVA-CFMZ model predictions for open cycle simulations were compared to experimental HCCI, SI, and SACI combustion experiments. The KIVA-CFMZ model demonstrated excellent predictive capability for a range of HCCI and SI conditions,

with the model successfully replicating the experimentally reported trends using model parameters similar to prior studies. Extending the model to SACI combustion diluted with EGR required adjustment to the flame model tuning parameters to achieve good agreement with the experimental data, a change that was not required in previous closed cycle simulation studies of air dilute SI and SACI combustion. This change suggests the need for further validation of the flame model inputs, particularly the S_L and flame thickness predictions under high temperature highly EGR dilute conditions, where there are extremely few fundamental experimental datasets reported. Further, a method was developed to compare SACI combustion simulations to experimental SACI combustion data with large degrees of cycle to cycle variability. The analysis showed that the ensemble averaged, or "mean", experimental pressure results for SACI combustion cases with high cycle to cycle variability were poor predictors of any of the individual experimental cycle results. Based on these findings subsets of the experimental results were used for model comparison and validation purposes.

In Chapter 5 the KIVA-CFMZ model was used to investigate the variations in the peak rate of heat release observed at constant phasing during SACI combustion when the fraction of flame and auto-ignition heat release were adjusted through changes in spark timing and T_{IVC}. The model results successfully reproduced experimental trends, where the fraction of flame propagation increased as spark timing was advanced and T_{IVC} was decreased, simultaneously decreasing the peak heat release rate. Advanced spark timing at lower T_{IVC} conditions allowed additional time for flame propagation and compression heating to overcome differences initial temperature and caused all three conditions studied to reach the mean end-gas temperatures required to initiate end-gas auto-ignition at a similar crank angle. While some of the observed reduction in the peak end-gas rate of heat release was associated with the reduced end-gas mass available for auto-ignition as the fraction of the charge consumed by the flame increased, the peak end-gas heat release rates also decreased on a per end-gas mass basis. Detailed analysis of the end-gas state prior to auto-ignition showed that

the thermal and equivalence ratio distributions in the cylinder prior to auto-ignition shifted to lower peak values as spark advance is increased. The observed reduction in overall heat release rate with increasing spark advance therefore resulted from the reduction in end-gas mass available at auto-ignition, as well as a shift in the distribution of temperatures and equivalence ratios toward lower reactivities.

Finally, in Chapter 6, the KIVA-CFMZ model was used to investigate variations in SACI combustion behavior as the ratio of EGR dilution to air dilution was altered and the resulting mixture O_2 concentration varied at constant combustion phasing. Model predictions agreed well with experimentally reported trends, where the fraction of flame propagation increased as the O_2 concentration in the mixture increased and T_{IVC} decreased. Simultaneously, the peak rate of heat release decreased with increasing O_2 concentration. An increase in the fraction of heat release due to flame propagation with increasing O_2 concentrations was attributed to increased laminar burning velocities due to the change in O_2, despite decreasing unburned gas temperatures. Higher mean unburned gas temperatures at the time of auto-ignition in mixtures with lower O_2 concentrations were attributed to differences in the thermal stratification of the unburned gas, where negligible differences in stratification below 1050 K were observed, while the lowest O_2 conditions contained more mass at the highest temperatures near 1100 K. The observed decrease in the peak heat release rate as O_2 concentration increased was attributed to a decrease in end-gas mass undergoing auto-ignition as the flame had consumed a larger fraction of the charge at that time. Negligible differences were noted in the auto-ignition heat release rate on a per end-gas mass basis independent of the mixture oxygen concentration, suggesting that thermal stratification is the predominate factor controlling the auto-ignition heat release rate.

This is the first computational study to quantify the detailed chemical and physical mechanisms describing the successful application of SACI to independently control phasing and heat release rates in engines. The results provide the basis for understanding how compositional and thermal stratification can be used to actively control and improve SACI

engine operation. For example, advancing spark timing at constant composition allowed more time for flame propagation to consume the hottest portion of the charge, increasing the thermal stratification and leading to a decrease in peak heat release rates. Manipulation of the mixture composition and spark advance may be used to further affect stratification at auto-ignition and reduce peak combustion rates.

7.2 Recommendations for Future Work

There is currently a lack of fundamental experimental or computational data for the validation of the one-dimensional laminar reaction front simulations in Chapter 2, particularly for conditions with high levels of EGR dilution. These are particularly challenging conditions due to the small ratio of ignition delay to flame time (the time required to propagate one flame thickness) associated with SACI combustion. While data from engine experiments can be used to infer the laminar reaction front properties, the compounding complexity of an engine environment makes differentiating reaction front effects from turbulence, heat transfer, and charge preparation influences extremely difficult and in some cases impossible. For more fundamental experimental investigations, shock tubes and rapid compression machines may provide the conditions relevant to such studies.

The ITNFS flame stretch model used in this work was developed under SI combustion conditions. The ability of this model to accurately predict flame stretching given the characteristic velocities and length scales in the SACI combustion regime should be verified with direct simulation. The results presented in this work suggest that there is some critical difference between the SI and SACI regimes that is not correctly captured by the combination of the laminar flame properties predictions and the ITNFS flame stretch predictions. Additional insight is also required for the empirical flame surface density destruction terms used to model flamelet merging and annihilation, and if these factors change under EGR dilute SACI conditions. Flamelet simulations using direct numerical

simulation (DNS) would provide further insight into all of these factors.

The fuel injection and vaporization model used in the current work was configured as a typical gasoline direct injector. Detailed spray characteristics for the specific injector model used in the experiments were not available to validate the spray model predictions. Access to such measurements would improve confidence in the model predictions of charge preparation and compositional stratification. In addition, further study of sensitivity of the KIVA-CFMZ model predictions to changes in the charge preparation strategy should be conducted. The impact of injection parameters and fuel vaporization characteristics on combustion should be quantified.

Of particular interest is the potential for heat release or partial fuel reforming during NVO to impact combustion phasing. While repeated open cycle simulations with a detailed chemical mechanism are prohibitively expensive, the mechanism swapping procedure developed in this work can be used to greatly reduce the computational expense of the breathing process and enable such studies. Further analysis will need to be conducted in order to determine which chemical species are required to be tracked in detail through the breathing process. Recent advances in shared memory parallel processing through the proliferation of multi-core CPUs and improved socket to socket interconnects, resulting in systems with 24 cores and shared memory in a commodity application, provides the potential for accelerating the fluids calculations and breathing simulations in KIVA. Existing compiler directives for vectorized parallelism on Cray supercomputers should be updated with modern OpenMP directives to take advantage of these new resources and facilitate more detailed simulations of SACI combustion.

While the metal engine experiments and detailed combustion chamber mesh used in this work provide some validation for the KIVA-CFMZ model predictions over a range of HCCI, SI, and SACI conditions diluted with both air and EGR, additional validation should be conducted to assess the ability of the model to accurately predict conditions of interest for engine development. Experiments of SACI combustion with intake boosting should be

simulated, and the ability of the various sub-models in the KIVA-CFMZ model to accurately replicate these conditions should be assessed. To identify the impact of the isooctane fuel surrogate choice on the model predictions, additional simulations should be conducted with a more detailed gasoline surrogate mechanism. This includes both KIVA-CFMZ engine modeling as well as laminar reaction front modeling with HCT to account for any differences in the burning velocity of the two fuels under SACI operating conditions. Alternatively, metal engine SACI experiments could be conducted with isooctane fuel to provide similar validation of the model predictions.

Finally, the KIVA-CFMZ model should be exercised over a wide range of conditions to provide additional fundamental understanding of the physical processes governing SACI combustion. The model should be used to identify the causes of the shortcomings of HCCI and SACI, including issues associated with control over the heat release rate and power density. Under higher load conditions the model can be used to study the behavior of SI knock and the transition into the SACI regime. Model predictions should be used as a diagnostic tool to understand experimentally observed behavior, with the results acting as a guide to direct future experimental investigations.

References

[1] S. Onishi, S. H. Jo, K. Shoda, P. D. Jo, and S. Kato. Active Thermo-Atmosphere Combustion (ATAC) - A new combustion process for internal combustion engines. *SAE Paper 790501*, 1979.

[2] R. H. Thring. Homogeneous charge compression ignition (HCCI) engines. *SAE Paper 892068*, 1989.

[3] M. Christensen, B. Johansson, and P. Einewall. Homogeneous charge compression ignition (HCCI) using isooctane, ethanol and natural gas - A comparison with spark-ignition operation. *SAE Paper 972874*, 1997.

[4] J.-O. Olsson, P. Tunestål, G. Haraldsson, and B. Johansson. A turbocharged dual-fuel HCCI engine. *SAE Paper 2001-01-1896*, 2001.

[5] J.-O. Olsson, P. Tunestål, J. Ulfvik, and B. Johansson. The Effect of Cooled EGR on Emissions and Performance of a Turbocharged HCCI Engine. *SAE Paper 2003-01-0743*, 2003.

[6] S. H. Oh and J. C. Cavendish. Transients of monolithic catalytic converters. response to step changes in feedstream temperature as related to controlling automobile emissions. *Industrial & Engineering Chemistry Product Research and Development*, 21(1):29–37, 1982.

[7] A. Cairns and H. Blaxill. The effects of combined internal and external exhaust gas recirculation on gasoline controlled auto-ignition. *SAE Paper 2005-01-0133*, 2005.

[8] J. Hiltner, S. Fiveland, R. Agama, and M. Willi. System Efficiency Issues for Natural Gas Fueled HCCI Engines in Heavy-Duty Stationary Applications. *SAE Paper 2002-01-0417*, 2002.

[9] J. Heywood. *Internal combustion engine fundamentals*. McGraw-Hill series in mechanical engineering. McGraw-Hill, 1988.

[10] J. T. Farrell, J. G. Stevens, and W. Weissman. A second law analysis of high efficiency low emission gasoline engine concepts. *SAE Paper 2006-01-0491*, 2006.

[11] M. Noguchi, Y. Tanaka, T. Tanaka, and Y. Takeuchi. A Study on Gasoline Engine Combustion by Observation of Intermediate Reactive Products during Combustion. *SAE Paper 790840*, 1979.

[12] P. M. Najt and D. E. Foster. Compression-Ignited Homogeneous Charge Combustion. *SAE Paper 830264*, 1983.

[13] A. Hultqvist, M. Christensen, B. Johansson, M. Richter, J. Nygren, J. Hult, and M. Aldjn. The HCCI Combustion Process in a Single Cycle - Speed Fuel Tracer LIF and Chemiluminescence Imaging. *SAE Paper 2002-01-0424*, 2002.

[14] J. E. Dec, W. Hwang, and M. Sjöberg. An Investigation of Thermal Stratification in HCCI Engines Using Chemiluminescence Imaging. *SAE Paper 2006-01-1518*, 2006.

[15] S. B. Fiveland and D. N. Assanis. A Four-Stroke Homogeneous Charge Compression Ignition Engine Simulation for Combustion and Performance Studies. *SAE Paper 2000-01-0332*, 2000.

[16] J. Kodavasal. *Effect of Charge Preparation Strategy on HCCI Combustion*. PhD Thesis, The University of Michigan, Ann Arbor, MI, 2013.

[17] A. Kulzer, A. Christ, M. Rauscher, C. Sauer, G. Würfel, and T. Blank. Thermodynamic analysis and benchmark of various gasoline combustion concepts. *SAE Paper 2006-01-0231*, 2006.

[18] S. Fiveland. *Modeling and Experimental Studies of a Large-Bore Natural Gas Engine Operating on Homogeneous Charge Compression Ignition*. PhD Thesis, The University of Michigan, Ann Arbor, MI, 2001.

[19] M. Christensen and B. Johansson. Supercharged homogeneous charge compression ignition (HCCI) with exhaust gas recirculation and pilot fuel. *SAE Paper 2000-01-1835*, 2000.

[20] M. Christensen and B. Johansson. Influence of Mixture Quality on Homogeneous Charge Compression Ignition. *SAE Paper 982454*, 1998.

[21] P. A. Caton, H. H. Song, N. B. Kaahaaina, and C. F. Edwards. Strategies for Achieving Residual-Effected Homogeneous Charge Compression Ignition Using Variable Valve Actuation. *SAE Paper 2005-01-0165*, 2005.

[22] H. Persson, R. Pfeiffer, A. Hultqvist, B. Johansson, and H. Ström. Cylinder-to-Cylinder and Cycle-to-Cycle Variations at HCCI Operation With Trapped Residuals. *SAE Paper 2005-01-0130*, 2005.

[23] H. Persson, M. Agrell, J.-O. Olsson, B. Johansson, and H. Ström. The Effect of Intake Temperature on HCCI Operation Using Negative Valve Overlap. *SAE Paper 2004-01-0944*, 2004.

[24] A. Babajimopoulos, G. A. Lavoie, and D. N. Assanis. Modeling HCCI Combustion With High Levels of Residual Gas Fraction - A Comparison of Two VVA Strategies. *SAE Paper 2003-01-3220*, 2003.

[25] F. Zhao, T. Asmus, D. Assanis, J. Dec, J. Eng, and P. Najt. Homogeneous Charge Compression Ignition (HCCI) Engines-Key Research and Development Issues, Society of Automotive Engineers. *Inc., Warrendale, PA*, 2003.

[26] J. A. Eng. Characterization of pressure waves in hcci combustion. *SAE Paper 2002-01-2859*, 2002.

[27] D. Flowers, S. Aceves, R. Smith, J. Torres, J. Girard, and R. Dibble. HCCI in a CFR Engine: Experiments and Detailed Kinetic Modeling. *SAE Paper 2000-01-0328*, 2000.

[28] J. A. Eng. Characterization of Pressure Waves in HCCI Combustion. *SAE Paper 2002-01-2859*, 2002.

[29] L. Manofsky, J. Vavra, D. Assanis, and A. Babjimopoulos. Bridging the Gap between HCCI and SI: Spark Assisted Compression Ignition. *SAE Paper 2011-01-1179*, 2011.

[30] J.-O. Olsson, P. Tunestål, B. Johansson, S. Fiveland, R. Agama, M. Willi, and D. Assanis. Compression Ratio Influence on Maximum Load of a Natural Gas Fueled HCCI Engine. *SAE Paper 2002-01-0111*, 2002.

[31] L. Koopmans, O. Backlund, and I. Denbratt. Cycle to cycle variations: Their influence on cycle resolved gas temperature and unburned hydrocarbons from a camless gasoline compression ignition engine. *SAE Paper 2002-01-0110*, 2002.

[32] L. MANOFSKY OLESKY, J. Vavra, D. Assanis, and A. Babajimopoulos. Effects of charge preheating methods on the combustion phasing limitations of an hcci engine with negative valve overlap. *Journal of engineering for gas turbines and power*, 134(11), 2012.

[33] T. W. Ryan and T. J. Callahan. Homogeneous Charge Compression Ignition of Diesel Fuel. *SAE Paper 961160*, 1996.

[34] J. E. Dec and Y. Yang. Boosted HCCI for High Power without Engine Knock and with Ultra-Low NOx Emissions - using Conventional Gasoline. *SAE Paper 2010-01-1086*, 2010.

[35] J. Allen and D. Law. Variable valve actuated controlled auto-ignition: Speed load maps and strategic regimes of operation. *SAE Paper 2002-01-0422*, 2002.

[36] J.-O. Olsson, P. Tunestål, B. Johansson, S. Fiveland, R. Agama, M. Willi, and D. Assanis. Compression ratio influence on maximum load of a natural gas fueled hcci engine. *SAE Paper 2002-01-0111*, 2002.

[37] E. Ortiz-Soto. *Combustion Modeling of Spark Assisted Compression Ignition for Experimental Analysis and Engine System Simulations*. PhD Thesis, The University of Michigan, 2013.

[38] L. K. Olesky. *An Experimental Investigation of the Burn Rates of Naturally Aspirated Spark Assisted Compression Ignition Combustion in a Single Cylinder Engine with Negative Valve Overlap*. PhD Thesis, The University of Michigan, 2013.

[39] C. K. Westbrook. Chemical kinetics of hydrocarbon ignition in practical combustion systems. *Proceedings of the Combustion Institute*, 28(2):1563–1577, Jan. 2000.

[40] C. Westbrook and F. Dryer. Prediction of laminar flame properties of methanol-air mixtures. *Combustion and Flame*, 37:171–192, 1980.

[41] C. K. Westbrook, F. L. Dryer, and K. Schug. Numerical modeling of ethylene oxidation in laminar flames. *Combustion and Flame*, 52 IS -:299–313, 1983.

[42] H. J. Curran, P. Gaffuri, W. Pitz, and C. Westbrook. A comprehensive modeling study of iso-octane oxidation. *Combustion and Flame*, 129(3):253–280, may 2002.

[43] C. K. Law. *Combustion physics*. Cambridge University Press, 2006.

[44] M. Sjöberg and J. E. Dec. An investigation into lowest acceptable combustion temperatures for hydrocarbon fuels in HCCI engines. *Proceedings of the Combustion Institute*, 30(2):2719–2726, Jan. 2005.

[45] M. Sjöberg, J. E. Dec, A. Babajimopoulos, and D. Assanis. Comparing enhanced natural thermal stratification against retarded combustion phasing for smoothing of hcci heat-release rates. *SAE Paper 2004-01-2994*, 2004.

[46] J. E. Dec. A Computational Study of the Effects of Low Fuel Loading and EGR on Heat Release Rates and Combustion Limits in HCCI Engines. *SAE Paper 2002-01-1309*, 2002.

[47] J. E. Dec, M. Sjöberg, and W. Hwang. Isolating the effects of egr on hcci heat-release rates and nox emissions. *SAE Paper 2009-01-2665*, 2009.

[48] L. M. Olesky, G. A. Lavoie, D. N. Assanis, M. S. Wooldridge, and J. B. Martz. The effects of diluent composition on the rates of hcci and spark assisted compression ignition combustion. *Applied Energy*, Submitted for Publication, 2014.

[49] S. S. Morimoto, Y. Kawabata, T. Sakurai, and T. Amano. Operating Characteristics of a Natural Gas-Fired Homogeneous Charge Compression Ignition Engine (Performance Improvement Using EGR). *SAE Paper 2001-01-1034*, Mar. 2001.

[50] D. A. Rothamer, J. A. Snyder, R. K. Hanson, R. R. Steeper, and R. P. Fitzgerald. Simultaneous imaging of exhaust gas residuals and temperature during hcci combustion. *Proceedings of the Combustion Institute*, 32(2):2869–2876, 2009.

[51] T. Aroonsrisopon, P. Werner, J. O. Waldman, V. Sohm, D. E. Foster, T. Morikawa, and M. Iida. Expanding the hcci operation with the charge stratification. *SAE Paper 2004-01-1756*, 2004.

[52] P. W. Bessonette, C. H. Schleyer, K. P. Duffy, W. L. Hardy, and M. P. Liechty. Effects of fuel property changes on heavy-duty hcci combustion. *SAE Paper 2007-01-0191*, 2007.

[53] J.-O. Olsson, P. Tunestål, G. Haraldsson, and B. Johansson. A turbo charged dual fuel hcci engine. *SAE Paper 2001-01-1896*, 2001.

[54] G. A. Lavoie, J. B. Martz, M. Wooldridge, and D. N. Assanis. A multi-mode combustion diagram for spark assisted compression ignition. *Combustion and Flame*, 157(6):1106–1110, jun 2010.

[55] A. Fuerhapter, W. F. Piock, and G. K. Fraidl. CSI - Controlled Auto Ignition - the Best Solution for the Fuel Consumption - Versus Emission Trade-Off? *SAE Paper 2003-01-0754*, 2003.

[56] Z. Wang, J.-X. Wang, S.-J. Shuai, G.-H. Tian, X. An, and Q.-J. Ma. Study of the effect of spark ignition on gasoline hcci combustion. *Proceedings of the Institution of Mechanical Engineers, Part D: Journal of Automobile Engineering*, 220(6):817–825, 2006.

[57] H. Yun, N. Wermuth, and P. Najt. Extending the High Load Operating Limit of a Naturally-Aspirated Gasoline HCCI Combustion Engine. *SAE Paper 2010-01-0847*, 2010.

[58] T. Urushihara, K. Yamaguchi, K. Yoshizawa, and T. Itoh. A study of a gasoline-fueled compression ignition engine expansion of hcci operation range using si combustion as a trigger of compression ignition . *SAE Paper 2005-01-0180*, 2005.

[59] H. Yun, N. Wermuth, and P. Najt. High load hcci operation using different valving strategies in a naturally-aspirated gasoline hcci engine. *SAE Paper 2011-01-0899*, 2011.

[60] J. P. Szybist, E. Nafziger, and A. Weall. Load expansion of stoichiometric hcci using spark assist and hydraulic valve actuation. *SAE Paper 2010-01-2172*, 2010.

[61] B. Zigler. *An Experimental Investigation of the Properties of Low Temperature Combustion in an Optical Engine*. PhD Thesis, Ph. D. Thesis, The University of Michigan, Ann Arbor, MI, 2008.

[62] H. Persson, A. Hultqvist, B. Johansson, and A. Remon. Investigation of the Early Flame Development in Spark-Assisted HCCI Combustion Using High-Speed Chemiluminescence Imaging. *SAE Paper 2007-01-0212*, 2007.

[63] D. L. Reuss, T.-W. Kuo, G. Silvas, V. Natarajan, and V. Sick. Experimental metrics for identifying origins of combustion variability during spark-assisted compression ignition. *International Journal of Engine Research*, 9(5):409–434, oct 2008.

[64] B. T. Zigler, P. E. Keros, K. B. Helleberg, M. Fatouraie, D. Assanis, and M. S. Wooldridge. An experimental investigation of the sensitivity of the ignition and combustion properties of a single-cylinder research engine to spark-assisted HCCI. *International Journal of Engine Research*, 12(4):353–375, Jan. 2011.

[65] B. Zigler, S. Walton, X. He, J. Wiswall, M. Wooldridge, and S. Wooldridge. Crank-Angle Resolved Imaging of Homogeneous Charge Compression Ignition Phenomena in a Single-Cylinder Research Engine, Tech. Meeting, CSS. *The Combustion Institute, Cleveland, OH*, 2006.

[66] Y. Huang, C. J. Sung, and J. A. Eng. Dilution limits of n-butane/air mixtures under conditions relevant to HCCI combustion. *Combustion and Flame*, 136(4):457–466, 2004.

[67] L. M. Olesky, J. B. Martz, G. A. Lavoie, J. Vavra, D. N. Assanis, and A. Babajimopoulos. The effects of spark timing, unburned gas temperature, and negative valve overlap on the rates of stoichiometric spark assisted compression ignition combustion. *Applied Energy*, 105:407–417, 2013.

[68] J. Martz, R. Middleton, G. Lavoie, A. Babajimopoulos, and D. Assanis. A computational study and correlation of premixed isooctane-air laminar reaction front properties under spark ignited and spark assisted compression ignition engine conditions. *Combustion and Flame*, 158(6):1089 – 1096, 2011.

[69] J. B. Martz, G. A. Lavoie, H. G. Im, R. J. Middleton, A. Babajimopoulos, and D. N. Assanis. The propagation of a laminar reaction front during end-gas auto-ignition. *Combustion and Flame*, 159(6):2077 – 2086, 2012.

[70] J. B. Martz. *Simulation and Model Development for Auto-Ignition and Reaction Front Propagation in Low-Temperature High-Pressure Lean-Burn Engines*. PhD Thesis, The University of Michigan, Ann Arbor, MI, 2010.

[71] R. Kee, J. Grcar, M. Smooke, and J. Miller. A Fortran program for modeling steady laminar one-dimensional premixed flames. *Sandia National Laboratory Report SAND85-8240*, 1985.

[72] P. F. Flynn, G. L. Hunter, R. P. Durrett, L. A. Farrell, and W. C. Akinyemi. Minimum Engine Flame Temperature Impacts on Diesel and Spark-Ignition Engine NOx Production. *SAE Paper 2000-01-1177*, 2000.

[73] G. A. Lavoie and P. Blumberg. Measurements of NO Emissions From a Stratified Charge Engine: Comparison of Theory and Experiment. *Combustion Science and Technology*, 8(1):25–37, 1973.

[74] X. He, M. Donovan, B. Zigler, T. Palmer, S. Walton, M. Wooldridge, and A. Atreya. An experimental and modeling study of iso-octane ignition delay times under homogeneous charge compression ignition conditions. *Combustion and Flame*, 142(3):266–275, 2005.

[75] A. Babajimopoulos, G. A. Lavoie, and D. N. Assanis. On the role of top dead center conditions in the combustion phasing of homogeneous charge compression ignition engines. *Combustion science and technology*, 179(9):2039–2063, 2007.

[76] M. Sjöberg and J. E. Dec. Influence of Fuel Autoignition Reactivity on the High-Load Limits of HCCI Engines. *SAE Paper 2008-01-0054*, 2008.

[77] R. M. Wagner, K. D. Edwards, C. S. Daw, J. B. Green, and B. G. Bunting. On the Nature of Cyclic Dispersion in Spark Assisted HCCI Combustion. *SAE Paper 2006-01-0418*, Apr. 2006.

[78] B. T. Zigler, S. M. Walton, D. M. Karwat, D. Assanis, M. S. Wooldridge, and S. T. Wooldridge. A Multi-Axis Imaging Study of Spark-Assisted Homogeneous Charge Compression Ignition Phenomena in a Single-Cylinder Research Engine. *ASME Conference Proceedings*, 2007(48116):395–405, 2007.

[79] G. A. Lavoie, E. Ortiz-Soto, A. Babajimopoulos, J. B. Martz, and D. N. Assanis. Thermodynamic sweet spot for high-efficiency, dilute, boosted gasoline engines. *International Journal of Engine Research*, 14(3):260–278, 2013.

[80] X. Wang, H. Xie, L. Li, L. Xie, T. Chen, and H. Zhao. Effect of the thermal stratification on si-cai hybrid combustion in a gasoline engine. *Applied Thermal Engineering*, 61(2):451–460, 2013.

[81] Z. Filipi and D. N. Assanis. Quasi-Dimensional Computer Simulation of the Turbocharged Spark-Ignition Engine and its Use for 2- and 4-Valve Engine Matching Studies. *SAE Paper 910075*, 1991.

[82] L. Liang, R. D. Reitz, C. O. Iyer, and J. Yi. Modeling Knock in Spark-Ignition Engines Using a G-equation Combustion Model Incorporating Detailed Chemical Kinetics. *SAE Paper 2007-01-0165*, 2007.

[83] S. Yang and R. Reitz. Improved combustion submodels for modelling gasoline engines with the level set G equation and detailed chemical kinetics. *Proceedings of the Institution of Mechanical Engineers*, 223:703–726, 2009.

[84] R. Dahms, C. Felsch, O. Röhl, and N. Peters. Detailed chemistry flamelet modeling of mixed-mode combustion in spark-assisted hcci engines. *Proceedings of the Combustion Institute*, 33(2):3023–3030, 2011.

[85] R. N. Dahms, M. C. Drake, T. D. Fansler, T.-W. Kuo, and N. Peters. Understanding ignition processes in spray-guided gasoline engines using high-speed imaging and the extended spark-ignition model sparkcimm. part a: Spark channel processes and the turbulent flame front propagation. *Combustion and flame*, 158(11):2229–2244, 2011.

[86] R. N. Dahms, M. C. Drake, T. D. Fansler, T.-W. Kuo, and N. Peters. Understanding ignition processes in spray-guided gasoline engines using high-speed imaging and the extended spark-ignition model sparkcimm: Part b: Importance of molecular fuel

properties in early flame front propagation. *Combustion and Flame*, 158(11):2245 – 2260, 2011.

[87] N. Peters. *Turbulent combustion*. Cambridge monographs on mechanics. Cambridge University Press, 2000.

[88] T. Baritaud, J. Duglos, and A. Fusco. Modeling turbulent combustion and pollutant formation in stratified charge SI engines. *Symposium (International) on Combustion*, 26(2):2627–2635, 1996.

[89] O. Colin, A. Benkenida, and C. Angelberger. 3D modeling of mixing, ignition and combustion phenomena in highly stratified gasoline engines. *Oil & Gas Science and Technology-Revue De L Institut Francais Du Petrole*, 58(1):47–62, 2003.

[90] A. Colin and A. Benkenida. The 3-zones extended coherent flame model (ECFM3Z) for computing premixed/diffusion combustion. *Oil & Gas Science and Technology-Revue De L Institut Francais Du Petrole*, 59(6):593–609, 2004.

[91] V. Knop and S. Jay. Latest developments in gasoline Auto-Ignition modelling applied to an optical CAI engine. *Oil & gas science and technology*, 2006.

[92] O. Colin, A. Pires da Cruz, and S. Jay. Detailed chemistry-based auto-ignition model including low temperature phenomena applied to 3-D engine calculations. *Proceedings of the Combustion Institute*, 30(2):2649–2656, 2005.

[93] A. Teraji, T. Tsuda, T. Noda, M. Kubo, and T. Itoh. Development of a three-dimensional knock simulation method incorporating a high-accuracy flame propagation model. *International Journal of Engine Research*, 6(1):73–83, Jan. 2005.

[94] M. Metghalchi and J. C. Keck. Burning velocities of mixtures of air with methanol, isooctane, and indolene at high pressure and temperature. *Combustion and Flame*, 48:191–210, 1982.

[95] Ö. L. Gülder. Correlations of Laminar Combustion Data for Alternative S.I. Engine Fuels. *SAE Paper 841000*, 1984.

[96] L. Liang and R. D. Reitz. Spark Ignition Engine Combustion Modeling Using a Level Set Method with Detailed Chemistry. *SAE Paper 2006-01-0243*, 2006.

[97] P. Eckert, S.-C. Kong, and R. D. Reitz. Modeling Autoignition and Engine Knock Under Spark Ignition Conditions. *SAE Paper 2003-01-0011*, 2003.

[98] B. Vanzieleghem. *Combustion Modeling for Gasoline Direct Injection Engines Using KIVA-3V*. PhD Thesis, The University of Michigan, Ann Arbor, MI, 2004.

[99] A. Babajimoppulos. *Development of Sequential and Fully Integrated CFD/Multi-Zone Models with Detailed Chemical Kinetics for the Simulation of HCCI Engines*. PhD Thesis, The University of Michigan, Ann Arbor, MI, 2005.

[100] R. J. Middleton, J. B. Martz, G. A. Lavoie, A. Babajimopoulos, and D. N. Assanis. A computational study and correlation of premixed isooctane air laminar reaction fronts diluted with egr. *Combustion and Flame*, 159(10):3146–3157, 2012.

[101] J. Martz, R. Middleton, G. Lavoie, M. Fatouraie, B. Zigler, M. Wooldridge, A. Babajimopoulos, and D. Assanis. Modeling Spark-Assisted Compression Ignition Combustion in an Optical Engine. *Submitted for Review: 35th Symposium (International) on Combustion*, 2014.

[102] R. J. Middleton, J. B. Martz, L. K. M. Olesky, G. A. Lavoie, M. S. Wooldridge, and D. N. Assanis. The effect of spark timing and negative valve overlap on spark assisted compression ignition combustion heat release rate. *35th Combustion Symposium*, Submitted for Publication, 2014.

[103] D. Veynante and L. Vervisch. Turbulent combustion modeling. *Progress in Energy and Combustion Science*, 28(3):193–266, 2002.

[104] M. Wirth and N. Peters. Turbulent premixed combustion: A flamelet formulation and spectral analysis in theory and IC-engine experiments. *Symposium (International) on Combustion*, 24(1):493–501, 1992.

[105] R. J. Tabaczynski, F. H. Trinker, and B. A. S. Shannon. Further refinement and validation of a turbulent flame propagation model for spark-ignition engines. *Combustion and Flame*, 39(2):111–121, oct 1980.

[106] W. J. Pitz, N. P. Cernansky, F. L. Dryer, F. N. Egolfopoulos, J. T. Farrell, D. G. Friend, and H. Pitsch. Development of an Experimental Database and Chemical Kinetic Models for Surrogate Gasoline Fuels. *SAE Paper 2007-01-0175*, 2007.

[107] S. Jerzembeck, N. Peters, P. Pepiot-Desjardins, and H. Pitsch. Laminar burning velocities at high pressure for primary reference fuels and gasoline: Experimental and numerical investigation. *Combustion and Flame*, 156(2):292 – 301, 2009.

[108] T. W. I. Ryan and S. S. Lestz. The laminar burning velocity of issooctane, n-heptane, methanol, methane, and propane at elevated temperature and pressures in the presence of a diluent. *SAE Paper 800103*, 1980.

[109] D. Bradley, R. Hicks, M. Laws, C. Sheppard, and R. Wooley. The Measurement of Laminar Burning Velocities and Markstein Numbers for Isooctane and Isooctane-n-Heptane-Mixtures at Elevated Temperatures and Pressures in an Explosion Bomb. *Combustion and Flame*, 115:126–144, 1998.

[110] J. Göttgens, F. Mauss, and N. Peters. Analytic approximations of burning velocities and flame thicknesses of lean hydrogen, methane, ethylene, ethane, acetylene, and propane flames. *Symposium (International) on Combustion*, 24(1):129–135, 1992.

[111] U. C. Müller, M. Bollig, and N. Peters. Approximations for burning velocities and markstein numbers for lean hydrocarbon and methanol flames. *Combustion and Flame*, 108(3):349–356, feb 1997.

[112] D. B. Rhodes and J. C. Keck. Laminar Burning Speed Measurements of Indolene-Air-Diluent Mixtures at High Pressures and Temperatures. *SAE Paper 850047*, 1985.

[113] Z. Zhao, A. Kazakov, J. Li, and F. Dryer. The initial temperature and N_2 dilution effect on the laminar flame speed of propane/air. *Combustion science and technology*, 176(10):1705–1723, 2004.

[114] C. Tang, Z. Huang, J. He, C. Jin, X. Wang, and H. Miao. Effects of n2 dilution on laminar burning characteristics of propane-air premixed flames. *Energy & Fuels*, 23(1):151–156, 2009.

[115] S. P. Marshall, S. Taylor, C. R. Stone, T. J. Davies, and R. F. Cracknell. Laminar burning velocity measurements of liquid fuels at elevated pressures and temperatures with combustion residuals. *Combustion and Flame*, 158(10):1920–1932, 2011.

[116] R. Dahms, C. Felsch, O. Röhl, and N. Peters. Detailed chemistry flamelet modeling of mixed-mode combustion in spark-assisted HCCI engines. *Proceedings of the Combustion Institute*, 33(2):3023–3030, 2011.

[117] C. Lund. *HCT: A general computer program for calculating time-dependent phenomena involving one-dimensional hydrodynamics, transport, and detailed chemical kinetics*. Lawrence Livermore Laboratory, University of California, 1978.

[118] C. Corre, F. Dryer, W. Pitz, and C. Westbrook. Two-stage N-butane flame: A comparison between experimental measurements and modeling results. *Symposium (International) on Combustion*, 24(1):843–850, 1992.

[119] H. J. Curran, M. P. Dunphy, J. M. Simmie, C. K. Westbrook, and W. J. Pitz. Shock tube ignition of ethanol, isobutene and MTBE: Experiments and modeling. *Symposium (International) on Combustion*, 24(1):769–776, 1992.

[120] H. J. Curran, P. Gaffuri, W. Pitz, and C. Westbrook. A Comprehensive Modeling Study of n-Heptane Oxidation. *Combustion and Flame*, 114(1-2):149–177, jul 1998.

[121] S. Wang, D. L. Miller, N. P. Cernansky, H. J. Curran, W. J. Pitz, and C. K. Westbrook. A flow reactor study of neopentane oxidation at 8 atmospheres: experiments and modeling. *Combustion and Flame*, 118(3):415–430, aug 1999.

[122] C. Westbrook, A. Adamczyk, and G. A. Lavoie. A numerical study of laminar flame wall quenching. *Combustion and Flame*, 40:81–99, 1981.

[123] C. Westbrook and F. Dryer. Simplified reaction mechanisms for the oxidation of hydrocarbon fuels in flames. *Combustion science and technology*, 27(1-2):31–43, 1981.

[124] Y. F. Tham, F. Bisetti, and J. Y. Chen. Development of a Highly Reduced Mechanism for Iso-Octane HCCI Combustion With Targeted Search Algorithm. *Journal of Engineering for Gas Turbines and Power*, 130(4):042804, 2008.

[125] R. Kee, G. Dixon-Lewis, J. Warnatz, M. Contrin, and J. Miller. A Fortran computer code package for the evaluation of gas-phase multicomponent transport properties, Report SAND86-8246. *UC-401, SANDIA Albuquerque*, 1986.

[126] D. F. Davidson, B. M. Gauthier, and R. K. Hanson. Shock tube ignition measurements of iso-octane/air and toluene/air at high pressures. *Proceedings of the Combustion Institute*, 30(1):1175–1182, jan 2005.

[127] H. Shen, J. Vanderover, and M. Oehlschlaeger. A shock tube study of iso-octane ignition at elevated pressures: The influence of diluent gases. *Combustion and Flame*, 155(4):739–755, dec 2008.

[128] K. Kumar, J. E. Freeh, C. J. Sung, and Y. Huang. Laminar flame speeds of preheated iso-octane /O_2/N_2 and n-heptane /Oxygen/N_2 mixtures. *Journal of propulsion and power*, 23(2):428–436, 2007.

[129] S. G. Davis and C. K. Law. Determination of and fuel structure effects on laminar flame speeds of C1 to C8 hydrocarbons. *Combustion science and technology*, 140(1-6):427–449, 1998.

[130] M. Marchionni, S. K. Aggarwal, I. K. Puri, and D. Lentini. The influence of real-gas thermodynamics on simulations of freely propagating flames in methane/oxygen/inert mixtures. *Combustion Science and Technology*, 179(9):1777–1795, 2007.

[131] A. M. Saur, F. Behrendt, and E. U. Franck. Calculation of high pressure counterflow diffusion flames up to 3000 bar. *Berichte der Bunsengesellschaft für physikalische Chemie*, 97(7):900–907, 1993.

[132] A. Babajimopoulos, D. Assanis, D. Flowers, S. Aceves, and R. Hessel. A fully coupled computational fluid dynamics and multi-zone model with detailed chemical kinetics for the simulation of premixed charge compression ignition engines. *International Journal of Engine Research*, 6(5):497–512, 2005.

[133] N. Peters and F. Williams. The asymptotic structure of stoichiometric methane-air flames. *Combustion and Flame*, 68(2):185 – 207, 1987.

[134] A. A. Amsden. Kiva-3v: A block-structured kiva program for engines with vertical or canted valves. Technical report, Los Alamos National Lab., NM (United States), 1997.

[135] C. Meneveau and T. Poinsot. Stretching and quenching of flamelets in premixed turbulent combustion. *Combustion and Flame*, 86(4):311–332, 1991.

[136] P. Boudier, S. Henriot, T. Poinsot, and T. Baritaud. A model for turbulent flame ignition and propagation in spark ignition engines. *Symposium (International) on Combustion*, 24(1):503–510, 1992.

[137] J. M. Duclos, D. Veynante, and T. Poinsot. A comparison of flamelet models for premixed turbulent combustion. *Combustion and Flame*, 95(1-2):101–117, 1993.

[138] S. A. Filatyev, J. F. Driscoll, C. D. Carter, and J. M. Donbar. Measured properties of turbulent premixed flames for model assessment, including burning velocities, stretch rates, and surface densities. *Combustion and Flame*, 141(1-2):1–21, 2005.

[139] J. M. Duclos, G. Bruneaux, and T. Baritaud. 3D Modeling of Combustion and Pollutants in a 4-Valve SI Engine; Effect of Fuel and Residuals Distribution and Spark Location. *SAE Paper 961964*, 1996.

[140] T. Poinsot, D. Haworth, and G. Bruneaux. Direct simulation and modeling of flame-wall interaction for premixed turbulent combustion. *Combustion and Flame*, 95(1-2):118–132, 1993.

[141] S. M. Aceves, J. Martinez-Frias, D. Flowers, J. R. Smith, R. Dibble, and J. Y. Chen. A Computer Generated Reduced Iso-Octane Chemical Kinetic Mechanism Applied to Simulation of HCCI Combustion. *SAE Paper 2002-01-2870*, 2002.

[142] J. Kodavasal. An Improved Multi-Zone Combustion Model for PCCI Simulation. Master's thesis, M.S. Thesis University of Michigan, Ann Arbor, MI , 2010.

[143] R. J. Kee, F. M. Rupley, and J. A. Miller. Chemkin-ii: A fortran chemical kinetics package for the analysis of gas-phase chemical kinetics. Technical report, Sandia National Labs., Livermore, CA (USA), 1989.

[144] C. Chryssakis and D. N. Assanis. A unified fuel spray breakup model for internal combustion engine applications. *Atomization and Sprays*, 18(5), 2008.

[145] B. Vanzieleghem, C. Chryssakis, R. Grover, V. Sick, H. Im, and D. Assanis. Modeling of gasoline direct injection mixture formation using kiva-3v: Development of spray breakup & wall impingement models and validation with optical engine planar laser induced fluorescence measurements. 2004.

[146] C. Chryssakis, K. Driscoll, V. Sick, and D. Assanis. Validation of an enhanced liquid sheet atomisation model against quantitative laser diagnostic measurements. *Zaragoza*, 9:11, 2002.

[147] C. A. Chryssakis, D. N. Assanis, J.-K. Lee, and K. Nishida. Fuel spray simulation of high-pressure swirl-injector for disi engines and comparison with laser diagnostic measurements. *SAE Paper 2003-01-0007*, 2003.

[148] C. Chryssakis and D. Assanis. A secondary atomization model for liquid droplet deformation and breakup under high weber number conditions. In *ILASS Americas, 18th Annual Conference on Liquid Atomization and Spray Systems, Irvine, CA*, 2005.

[149] D. P. Schmidt, I. Nouar, P. K. Senecal, C. J. Rutland, J. K. Martin, R. D. Reitz, and J. A. Hoffman. Pressure-swirl atomization in the near field. *SAE Paper 1999-01-0496*, 1999.

[150] P. Senecal, D. P. Schmidt, I. Nouar, C. J. Rutland, R. D. Reitz, and M. Corradini. Modeling high-speed viscous liquid sheet atomization. *International Journal of Multiphase Flow*, 25(6):1073–1097, 1999.

[151] W. K. Brown and K. H. Wohletz. Derivation of the weibull distribution based on physical principles and its connection to the rosin–rammler and lognormal distributions. *Journal of Applied Physics*, 78(4):2758–2763, 1995.

[152] P. J. O'Rourke and A. A. Amsden. The tab method for numerical calculation of spray droplet breakup. *SAE Paper 872089*, 1987.

[153] R. Grover, D. Assanis, A. Lippert, S. El Tahry, M. Drake, T. Fansler, and D. Harrington. A critical analysis of splash criteria for gdi spray impingement. In *15th Annual Conference on Liquid Atomization and Spray Systems*, 2002.

[154] C. Law. Heat and mass transfer in combustion: fundamental concepts and analytical techniques. *Progress in energy and combustion science*, 10(3):295–318, 1984.

[155] K. K. Kuo. *Principles of combustion*. Wiley New York et al., 1986.

[156] S. R. Turns. *An Introduction to Combustion*. McGraw-Hill, Inc., 1996.

[157] F. U. Manual. Fluent userís guide. *Fluent Inc, Lebanon*, 2005.

[158] P. ORourke and A. Amsden. A particle numerical model for wall film dynamics in port-injected engines. Technical report, Los Alamos National Lab., NM (United States), 1996.

[159] W. M. Rohsenow. A method of correlating heat transfer data for surface boiling of liquids. Technical report, Cambridge, Mass.: MIT Division of Industrial Cooporation,[1951], 1951.

[160] R. Herweg and R. R. Maly. A Fundamental Model for Flame Kernel Formation in S. I. Engines. *SAE Paper 922243*, 1992.

[161] S. Falfari and G. M. Bianchi. Development of an Ignition Model for S.I. Engines Simulation. *SAE Paper 2007-01-0148*, 2007.

[162] Z. Tan and R. D. Reitz. An ignition and combustion model based on the level-set method for spark ignition engine multidimensional modeling. *Combustion and Flame*, 145(1):1–15, 2006.

[163] M. Lim, R. Anderson, and V. S. Arpaci. Prediction of spark kernel development in constant volume combustion. *Combustion and flame*, 69(3):303–316, 1987.

[164] Y. Ko, R. Anderson, and V. S. Arpaci. Spark ignition of propane-air mixtures near the minimum ignition energy: Part i. an experimental study. *Combustion and flame*, 83(1):75–87, 1991.

[165] E. Lusk, N. Doss, and A. Skjellum. A high-performance, portable implementation of the mpi message passing interface standard. *Parallel Computing*, 22:789–828, 1996.

[166] W. D. Gropp, E. L. Lusk, and A. Skjellum. *Using MPI: portable parallel programming with the message-passing interface*, volume 1. the MIT Press, 1999.

[167] M. Snir, S. W. Otto, D. W. Walker, J. Dongarra, and S. Huss-Lederman. *MPI: the complete reference*. MIT press, 1995.

[168] G. M. Amdahl. Validity of the single processor approach to achieving large scale computing capabilities. In *Proceedings of the April 18-20, 1967, spring joint computer conference*, pages 483–485. ACM, 1967.

[169] R. P. Fitzgerald, R. Steeper, J. Snyder, R. Hanson, and R. Hessel. Determination of cycle temperatures and residual gas fraction for hcci negative valve overlap operation. *SAE Paper 2010-01-0343*, 2010.

[170] M. Namazian and J. Heywood. Flow in the piston-cylinder-ring crevices of a spark-ignition engine: Effect on hydrocarbon emissions, efficiency and power. *SAE Paper 820088*, 1982.

[171] J. X. Zhao and C. fon F. Lee. Modeling of blow-by in a small-bore high-speed direct-injection optically accessible diesel engine. *SAE Paper 2006-01-0649*, 2006.

[172] J. B. Martz, R. J. Middleton, G. A. L. B. Zigler, and M. S. Wooldridge. Insights into the affect of the top land crevice volume during hcci combustion within an optical engine. In Preparation, 2014.

[173] Gamma Technologies, Inc. *GT-Suite V7.2*. http://www.gtisoft.com.

[174] Gamma Technologies, Inc. *GT-Suite Engine Performance Application Manual*. Version 7.2.

[175] A. Omrane, G. Juhlin, M. Aldén, G. Josefsson, J. Engström, and T. Benham. Demonstration of two-dimensional temperature characterization of valves and transparent piston in a gdi optical engine. *SAE Paper 2004-01-0609*, 2004.

[176] J. E. Dec and M. Sjöberg. Isolating the effects of fuel chemistry on combustion phasing in an hcci engine and the potential of fuel stratification for ignition control. *SAE Paper 2004-01-0557*, 2004.

[177] O. Colin, A. Benkenida, and C. Angelberger. 3d modeling of mixing, ignition and combustion phenomena in highly stratified gasoline engines. *Oil & gas science and technology*, 58(1):47–62, 2003.